Time-discretization of a plasma-neutral MHD model with a semi-implicit leapfrog algorithm

Sina Taheri

A dissertation
submitted in partial fulfillment of the
requirements for the degree of

Doctor of Philosophy

University of Washington

2021

Reading Committee:
Uri Shumlak, Chair
Brian Nelson
Justin Little

Program Authorized to Offer Degree:
Aerospace and Energetics Research Program

University of Washington

Abstract

Time-discretization of a plasma-neutral MHD model with a semi-implicit leapfrog algorithm

Sina Taheri

Chair of the Supervisory Committee:
Professor Uri Shumlak
Department of Aeronautics and Astronautics

Interaction between plasma fluid and neutral species is of great importance in the dynamic behavior of magnetically confined plasma devices, such as the edge region of tokamaks and the plasma formation of Z-pinches. The presence of neutrals can have beneficial effects such as fueling burning plasmas and quenching the disruptions in tokamaks, as well as deleterious effects like depositing high energy particles on the vessel wall. Also, it can affect the stability of a pinch and change the dynamics of the pinch collapse. Thus, incorporation of atomic physics with plasma modeling tools is required to study next-generation fusion devices.

Fluid-based plasma models such as magnetohydrodynamic (MHD) are commonly used for fusion simulation. One of the key challenges in numerical simulation with these fluid models is the vast separation of the time scales describing different physics in the model. The semi-implicit leapfrog time advance scheme is one of the commonly used algorithms for initial-value problems that can bridge between fast-wave and slow-diffusive time scales. Functional structure of the MHD equations results in a data dependency among fields and lets the advances for the plasma density, velocity, temperature, and magnetic field to be staggered and solved sequentially.

Inclusion of the atomic interactions between plasma and neutral species breaks the data dependency in MHD equations and also adds more to an already vast span of time scales. A reacting plasma-neutral model [E. T. Meier, and U. Shumlak. “A general nonlinear fluid

model for reacting plasma-neutral mixtures." Physics of Plasmas 19.7 (2012): 072508] is used to study the interaction between plasma and neutral fluids that accounts for electron-impact ionization, radiative recombination, and resonant charge exchange. In this research we address how to best integrate atomic physics into semi-implicit leapfrog time advance. Two competing approaches are studied: 1) Crank-Nicolson time-centering of the atomic reactions within the framework of leapfrog algorithm. A Newton iteration is used to include nonlinear terms in atomic physics. 2) Operator-splitting the terms associated with the atomic interactions into constituent ODE and PDE parts using a Strang-splitting technique. As a variation to this splitting method a Douglas-Rachford inspired splitting scheme is considered as well.

Accuracy and efficiency of the time-advance methods are studied through a series of zero- and one-dimensional test cases. Among the 0-D cases we compare the shear Alfvén and magneto-acoustic wave propagation results with analytic solutions where all other cases are compared to a fine-time-resolution base calculation. We consider two 1-D examples: fusion-plasma edge fueling representing a slow dynamic application and a planar electromagnetic plasma accelerator as a fast wave application.

We show that a second-order-in-time Douglas-Rachford inspired coupling between the ODE and PDE advances is effective in reducing the time-discretization error to be comparable to that of Crank-Nicolson with Newton iteration of the nonlinear terms. Splitting ODE and PDE parts results in independent matrix solves for each field which reduces the computational cost considerably and provides parallelization over species relative to Crank-Nicolson.

TABLE OF CONTENTS

LIST OF FIGURES

LIST OF TABLES

ACKNOWLEDGMENTS

I would like to thank a variety of people whom without this work would not be possible. Professor Uri Shumlak provided me the opportunity to continue my education in plasma physics and helped me to learn a lot. I cannot properly express my gratitude to Dr. Jacob King who helped me and supported me from the beginning and none of this work would have been done without him. I only can say thank you. I also want to thank Dr. Chris Hansen who has been providing support in difficult situations that I have experienced. Additionally, I would like to thank the entire (former and present) group members in Computational Plasma Dynamics Lab: Eric Meier, Sean Miller, Iman Datta, Andrew Ho, Whitney Thomas, Daniel Crews, Aria Johansen, and Yu Takagaki. Lastly, I would like to thank my family, who supported me during all these years: my parents Farhad and Zahra, my brother Saeed, my sister-in-law Faegheh, and my amazing friend Mehraveh who is like a family member.

DEDICATION

To my family,
and my sunlight, Mehraveh.

Chapter 1

INTRODUCTION

The modern world is tightly coupled with energy consumption. The amount of energy used by a nation is one of the measures to evaluate life standards in that society. Even there is a proposed measure that relates humankind evolution to the amount of energy being used by the entire planet. Humankind started energy conversion thousands of years ago by discovering fire. Since then humans were always in search of more efficient and more abundant forms of energy sources. After industrial revolution and extraordinary jump in energy consumption worldwide, atomic energy joined its predecessor, chemical energy, to provide the ever-increasing demand for energy. However, this thirst for advance and evolution resulted in extreme environmental complexities and threatens the essence of life itself. Greenhouse gases and nuclear wastes are becoming huge problems in energy production and the need to find cleaner sources of energy becoming more obvious than ever.

This is where fusion comes into play. According to Einstein's famous equation $E = mc^2$, when light atoms such as hydrogen combine to create a heavier element like helium, a portion of their mass converts to energy. The energy density of this reaction is several times higher than a fission reaction where an unstable heavy atom breaks into two, and several thousands times the energy density of fossil fuels. In addition, fusion reaction does not produce any kind of greenhouse gas, and its nuclear waste has a short lifetime which makes it manageable and disposable.

Ironically fusing light atoms needs a tremendous amount of energy to overcome the electromagnetic repulsion of the nuclei. Increasing the energy of the atoms makes particles move faster and collisions with other particles may break the bond between electrons and the nucleus. This substance of free electrons and nuclei is called plasma and it is the doorway to

thermonuclear fusion energy. In the early days of plasma physics, scientists were more interested in plasma state itself and different theories, such as magnetohydrodynamics (MHD) and kinetic theory, were proposed to describe the behavior of plasma. This understanding of plasma physics lets the scientists move forward to build devices and confine plasma in pursuit of fusion energy. Different concepts were introduced during the years but one property was the same for almost every concept, plasma was in contact with a solid wall. This interaction between plasma and neutral states of mater brought new concepts and consequently new complexities in plasma physics. More specifically in magnetically confined plasmas, the region of interest were divided into two sections, the core and the edge. In the core region, temperature is so high that neutrals rarely exist. On the other hand, temperatures in the edge region are in the range where plasma and neutrals exist in a comparable fractions and interactions between them is the main object of focus.

Recently, the plasma edge has become an area of extreme importance in plasma physics investigations. Many experimental studies have indicated that the overall performance characteristics of confined plasmas are determined by phenomena happening in this thin region. Atomic reactions between plasma and neutral species involving recycling and fueling are important in the dynamic behavior of magnetically confined plasma devices particularly in edge region [35]. Also, injecting massive high pressure gas, liquid jets, and killer pellets are a few of the possible approaches to mitigate disruptions and control damage to vessel structures [11]. Similarly, the presence of neutrals can affect the stability of the pinch in Z-pinch devices and change the dynamics of the pinch collapse [14, 38].

There are different descriptions of neutral transport in plasmas in the literature that takes into account the effects of neutrals in plasma dynamics. On a high level classification, there are kinetic neutral transport methods and fluid representation of neutral species. The former class includes the spherical harmonics methods (e.g., diffusion theory), the integral transport, or collision probability methods, the interface current balance methods, and Monte Carlo methods [35], where in the fluid representation, the neutrals are treated as another fluid species described with conventional Navier-Stokes equations [2, 35].

Similar to many other branches of science, studying plasmas and their interaction with neutrals is pursued with different approaches such as theoretical, numerical, and experimental. Each of these approaches has its own advantages and disadvantages. Theoretical studies give deeper understanding of underlying physics while they cannot extend beyond simple geometries and reduced complexities. On the other hand, experimental studies give all the detail about a real-life device, however, building and running these experiments are expensive and time-consuming. And in the middle ground, numerical simulations are relatively cheap and more flexible in terms of setup but common numerical descriptions have different fidelities and they do not include all the underlying physics. In this research we focus on numerical studies of plasma-neutral models and specifically the time-discretization algorithms.

Focusing on fluid description of plasma dynamics with magnetohydrodynamic (MHD) equations, a key challenge is incorporation of vastly separated time scales. Fast dynamics are mediated by Alfvén waves while changes to the magnetic topology occurs on a slower time-scale determined by the low plasma resistivity. On top of that, fluid equations for atomic interactions introduce additional stiff coupling through effects such as ionization, recombination and charge exchange.

Without atomic interaction, time discretization of the MHD equations using a mixed implicit/semi-implicit leapfrog method [20, 30, 33, 34] is a often employed to bridge the fast-wave and slow-diffusive time scales. This algorithm is a workhorse for initial-value MHD codes such as NIMROD [33] and M3D-C1 [12]. Considering the functional dependencies for MHD equations the advances for plasma density, velocity, temperature and magnetic field can be staggered or solved sequentially. However, inclusion of plasma-neutral interactions breaks this data dependency, thus introducing new sources of error into numerical simulations.

1.1 Objectives

In this research we address how to best integrate the atomic physics into the implicit/semi-implicit leapfrog algorithm that is consistent with NIMROD implementation while delivering

acceptable accuracy. We consider two competing approaches for this implementation:

- coupling the neutral species to the plasma through a time-centered Crank-Nicolson approach within the structure of the leapfrog advance,

- operator-splitting the terms associated with the atomic interactions using a Strang-splitting technique.

In the Crank-Nicolson approach the coupled plasma and neutral fields are each solved simultaneously but coupling between some fields (e.g., centering the temperature in the density advance) is neglected. And in order to include nonlinear terms that arise through the atomic interactions, we employ an approximate Jacobian-free Newton-Krylov method.

Alternatively, the operator-splitting scheme breaks equations into constituent ODE (no spatial gradients) and PDE parts. All the nonlinear contributions are handled by the ODE solver, thus, no nonlinear iteration is required. Furthermore, we modify the Strang-split algorithm using a Douglas-Rachford inspired splitting method to eliminate the error associated with the leapfrog structure neglecting the functional dependencies introduced by the atomic physics terms and also reduce the ODE/PDE splitting error.

We study the accuracy and efficiency of these algorithms through a battery of 0-D and 1-D cases. Identifying different sources of error in numerical implementations, we try to address them in these competing methods. As applications to this numerical tool, we look at fusion-plasma edge fueling in a generic 1-D tokamak pedestal, as well as plasma acceleration in a sheared flow stabilized Z-pinch. We also look at 2-D setups for ion orbit loss in tokamak pedestal and plasma acceleration in Z-pinch.

1.2 Overview of this research

In Chap. 2 we describe the plasma-neutral model equations presented by Meier and Shumlak [21] and associated approximations in more detail. Chapter 3 describes the spatial and temporal discretization schemes used here. The discussion next turns to the details of the

competing time-discretization methods and quantifying the different sources of (e.g., from using a leapfrog method with atomic interactions, neglect of the nonlinear contributions and operator splitting). In Chap. 4 we employ a number of zero-dimensional tests with varied plasma-neutral parameters to diagnose the accuracy and computational efficiency of each time-discretization. Since these tests neglect any error associated with the ODE/PDE splitting, we move on to one-dimensional tests by considering cases that roughly represent tokamak-plasma edge fueling and z-pinch startup from a plasma-gun injector. Next, in Chap. 5 we look at some two-dimensional applications of the numerical tool in hand by considering the geometry effects in the z-pinch acceleration region as well as 2-D simulations of plasma-neutral interactions in the edge region of tokamak-plasma pedestals. At the end, we conclude by proposing some future work that can be pursued using the findings of this research.

Chapter 2

A MODEL OF INTERACTING PLASMA AND NEUTRALS

Partially ionized plasma consists of at least three different components: electrons, positive ions, and neutral atoms or molecules. Plasma components interact with each other via collisions and electromagnetic fields where plasma and neutrals interact only due to collisions between them. Collisions between particles can be elastic or inelastic, whether the particles keep their identity or lose it. These species can be treated as separate fluids governed by conservation laws to describe their dynamic behavior. Mass, momentum, and energy conservation laws for each fluid can be derived from a statistical point of view and different species are coupled through collisions and atomic reactions.

2.1 History of plasma-neutral model

The field of partially ionized plasmas is pursued in many different communities, such as astrophysics, atmospheric and space sciences, low-temperature plasma physics, fusion, and others. In this research, we will describe the development of the fusion and astrophysics perspectives.

First, we focus on edge plasma physics and neutral effects on the dynamics of magnetically confined devices within the fusion community. Among early studies of coupled plasma-neutral systems, Vold et al. [40] described the neutrals in a diffusion approximation and gave a set of transport equations for plasma. One of the limitations of this early model was the assumption of ambipolarity to compute plasma potential, drift velocity, and net poloidal velocity. Hazeltine et al. [9] using the simplicity of charge exchange (CX) operator developed a general variational principle to include the effects of neutrals on plasma transport. While this method showed the effects of neutrals on the plasma for an arbitrary CX cross-section,

it didn't include neutral-neutral collisions and it was non-local. The simplifying assumptions of short CX mean-free-path and constant product of CX cross-section and relative velocity, allowed them to solve neutral particle, momentum, and heat fluxes directly to present neutral transport coefficients. Looking specifically into neutral-ion transport at tokamak edge plasma, Catto [3] presented a set of short mean-free-path moment equations for single neutral and single-ion system where charge exchange, ionization, and recombination were considered. Three simplifying assumptions were essential for this model, namely, negligible neutral-neutral collisions, constant CX rate (product of CX cross-section and relative velocity), and negligible modifications of electron distribution function due to electron-neutral collision and atomic processes. Helander et al. [10] improved upon the former models by considering a more complicated CX cross-section to get accurate transport coefficients. They presented their results as a set of hydrodynamic equations and transport coefficients for partially ionized plasmas in tokamak edge region. Following Catto, Simakov [31] used drift-ordering to present a close set of fluid equations for collisional, magnetized, partially ionized plasma which targets the edge of plasma confinement devices. Meier and Shumlak [21] took a general approach to interactive plasma-neutral modeling starting from Boltzmann equation and extending Braginskii's method to get two-component and three-component presentation of the model. Both elastic scattering collisions and inelastic reacting collisions are considered in this model.

Alternatively, we can follow the partially ionized plasma model development from the astrophysical perspective. Birk and Otto [2] presented a plasma-neutral gas-fluid model by integrating the balance equations for the plasma, neutral gas, and magnetic field under the constraint of conservation of mass, momentum, and energy. They studied linear and nonlinear problems assuming semi-empirical transport coefficients to validate the model and proposed Earth's magnetosphere-ionosphere and solar photosphere chromosphere as immediate applications. Zaqarashvili et al. [43] focused on MHD waves in solar partially ionized plasmas, compared wave dynamics in single-fluid and two-fluid descriptions. They showed that for high-frequency (compared to ion-neutral collision frequency) waves, neutral effects

are considerable and the two-fluid model is a better approximation. Khomenko et al. [16] gave a history of models used to describe phenomena in the solar atmosphere, emphasizing neutrals effects on chromospheric plasma due to weak collisionality. Similar to Meier and Shumlak, they started with the Boltzmann equation including interaction with radiation via excitation/deexcitation and ionization recombination to get photons as a separate species interacting with other species.

2.2 Model derivation

In this research we follow the Meier and Shumlak [21] scheme to describe plasma-neutral model generalizing Braginskii's approach. The starting point is the Boltzmann equation for species α,

$$\frac{\partial f_\alpha}{\partial t} + \mathbf{v} \cdot \nabla_x f_\alpha + \frac{q_\alpha}{m_\alpha} (\mathbf{E} + \mathbf{v} \times \mathbf{B}) \cdot \nabla_v f_\alpha = \frac{\partial f_\alpha}{\partial t}|_{collisions} = C_\alpha^{scat.,react.}, \tag{2.1}$$

where f_α is the distribution function of particles and the collision term, $C_\alpha^{scat.,react.}$, refers to scattering and reacting collisions. Scattering collisions are elastic collisions and derived using the Braginskii approach, where reacting collisions include ionization, recombination, and charge exchange reactions, which are treated in the same manner by Meier and Shumlak [21]. The fluid description of the model is achieved taking velocity moments of the Boltzmann equation, where a neutral species is added as a separate distribution function and interactions between all components are considered in the mass, the momentum, and the energy conservation laws. The closures are derived using a Chapman-Enskog expansion where it specifies an ordering of important terms in the Boltzmann equation.

Deriving conservation laws with fluid description requires an averaging scheme for the distribution function in velocity space. The first three moments of the Boltzmann equation ignoring the reacting collisions is well derived in literature. However, it is the integrals of the reacting collisions that plays an important role in reactive plasma-neutral models describing the dynamics of the coupled system. Before taking the moments of the Boltzmann equation to obtain the fluid equations, we summarize the moments of the reacting collision operators

presented in [21]. Three reacting collisions, namely electron impact ionization, radiative recombination, and resonant charge exchange are considered in this model where the collision operators for them are

$$\begin{aligned}
C_e^{ion} &= f_n \int f_e \sigma_{ion} v_{rel} d\mathbf{v}, \\
C_i^{ion} &= f_n \int f_e \sigma_{ion} v_{rel} d\mathbf{v}, \\
C_n^{ion} &= -f_n \int f_e \sigma_{ion} v_{rel} d\mathbf{v}, \\
C_e^{rec} &= -f_e \int f_i \sigma_{rec} v_{rel} d\mathbf{v}, \\
C_i^{rec} &= -f_i \int f_e \sigma_{rec} v_{rel} d\mathbf{v}, \\
C_n^{rec} &= \frac{m_e}{m_n} f_e \int f_i \sigma_{rec} v_{rel} d\mathbf{v} + \frac{m_i}{m_n} f_i \int f_e \sigma_{rec} v_{rel} d\mathbf{v}, \\
C_i^{cx} &= f_n \int f_i \sigma_{cx} v_{rel} d\mathbf{v} - f_i \int f_n \sigma_{cx} v_{rel} d\mathbf{v}, \\
C_n^{cx} &= \frac{m_i}{m_n} f_i \int f_n \sigma_{cx} v_{rel} d\mathbf{v} - \frac{m_i}{m_n} f_n \int f_i \sigma_{cx} v_{rel} d\mathbf{v},
\end{aligned} \tag{2.2}$$

where v_{rel} is the relative velocity of the colliding particles, cross-sections for electron impact ionization and radiative recombination are only functions of electron random velocity, and the charge exchange cross-section is considered to be a function of collision velocity. For deriving the fist three moments of the reacting collision operators a Maxwellian distribution function is assumed, $f_\alpha = n_\alpha (\pi v_{T\alpha}^2)^{-3/2} \exp\left[-(\mathbf{v} - \mathbf{v}_\alpha)^2 / v_{T\alpha}^2\right]$, where n_α is the number density, $v_{T\alpha}$ is the thermal velocity, $\mathbf{v}$ is the particle velocity, and $\mathbf{v}_\alpha$ is the bulk velocity of the species α.

0^{th} moments

The 0^{th} moments of collision operators appear in continuity equation mainly, however, they simplify the other conservation laws. The ionization effect on neutrals is

$$\int C_n^{ion} d\mathbf{v} = -\int f_n(\mathbf{v}') \int f_e(\mathbf{v}) \sigma_{ion}(v_{rel}) v_{rel} d\mathbf{v} d\mathbf{v}'. \tag{2.3}$$

Without presenting the details of integration, the final expression is

$$\int C_n^{ion} d\mathbf{v} \approx \Gamma_n^{ion} = -n_e n_n \langle \sigma_{ion} v_e \rangle, \tag{2.4}$$

where $\langle \sigma_{ion} v_e \rangle$ is the ionization rate parameter and Γ_n^{ion} is the notation for source rates due to ionization affecting neutral species. Voronov [41] presented the ionization rate for hydrogen atom as a function of electron temperature as

$$\langle \sigma_{ion} v_e \rangle = 0.291 \times 10^{-13} \frac{1}{0.232 + \phi_{ion}} \left(\frac{\phi_{ion}}{T_e} \right)^{0.39} \exp - \left(\frac{\phi_{ion}}{T_e} \right) \quad [m^3/s], \tag{2.5}$$

with ϕ_{ion} representing the ionization energy. Similarly, the ionization contribution to ion species is found to be $\int C_i^{ion} d\mathbf{v}' \approx \Gamma_i^{ion} = -\Gamma_n^{ion}$ and the ionization contribution to electron species is identical $\int C_e^{ion} d\mathbf{v}' \approx \Gamma_e^{ion} = -\Gamma_n^{ion}$.

Recombination effects are captured in the same manner by the following integral

$$\int C_i^{rec} d\mathbf{v} \approx \Gamma_i^{rec} = -n_e n_i \langle \sigma_{rec} v_e \rangle, \tag{2.6}$$

where $\langle \sigma_{rec} v_e \rangle$ is the recombination rate parameter, presented as a function of electron temperature T_e by Goldston [7],

$$\langle \sigma_{rec} v_e \rangle = 0.7 \times 10^{-19} \left(\frac{13.6}{T_e} \right)^{1/2}. \tag{2.7}$$

Following the ionization reaction, recombination contribution to the electron and neutral species are $\int C_e^{rec} d\mathbf{v}' \approx \Gamma_e^{rec} = \Gamma_i^{rec}$ and $\int C_n^{rec} d\mathbf{v}' \approx \Gamma_n^{rec} = -\Gamma_i^{rec}$, respectively.

It is clear that the charge exchange does not change the electron, the ion or the neutral net number density. However, defining the source rate for charge exchange collisions is important for completeness and easing the calculation of higher moments. Meier [22] presented the calculation in detail where the charge exchange collision operator can be approximated as

$$C_i^{cx} \approx \sigma_{cx} (v_i^* n_i f_n - v_n^* n_n f_i), \tag{2.8}$$

where $v_\alpha^* \equiv \sqrt{4 v_{T\alpha}/\pi + (\mathbf{v} - \mathbf{v}_\alpha)^2}$. Under the assumption that the neutral gas distribution function is dominated by neutral-neutral scattering collisions, Meier [22] gave the 0^{th} moment for the first term in charge exchange collision operator as

$$\int \sigma_{cx} v_i^* f_n d\mathbf{v} \approx \sigma_{cx}(V_{cx}) n_i n_n V_{cx}, \tag{2.9}$$

with V_{cx} defined as a representative speed for charge exchange collisions,

$$V_{cx} \equiv \sqrt{\frac{4}{\pi}v_{Ti}^2 + \frac{4}{\pi}v_{Tn}^2 + v_{in}^2}, \tag{2.10}$$

where $v_{in}^2 \equiv |\mathbf{v}_i - \mathbf{v}_n|^2$. Resonant charge exchange cross-section is generally a weak function of the defined velocity, V_{cx}. Meier [22] suggested $\sigma_{cx} = 1.12 \times 10^{-18} - 7.15 \times 10^{-20} \ln(V_{cx})$ as an acceptable fit to ORNL [1] data set.

1^{st} moments

A key assumption in calculating the first moments is splitting the particle velocity into bulk and random velocities, $\mathbf{v} = \mathbf{v}_\alpha + \mathbf{w}$. In this manner, the integral for the bulk velocity is simply related to the 0^{th} moment and only the second term needs to be calculated. The first moment of the ionization collision operator is expressed as

$$\int m_i \mathbf{v} C_i^{ion} d\mathbf{v} = \int m_i \mathbf{v} f_n(\mathbf{v}) \int f_e(\mathbf{v}') \sigma_{ion} v_{rel} d\mathbf{v}' d\mathbf{v}. \tag{2.11}$$

Splitting the velocity and using the approximation for inner integral,

$$\int m_i \mathbf{v} C_i^{ion} d\mathbf{v} = m_i n_e \langle \sigma_{ion} v_e \rangle \left(\mathbf{v}_n \int f_n d\mathbf{v} + \int \mathbf{w} f_n d\mathbf{v} \right), \tag{2.12}$$

the first term on the right hand side is related to ionization 0^{th} moment and the second term is zero (odd integral). Therefore,

$$\int m_i \mathbf{v} C_i^{ion} d\mathbf{v} = m_i \mathbf{v}_n \Gamma_i^{ion}. \tag{2.13}$$

Similarly, the 1^{st} moments of ionization collision operator acting on electron and neutral species are $\int m_e \mathbf{v} C_e^{ion} d\mathbf{v} = m_e \mathbf{v}_n \Gamma_i^{ion}$ and $\int m_n \mathbf{v} C_n^{ion} d\mathbf{v} = -m_n \mathbf{v}_n \Gamma_i^{ion}$, respectively.

In the same manner, the 1^{st} moment contribution of recombination reaction to ion, electron, and neutral species are

$$\begin{aligned} \int m_i \mathbf{v} C_i^{rec} d\mathbf{v} &= -m_i \mathbf{v}_i \Gamma_n^{rec}, \\ \int m_e \mathbf{v} C_e^{rec} d\mathbf{v} &= -m_e \mathbf{v}_i \Gamma_n^{rec}, \\ \int m_n \mathbf{v} C_n^{rec} d\mathbf{v} &= (m_i \mathbf{v}_i + m_e \mathbf{v}_e) \Gamma_n^{rec}. \end{aligned} \tag{2.14}$$

Calculation of the 1^{st} moment contribution of the charge exchange to ion species is done by splitting the particle velocity like before and using the definition of charge exchange flux,

$$\begin{aligned}\int m_i \mathbf{v} C_i^{cx} d\mathbf{v} &\approx \int m_i \sigma_{cx} \mathbf{v} (n_i v_i^* f_n - n_n v_v^* f_i) d\mathbf{v} \\ &= m_i(\mathbf{v}_n - \mathbf{v}_i)\Gamma^{cx} + m_i \sigma_{cx} \left(n_i \int \mathbf{w} v_i^* f_n d\mathbf{v} - n_n \int \mathbf{w} v_n^* f_i d\mathbf{v} \right),\end{aligned} \tag{2.15}$$

where the last two terms represent the frictional transfer of momentum between species. Meier [21] gave the following approximations for these terms

$$m_i \sigma_{cx} n_i \int \mathbf{w} v_i^* f_n d\mathbf{v} \equiv \mathbf{R}_{in}^{cx} \approx -m_i \sigma_{cx} n_i n_n \mathbf{v}_{in} v_{Tn}^2 \left[4 \left(\frac{4}{\pi} v_{Ti}^2 + v_{in}^2 \right) + \frac{9\pi}{4} v_{Tn}^2 \right]^{-1/2}, \tag{2.16}$$

and

$$m_i \sigma_{cx} n_n \int \mathbf{w} v_n^* f_i d\mathbf{v} \equiv \mathbf{R}_{ni}^{cx} \approx +m_i \sigma_{cx} n_i n_n \mathbf{v}_{in} v_{Ti}^2 \left[4 \left(\frac{4}{\pi} v_{Tn}^2 + v_{in}^2 \right) + \frac{9\pi}{4} v_{Ti}^2 \right]^{-1/2}. \tag{2.17}$$

The neutral species charge-exchange contribution is the same as expression above, but with the opposite sign

$$\int m_n \mathbf{v} C_n^{cx} d\mathbf{v} \approx m_i(\mathbf{v}_i - \mathbf{v}_n)\Gamma^{cx} + \mathbf{R}_{ni}^{cx} - \mathbf{R}_{in}^{cx}. \tag{2.18}$$

2^{nd} moments

The second moment of collision operators gives the energy exchange between species under the specific collision process. Contribution of the 2^{nd} moment of ionization collision operator on ions is calculated using split particle velocity as

$$\int \frac{1}{2} m_i \mathbf{v}^2 C_i^{ion} d\mathbf{v} \approx m_i n_e \langle \sigma_{ion} v_e \rangle \left(\frac{1}{2} \mathbf{v}_n^2 \int f_n d\mathbf{v} + \mathbf{v}_n \cdot \int \mathbf{w} f_n d\mathbf{v} + \frac{1}{2} \int \mathbf{w}^2 f_n d\mathbf{v} \right). \tag{2.19}$$

The first term on the right-hand side is related to ionization 0^{th} moment, the second term is an odd integral and vanishes, and the last term is the energy exchange due to random movement of the particles. Meier [21] calculated this integral in spherical coordinates to give

$$\int \mathbf{w}^2 f_n d\mathbf{v} = \frac{3}{2} n_n v_{Tn}^2, \tag{2.20}$$

where it can be identified as transfer of internal energy. Thus, the 2^{nd} moment of ionization collision operator is

$$\int \frac{1}{2} m_i \mathbf{v}^2 C_i^{ion} d\mathbf{v} \approx \frac{m_i}{m_n} \left(\Gamma_i^{ion} \frac{1}{2} m_n \mathbf{v}_n^2 + Q_i^{ion} \right). \tag{2.21}$$

Similarly, the second moment of ionization collision operator for electron species is written as

$$\int \frac{1}{2} m_e \mathbf{v}^2 C_e^{ion} d\mathbf{v} \approx \frac{m_e}{m_n} \left(\Gamma_i^{ion} \frac{1}{2} m_n \mathbf{v}_n^2 + Q_i^{ion} \right) - \Gamma_i^{ion} \phi_{ion}, \tag{2.22}$$

where ϕ_{ion} represents the effective ionization energy. And the ionization collisions affect the neutral energy in the same manner given as

$$\int \frac{1}{2} m_n \mathbf{v}^2 C_n^{ion} d\mathbf{v} \approx - \left(\Gamma_i^{ion} \frac{1}{2} m_n \mathbf{v}_n^2 + Q_i^{ion} \right). \tag{2.23}$$

The same procedure is pursued for recombination contribution to ion, electron, and neutral species and the 2^{nd} moments are presented as

$$\begin{aligned}
&\int \frac{1}{2} m_i \mathbf{v}^2 C_i^{rec} d\mathbf{v} \approx - \left(\Gamma_n^{rec} \frac{1}{2} m_i \mathbf{v}_i^2 + Q_n^{rec} \right), \\
&\int \frac{1}{2} m_e \mathbf{v}^2 C_e^{rec} d\mathbf{v} \approx - \Gamma_n^{rec} \frac{1}{2} m_e \mathbf{v}_e^2, \\
&\int \frac{1}{2} m_n \mathbf{v}^2 C_n^{rec} d\mathbf{v} \approx \Gamma_n^{rec} \left(\frac{1}{2} m_i \mathbf{v}_i^2 + \frac{1}{2} m_e \mathbf{v}_e^2 + Q_n^{rec} \right),
\end{aligned} \tag{2.24}$$

where $Q_i^{rec} \equiv \Gamma_n^{rec} \frac{3}{2} m_i v_{Ti}^2$.

The second moment of the charge-exchange collision operator is

$$\int \frac{1}{2} m_i \mathbf{v}^2 C_i^{cx} d\mathbf{v} \approx \int \frac{1}{2} m_i \sigma_{cx} \mathbf{v}^2 (n_i v_i^* f_n - n_n v_n^* f_i) d\mathbf{v}. \tag{2.25}$$

Splitting the particle velocity into bulk and random components and taking the integrals, the charge-exchange contribution to ions can be written as

$$\int \frac{1}{2} m_i \mathbf{v}^2 C_i^{cx} d\mathbf{v} \approx \Gamma^{cx} \frac{1}{2} m_i (\mathbf{v}_n^2 - \mathbf{v}_i^2) + \mathbf{v}_n \cdot \mathbf{R}_{in} - \mathbf{v}_i \cdot \mathbf{R}_{ni}^{cx} + Q_{in}^{cx} - Q_{ni}^{cx} \tag{2.26}$$

where Q_{in}^{cx} and Q_{ni}^{cx} represent the random thermal energy transfer and are defined as

$$Q_{in}^{cx} \approx \sigma_{cx} m_i n_i n_n \frac{3}{4} v_{Tn}^2 \sqrt{\frac{4}{\pi} v_{Ti}^2 + \frac{64}{9\pi} v_{Tn}^2 + v_{in}^2}, \tag{2.27}$$

and

$$Q_{ni}^{cx} \approx \sigma_{cx} m_i n_i n_n \frac{3}{4} v_{Ti}^2 \sqrt{\frac{4}{\pi} v_{Tn}^2 + \frac{64}{9\pi} v_{Ti}^2 + v_{in}^2}. \tag{2.28}$$

Similarly, the CX contribution for neutrals is

$$\int \frac{1}{2} m_n \mathbf{v}^2 C_n^{cx} d\mathbf{v} \approx \Gamma^{cx} \frac{1}{2} m_i (\mathbf{v}_i^2 - \mathbf{v}_n^2) - \mathbf{v}_n \cdot \mathbf{R}_{in}^{cx} + \mathbf{v}_i \cdot \mathbf{R}_{ni}^{cx} - Q_{in}^{cx} + Q_{ni}^{cx}. \tag{2.29}$$

2.2.1 Three-component model

The fluid description of weakly ionized plasmas can be derived by taking the appropriate moments of the Boltzmann equation. Using the expressions from Braginskii for scattering collision operators and expressions from Meier [21] for reacting collision operators, the following continuity, momentum, and energy conservation laws can be obtained from the first three moments of the kinetic equation.

Continuity

$$\frac{\partial n_e}{\partial t} + \nabla \cdot (n_e \mathbf{v}_e) = \Gamma_i^{ion} - \Gamma_n^{rec}, \tag{2.30}$$

$$\frac{\partial n_i}{\partial t} + \nabla \cdot (n_i \mathbf{v}_i) = \Gamma_i^{ion} - \Gamma_n^{rec}, \tag{2.31}$$

$$\frac{\partial n_n}{\partial t} + \nabla \cdot (n_n \mathbf{v}_n) = \Gamma_n^{rec} - \Gamma_i^{ion}. \tag{2.32}$$

Momentum

$$\begin{aligned} \frac{\partial}{\partial t}(m_e n_e \mathbf{v}_e) + \nabla \cdot (m_e n_e \mathbf{v}_e \mathbf{v}_e + \mathbb{P}_e) = &- q_e n_e (\mathbf{E} + \mathbf{v}_e \times \mathbf{B}) - \mathbf{R}_i^{ie} + \mathbf{R}_e^{en} \\ &+ \Gamma_i^{ion} m_e \mathbf{v}_n - \Gamma_n^{rec} m_e \mathbf{v}_e, \end{aligned} \tag{2.33}$$

$$\begin{aligned} \frac{\partial}{\partial t}(m_i n_i \mathbf{v}_i) + \nabla \cdot (m_i n_i \mathbf{v}_i \mathbf{v}_i + \mathbb{P}_i) = &+ q_i n_i (\mathbf{E} + \mathbf{v}_i \times \mathbf{B}) + \mathbf{R}_i^{ie} + \mathbf{R}_i^{in} + \mathbf{R}_{in}^{cx} - \mathbf{R}_{ni}^{cx} \\ &+ \Gamma_i^{ion} m_i \mathbf{v}_n - \Gamma_n^{rec} m_i \mathbf{v}_i + \Gamma^{cx} m_i (\mathbf{v}_n - \mathbf{v}_i), \end{aligned} \tag{2.34}$$

$$\begin{aligned} \frac{\partial}{\partial t}(m_i n_n \mathbf{v}_n) + \nabla \cdot (m_i n_n \mathbf{v}_n \mathbf{v}_n + \mathbb{P}_n) = &- \mathbf{R}_i^{in} - \mathbf{R}_e^{en} - \mathbf{R}_{in}^{cx} + \mathbf{R}_{ni}^{cx} \\ &+ \Gamma_n^{rec} m_i \mathbf{v} - \Gamma_i^{ion} m_i \mathbf{v}_n + \Gamma^{cx} m_i (\mathbf{v} - \mathbf{v}_n), \end{aligned} \tag{2.35}$$

where q_i and q_e are the ion and the electron charge magnitudes, $\mathbf{R}^{ie}$ is the scattering collisional momentum transfer between ions and electrons presented by Braginskii, and $\mathbf{R}^{in}$ and $\mathbf{R}^{en}$ are the scattering collisional momentum transfer between ion-neutral and electron-neutral, respectively. $\mathbf{R}^{cx}_{in}$ and $\mathbf{R}^{cx}_{ni}$ represent the frictional transfer of momentum between species due to charge exchange defined previously.

Energy

Defining the total fluid energy density as $\epsilon_\alpha \equiv m_\alpha \mathbf{v}_\alpha/2 + p_\alpha/(\gamma-1)$, the total energy (excluding the electromagnetic energy) conservation law for each species can be written as

$$\begin{aligned}\frac{\partial \epsilon_e}{\partial t} + \nabla\cdot(\epsilon_e\mathbf{v}_e + \mathbf{v}_e\cdot\mathbb{P}_e + \mathbf{h}_e) = &- q_e n_e \mathbf{v}_e\cdot\mathbf{E} - \mathbf{v}_e\cdot\mathbf{R}^{ie}_i + \mathbf{v}_e\cdot\mathbf{R}^{en}_e \\ &+ Q^{ie}_e + Q^{en}_e + \frac{m_e}{m_n}Q^{ion}_i \\ &+ \Gamma^{ion}_i\frac{1}{2}m_e\mathbf{v}_n^2 - \Gamma^{rec}_n\frac{1}{2}m_e\mathbf{v}_e^2 - \Gamma^{ion}_i\phi_{ion},\end{aligned} \tag{2.36}$$

$$\begin{aligned}\frac{\partial \epsilon_i}{\partial t} + \nabla\cdot(\epsilon_i\mathbf{v}_i + \mathbf{v}_i\cdot\mathbb{P}_i + \mathbf{h}_i) = &+ q_i n_i \mathbf{v}_i\cdot\mathbf{E} + \mathbf{v}_i\cdot\mathbf{R}^{ie}_i + \mathbf{v}_i\cdot\mathbf{R}^{in}_i + \mathbf{v}_n\cdot\mathbf{R}^{cx}_{in} - \mathbf{v}_i\cdot\mathbf{R}^{cx}_{ni} \\ &+ Q^{ie}_i + Q^{in}_i + \frac{m_i}{m_n}Q^{ion}_i - Q^{rec}_n + Q^{cx}_{in} - Q^{cx}_{ni} \\ &+ \Gamma^{ion}_i\frac{1}{2}m_i\mathbf{v}_n^2 - \Gamma^{rec}_n\frac{1}{2}m_i\mathbf{v}_i^2 + \Gamma^{cx}\frac{1}{2}m_i(\mathbf{v}_n^2 - \mathbf{v}_i^2),\end{aligned} \tag{2.37}$$

$$\begin{aligned}\frac{\partial \epsilon_n}{\partial t} + \nabla\cdot(\epsilon_n\mathbf{v}_n + \mathbf{v}_n\cdot\mathbb{P}_n + \mathbf{h}_n) = &- \mathbf{v}_n\cdot\mathbf{R}^{in}_i - \mathbf{v}_n\cdot\mathbf{R}^{en}_e - \mathbf{v}_n\cdot\mathbf{R}^{cx}_{in} + \mathbf{v}_i\cdot\mathbf{R}^{cx}_{ni} \\ &+ Q^{in}_n + Q^{en}_n - Q^{ion}_i + Q^{rec}_n - Q^{cx}_{in} + Q^{cx}_{ni} - \Gamma^{ion}_i\frac{1}{2}m_n\mathbf{v}_n^2 \\ &+ \Gamma^{rec}_n\left(\frac{1}{2}m_i\mathbf{v}_i^2 + \frac{1}{2}m_e\mathbf{v}_e^2\right) - \Gamma^{cx}\frac{1}{2}m_i(\mathbf{v}_n^2 - \mathbf{v}_i^2),\end{aligned} \tag{2.38}$$

where Q^{ie} is the scattering collisional heat generation presented by Braginskii. Q^{in} and Q^{en} are the scattering heat generation due to ion-neutral and electron-neutral collisions,

respectively. Q_{in}^{cx} and Q_{ni}^{cx} represent the random thermal energy transfer due to charge exchange. And the species heat fluxes presented by $\mathbf{h}_\alpha$, are specified by using a Chapman-Enskog -like expansion of the distribution function given in details by Meier [22].

2.2.2 Two-component model

Three component fluid description of partially ionized plasmas can be simplified under the same idea used for MHD equations to give a more tractable set of equations while it retains the important physics [7]. The electron fluid and ion fluid are combined appropriately to reach a two component fluid model for the partially ionized plasma. Appropriate summation of densities and velocities gives the center-of-mass density and velocity of the single fluid plasma system as

$$\rho = m_e n_e + m_i n_i, \tag{2.39}$$

$$\mathbf{v} = \frac{m_e n_e \mathbf{v}_e + m_i n_i \mathbf{v}_i}{m_e n_e + m_i n_i}. \tag{2.40}$$

Here, the equations are limited to singly charged ions, $q = q_i = -q_e$, and charge neutrality is satisfied, $n = n_i = n_e$. Electron mass is neglected, $m_e \to 0$, and the plasma center-of-mass velocity is approximated by ion velocity $\mathbf{v} \approx \mathbf{v}_i$. Further assumptions are made in numerical implementation of the two component model which will be explained in Sec. 2.3.

Continuity

Adding the ion and the electron number density conservation laws gives the plasma continuity equation along with neutral continuity,

$$\frac{\partial n}{\partial t} + \nabla \cdot (n\mathbf{v}) = \Gamma_i^{ion} - \Gamma_n^{rec}, \tag{2.41}$$

$$\frac{\partial n_n}{\partial t} + \nabla \cdot (n_n \mathbf{v}_n) = \Gamma_n^{rec} - \Gamma_i^{ion}. \tag{2.42}$$

Momentum

Similarly, taking a linear combination of the ion and the electron momentum equations yields the plasma momentum equation accompanying the neutral momentum,

$$\begin{aligned}\frac{\partial}{\partial t}(m_i n\mathbf{v}) + \nabla\cdot(m_i n\mathbf{v}\mathbf{v} + \mathbb{P}) =& \mathbf{j}\times\mathbf{B} + \mathbf{R}_i^{in} + \mathbf{R}_e^{en} + \mathbf{R}_{in}^{cx} - \mathbf{R}_{ni}^{cx} \\ &+ \Gamma_i^{ion} m_i\mathbf{v}_n - \Gamma_n^{rec} m_i\mathbf{v} - \Gamma^{cx} m_i(\mathbf{v}-\mathbf{v}_n),\end{aligned} \tag{2.43}$$

$$\begin{aligned}\frac{\partial}{\partial t}(m_i n_n\mathbf{v}_n) + \nabla\cdot(m_i n_n\mathbf{v}_n\mathbf{v}_n + \mathbb{P}_n) =& -\mathbf{R}_i^{in} - \mathbf{R}_e^{en} - \mathbf{R}_{in}^{cx} + \mathbf{R}_{ni}^{cx} \\ &+ \Gamma_n^{rec} m_i\mathbf{v} - \Gamma_i^{ion} m_i\mathbf{v}_n + \Gamma^{cx} m_i(\mathbf{v}-\mathbf{v}_n).\end{aligned} \tag{2.44}$$

The total pressure tensor is $\mathbb{P} = p\mathbb{I} + \mathbf{\Pi}$ with $\mathbf{\Pi}$ representing the viscous stress tensor. Assuming the same density and temperature for ions and electrons, the components of electron viscous stress tensor are smaller than ion components, therefore, $\mathbf{\Pi} \approx \mathbf{\Pi}_i$ is sufficiently accurate.

Energy

The energy equation for plasma is obtained by adding energy equations for ion and electron fluids assuming negligible electron mass, $m_e \to 0$,

$$\begin{aligned}\frac{\partial\epsilon}{\partial t} + \nabla\cdot(\epsilon\mathbf{v} + \mathbf{v}\cdot\mathbb{P} + \mathbf{h}) =& \mathbf{j}\cdot\mathbf{E} + \mathbf{v}\cdot\mathbf{R}_i^{in} + \mathbf{v}\cdot\mathbf{R}_e^{en} + \mathbf{v}_n\cdot\mathbf{R}_{in}^{cx} - \mathbf{v}\cdot\mathbf{R}_{ni}^{cx} \\ &+ Q_i^{in} + Q_e^{en} + Q_i^{ion} - Q_n^{rec} + Q_{in}^{cx} - Q_{ni}^{cx} \\ &+ \Gamma_i^{ion}\left(\frac{1}{2}m_i v_n^2 - \phi_{ion}\right) - \Gamma_n^{rec}\frac{1}{2}m_i v^2 + \Gamma^{cx}\frac{1}{2}m_i(v_n^2 - v^2),\end{aligned} \tag{2.45}$$

$$\begin{aligned}\frac{\partial\epsilon_n}{\partial t} + \nabla\cdot(\epsilon_n\mathbf{v}_n + \mathbf{v}_n\cdot\mathbb{P}_n + \mathbf{h}_n) =& -\mathbf{v}_n\cdot\mathbf{R}_i^{in} - \mathbf{v}_n\cdot\mathbf{R}_e^{en} - \mathbf{v}_n\cdot\mathbf{R}_{in}^{cx} + \mathbf{v}\cdot\mathbf{R}_{ni}^{cx} \\ &+ Q_n^{in} + Q_n^{en} - Q_n^{ion} + Q_i^{rec} + Q_e^{rec} - Q_{in}^{cx} + Q_{ni}^{cx} \\ &+ \Gamma_n^{rec}\frac{1}{2}m_i v^2 - \Gamma_i^{ion}\frac{1}{2}m_i v_n^2 - \Gamma^{cx}\frac{1}{2}m_i(v_n^2 - v^2).\end{aligned} \tag{2.46}$$

Generalized Ohm's law

Subtracting the appropriate factors of ion and electron momentum equations determines the relative behavior of the electron-ion fluids. Assuming slowly varying phenomena, $\partial/\partial t = 0$, and neglecting terms of order m_e/m_i, the generalized Ohm's law can be written as,

$$\mathbf{E} + \mathbf{v} \times \mathbf{B} = \frac{1}{qn}(-\mathbf{R}_i^{ie} + \mathbf{R}_e^{en}), \tag{2.47}$$

where $\mathbf{R}_i^{ie}$ is the collision term between electrons and ions and $\mathbf{R}_e^{en}$ is the collision term between electrons and neutrals as before.

2.3 NIMNEUT formulation

In this research we use the NIMROD code as the framework for implementing an interactive plasma-neutral model described in Sec. 2.2. In Chap. 3 we discuss the spatial and temporal discretization of the equations in detail. We use the two-component model of plasma-neutral system with some simplifying assumptions given as follows.

Continuity

Numerical solution of the number density equations for plasma and neutral species is prone to artificial oscillations due to discretization of the equations. Here, we use a second order diffusion term to suppress these undesirable oscillations. We also use diffusive layers at the boundaries to specify a specific kind of boundary condition. Details about boundary conditions is given in Sec. 3.4. The final form of number density equations is given as

$$\frac{\partial n}{\partial t} + \nabla \cdot (n\mathbf{v}) - D\nabla^2 n = \Gamma_i^{ion} - \Gamma_n^{rec}, \tag{2.48}$$

$$\frac{\partial n_n}{\partial t} + \nabla \cdot (n_n \mathbf{v}_n) - D_n \nabla^2 n_n = \Gamma_n^{rec} - \Gamma_i^{ion}. \tag{2.49}$$

Momentum

Instead of solving the momentum equation, we evolve the center of mass velocity equation. Multiplying the continuity equation by center of mass velocity and subtracting it from momentum equation we get the velocity evolution as

$$m_i n \left(\frac{\partial \mathbf{v}}{\partial t} + \mathbf{v} \cdot \nabla \mathbf{v} \right) + \nabla p + \nabla \cdot \mathbf{\Pi} = \mathbf{J} \times \mathbf{B} + \mathbf{R}_{in}^{cx} - \mathbf{R}_{ni}^{cx} + \Gamma_i^{ion} m_i (\mathbf{v}_n - \mathbf{v}) + \Gamma^{cx} m_i (\mathbf{v}_n - \mathbf{v}), \tag{2.50}$$

$$m_i n_n \left(\frac{\partial \mathbf{v}_n}{\partial t} + \mathbf{v}_n \cdot \nabla \mathbf{v}_n \right) + \nabla p_n + \nabla \cdot \mathbf{\Pi}_n = \mathbf{R}_{ni}^{cx} - \mathbf{R}_{in}^{cx} + \Gamma_n^{rec} m_i (\mathbf{v} - \mathbf{v}_n) + \Gamma^{cx} m_i (\mathbf{v} - \mathbf{v}_n). \tag{2.51}$$

An important point here is that the momentum transfer due to neutral-charged particle collisions is neglected. Goldston [7] shows that these collisions are relatively unimportant compared to Coulomb collisions even for partially ionized plasmas. Meier [22] suggests that for problems with interesting physics in the low ionization regions, the neutral-charged collisions should be included in the model. All the drag forces due to reactive collisions depend on relative bulk velocity of plasma and neutral species. If the bulk velocities are the same, the distribution functions overlap and the charge exchange frictional forces disappear due to symmetric CX reaction rate.

Energy

Another alteration that we employ in this research is to advance temperature equations instead of total energy density. It is more beneficial to solve for primitive values in implicit/semi-implicit algorithm that we use rather than advancing the conservative forms. Combining the energy density equation with continuity and center of mass velocity equations and doing

some algebra, the temperature equation can be written as

$$\begin{aligned}\frac{n}{\gamma-1}\left(\frac{\partial T}{\partial t}+\mathbf{v}\cdot\nabla T\right) =& -p\nabla\cdot\mathbf{v}-\boldsymbol{\Pi}:\nabla\mathbf{v}-\nabla\cdot\mathbf{h}+\eta J^2\\ &+Q_i^{ion}-Q_n^{rec}+Q_{in}^{cx}-Q_{ni}^{cx}-T(\Gamma_i^{ion}-\Gamma_n^{rec})-\Gamma_i^{ion}\phi_{ion}\\ &+\Gamma_i^{ion}\frac{m_i}{2}(\mathbf{v}-\mathbf{v}_n)^2+\Gamma^{cx}\frac{m_i}{2}(\mathbf{v}-\mathbf{v}_n)^2-\mathbf{R}_{in}^{cx}\cdot(\mathbf{v}-\mathbf{v}_n),\end{aligned} \tag{2.52}$$

$$\begin{aligned}\frac{n_n}{\gamma-1}\left(\frac{\partial T_n}{\partial t}+\mathbf{v}_n\cdot\nabla T_n\right) =& -p_n\nabla\cdot\mathbf{v}_n-\boldsymbol{\Pi}_n:\nabla\mathbf{v}_n-\nabla\cdot\mathbf{h}_n\\ &-Q_i^{ion}+Q_n^{rec}-Q_{in}^{cx}+Q_{ni}^{cx}-T_n(\Gamma_n^{rec}-\Gamma_i^{ion})\\ &+\Gamma_n^{rec}\frac{m_i}{2}(\mathbf{v}-\mathbf{v}_n)^2+\Gamma^{cx}\frac{m_i}{2}(\mathbf{v}-\mathbf{v}_n)^2+\mathbf{R}_{ni}^{cx}\cdot(\mathbf{v}-\mathbf{v}_n).\end{aligned} \tag{2.53}$$

Again, we assume regimes where neutral-charged collisions are relatively negligible compared to coulomb collisions between charged species and drop the neutral-charged particle scattering terms, Q_i^{in} and Q_e^{en}. As discussed before the ionization and recombination effects are captured in Q_i^{ion} and Q_n^{rec} terms, and Q_{in}^{cx} and Q_{ni}^{cx} terms represent thermal energy transfer due to charge exchange. The plasma heat flux, $\mathbf{h}$, is calculated using Braginskii's formula and neutral heat flux is given by $\mathbf{h}_n=-\kappa_n\nabla T_n$, where κ_n is the neutral thermal conductivity. In this research, a uniform constant heat conductivity is assumed for neutral species.

Magnetic induction

Substituting the generalized Ohm's law in Faraday's law yields the magnetic induction equation as

$$\frac{\partial\mathbf{B}}{\partial t}=\nabla\times\left[\mathbf{v}\times\mathbf{B}-\frac{1}{qn}(-\mathbf{R}_i^{ie}+\mathbf{R}_e^{en})\right], \tag{2.54}$$

where $\mathbf{R}_i^{ie}$ is the frictional drag term, and $\mathbf{R}_e^{en}$ is the electron-neutral scattering term. As discussed before, the electron-neutral scattering term is relatively unimportant and neglected. Also, the frictional term is assumed to be isotropic resistive drag, $\eta\mathbf{J}$, where the resistivity is considered to be constant or calculated by the Spitzer formula.

Chapter 3

NUMERICAL MODEL

Finding the analytic solution for the nonlinear equations of plasma-neutral systems is extremely challenging, if not impossible. Numerical methods come into play to replace partial differential equations with algebraic systems and present the solution in a discretized space. Numerical solutions allow to construct an approximation u_N of the exact solution u of a given PDE and to evaluate the error between exact and approximate solution $u - u_N$. There are different schemes on numerical methods, each suitable to approach certain types of problems. The finite element method is a powerful category of numerical techniques in fluid dynamics, although the initial developments were targeting structural mechanics. The method is a generalization of the classical variational and weighted-residual methods, which are based on the idea that the solution u of a differential equation can be represented as a linear combination of unknown parameters c_j and appropriately selected functions ϕ_j in the entire domain of the problem [27]. In this chapter, we review the governing equations and numerical tool used to solve them.

The numerical tool used in this research is a well established extended MHD solver called NIMROD, the Non-Ideal Magnetohydrodynamics with Rotation — Open Discussion [33]. This solver is a continuous Galerkin finite element code which is tailored for devices with toroidally symmetric geometries. Poloidal cross-section can be complicated and represented by a weighted-residual finite element method, where the toroidal direction is described using truncated Fourier expansion. NIMROD solves the single fluid form of velocity moments of the electron and ion distribution functions, neglecting terms of order m_e/m_i smaller than other terms coupled to Maxwell equations without displacement current [32].

3.1 Governing equations

In Chap. 2 we present a complete set of governing equations, Eqs. (2.48) – (2.54), for an interactive plasma-neutral model and in Sec. 2.3 we tailor the equations to be compatible with the framework in NIMROD code. In this representation we separate the steady-state part from the perturbed parts in the solution of the fields, i.e., we evolve perturbations around an equilibrium state. The reason for this decomposition can be found in relative magnitudes of the perturbations and the steady fields. Since the perturbations can be orders of magnitude smaller than steady fields, not having decomposition would require enormous accuracy. However, decomposition adds to the complexity and computational cost. Letting $\partial/\partial t \to 0$ gives the steady state equations which can be solved to find the Grad-Shafranov equilibrium. Next, we look into spatial and temporal discretization of the governing equations.

3.2 Spatial discretization

A finite-dimensional spatial representation is achieved through a basis function expansion and a weak form of the marching equations that is equivalent to a collection of variational problems [33]. Two dimensional Lagrange-type finite elements is chosen to present arbitrary shaped regions of poloidal plane and for the remaining direction, which is periodic, the finite Fourier series is an approximate expansion. The collection of variational problems is expressed in both cylindrical (R, Z, φ) and Cartesian (x, y, z) coordinates as shown in Fig. 3.1.

3.2.1 Fourier representation

We use a pseudo-spectral method to represent the periodic direction of the domain. A truncated Fourier representation of the solution fields is used in the numerical computation given as

$$A(\phi) = A_0 + \sum_{n=1}^{N} \left(A_n e^{in\phi} + A_n^* e^{-in\phi} \right), \tag{3.1}$$

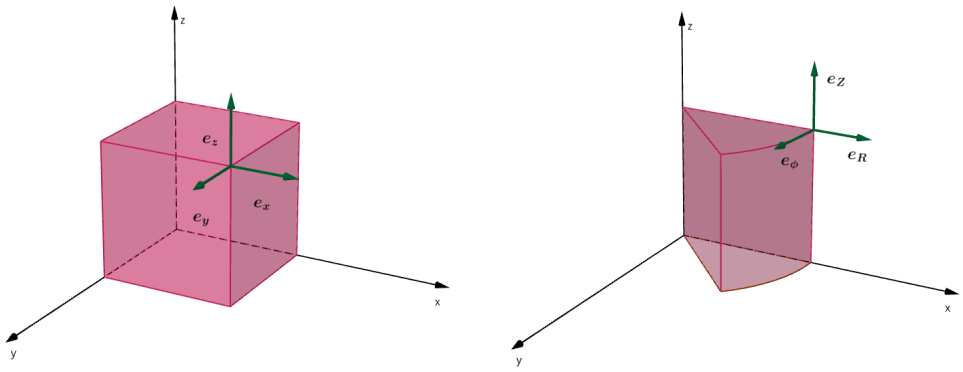

(a) Unit vectors in linear geometry, (b) Unit vectors in toroidal geometry.

Figure 3.1: Both linear and toroidal geometries can be considered using the code in this research. All equations are expressed in (R, Z, ϕ and (X, Y, Z) coordinates with unit vectors shown above. It should be noticed that the toroidal coordinate system here is different from usual cylindrical coordinate system.

where all the fields are real functions of space and we solve for complex coefficients A_n [32]. Using Fourier transform brings computational benefits in solving complicated systems; for instance, in nonlinear simulations where the Fast Fourier Transform (FFT) is used to compute fields products, orthogonality of basis functions decouples Fourier modes leading to simpler systems, and modal analysis of the solution fields can be performed more easily.

3.2.2 Continuous finite element representation

To complete the spatial representation finite element discretization is used for arbitrary cross-section regions in the poloidal, i.e., R-Z, plane. Similar to Fourier representation, finite element scheme is based on basis function expansion. In this manner, governing equations become a set of discrete equations describing the evolution of the coefficients of the basis

functions. In the finite element scheme, solutions are described of the form

$$A(R,Z) = \sum_j A_j \alpha_j(R,Z), \tag{3.2}$$

where α_j represents the basis function which is a low-order polynomial over each element [32]; for instance a continuous linear basis function in one dimension is given as

$$\alpha_j(x) = \begin{cases} 0 & x < x_{j-1} \\ \frac{x-x_{j-1}}{x_j - x_{j-1}} & x_{j-1} \le x \le x_j \\ \frac{x_{j+1}-x}{x_{j+1}-x_j} & x_j \le x \le x_{j+1} \\ 0 & x > x_{j+1} \end{cases} \tag{3.3}$$

Two-dimensional basis functions are formed as products of 1D basis functions for R and Z. Continuous finite element requires a continuous solution space; however, derivatives need to be piece wise continuous only. This representation only works in uniform meshes, hence, nonuniform meshes are mapped from logical coordinates to physical coordinates.

Combining both Fourier and finite element representations, the scalars are expanded in this scheme as

$$S(R,Z,\phi) = \sum_j \alpha_j(R,Z) \left[S_{j0} + \sum_{n=1}^{N} \left(S_{jn} e^{in\phi} + S_{jn}^* e^{-in\phi} \right) \right], \tag{3.4}$$

and the vectors are expanded similarly

$$\mathbf{V}(R,Z,\phi) = \sum_j \sum_l \alpha_j(R,Z) \hat{e}_l \left[V_{jl0} + \sum_{n=1}^{N} \left(V_{jln} e^{in\phi} + V_{jln}^* e^{-in\phi} \right) \right], \tag{3.5}$$

where $\hat{e}_l$ is the direction vector and $*$ represents the complex conjugate of the fields. For simplicity, we suppress complex conjugate terms and make n sum from 0 to N where $N = (number\ of\ Fourier\ modes - 1)$. The weak formulation is obtained by taking the inner product of the governing equations with the set of test functions, which for the Galerkin method are the same as basis functions. The inner product convention for complex functions u and v is defined as the integral over the finite element domain Ω

$$\langle u, v \rangle = \int_\Omega \bar{v} u \, d\Omega. \tag{3.6}$$

As an example, for variable S the weak form integral can be written as

$$\begin{aligned}\langle \varphi_{jn} S_{jn}, \varphi_{im} \rangle &= \int_\Omega \bar{\varphi}_{im} \varphi_{jn} S_{jn} \; d\Omega \\ &= \int_\Omega \alpha_i \exp^{-ik_m\phi} \alpha_j \exp^{ik_n\phi} \; S_{jn} \; d\Omega \\ &= \int_\Omega \alpha_i \alpha_j \exp^{i(k_n - k_m)\phi} \; S_{jn} \; d\Omega.\end{aligned} \tag{3.7}$$

This integral can be separated into integration over the (R, Z) plane, denoted by Ω, and integration over the periodic dimension ϕ. When integrating the latter we assume that $\phi \in [0, 1]$ and that the modes have wavelengths $k_m \in \{2\pi m : m \in \mathbb{Z}\}$, which makes $\exp(ik_m\phi)$ an orthonormal basis.

$$\begin{aligned}\int_\Omega \alpha_i \alpha_j \exp^{i(k_n - k_m)\phi} \; S_{jn} \; d\Omega &= \int_{\Omega'} \alpha_i \alpha_j \int_0^1 \exp^{i(k_n - k_m)\phi} \; S_{jn} \; d\theta \; d\Omega' \\ &= \int_{\Omega'} \alpha_i \alpha_j \; S_{jn} \; \delta_{nm} \; d\Omega' \\ &= \int_{\Omega'} \alpha_i \alpha_j \; S_{jm} \; d\Omega'.\end{aligned} \tag{3.8}$$

Thus, orthogonality of the Fourier basis allows the 3D integral to be reduced to a set of 2D integrals, each associated with an independent mode m. In this particular case, the 2D integral is independent of m so the integral (the mass matrix) needs only to be evaluated once. However, this should not obscure the fact that we have a three-dimensional coefficient matrix S_{jm}.

3.3 Time Discretization

When developing discrete models for resistive MHD, the extreme temporal stiffness exhibited by the normal modes of the MHD equations becomes a challenging issue. This property is measured by the Lundquist number, $S = \tau_R/\tau_A$, which represents the ratio of resistive diffusion characteristic time to the Alfvén characteristic time. Since it is necessary to track phenomena with highly different (by 5–10 orders of magnitude) characteristic time scales, numerical method requires special time differencing algorithms [29]. Including atomic in-

teractions in plasma equations introduces additional stiff coupling through effects such as ionization, recombination and charge exchange.

It is shown that using a mixed implicit/semi-implicit leapfrog method [34] to discretize the MHD equations can bridge the fast-wave and slow-diffusive time scales. Consider the functional dependencies for single-fluid MHD without atomic interactions: $n(\mathbf{V})$, $\mathbf{V}(n, \mathbf{B}, T)$, $T(n, \mathbf{V})$, and $\mathbf{B}(\mathbf{V})$. This data dependence allows for time-splitting by field and sequential field solves which reduces the complexity and computational cost of implicit algorithms. In the semi-implicit leapfrog algorithm the velocity field is staggered with respect to the other fields which are solved sequentially [33]. In order to stabilize wave propagation associated with the leapfrog algorithm, it is essential to include a semi-implicit operator [30] which is added to the velocity advance equation in the NIMROD code. Using the ideal-MHD force operator limits spectral-pollution time-discretization error [20]. Applying this algorithm to MHD formulation the semi-discrete equations can be written as

$$\frac{\Delta n}{\Delta t} + \frac{1}{2}\nabla\cdot(\mathbf{v}^{j+1}\Delta n) - \frac{1}{2}D\nabla^2\Delta n = -\nabla\cdot(\mathbf{v}^{j+1}n^{j+1/2}) + D\nabla^2 n^{j+1/2}, \tag{3.9}$$

$$\begin{aligned} m_i n^{j+1/2}\left(\frac{\Delta\mathbf{v}}{\Delta t} + \frac{1}{2}\mathbf{v}^j\cdot\nabla\Delta\mathbf{v} + \frac{1}{2}\Delta\mathbf{v}\cdot\nabla\mathbf{v}^j + \frac{1}{4}\Delta\mathbf{v}\cdot\nabla\Delta\mathbf{v}\right) = \\ \mathbf{J}^{j+1/2}\times\mathbf{B}^{j+1/2} - m_i n^{j+1/2}\mathbf{v}^j\cdot\nabla\mathbf{v}^j - \nabla p^{j+1/2} - \nabla\cdot\mathbf{\Pi}^{j+1/2}(\mathbf{v}^j), \end{aligned} \tag{3.10}$$

$$\begin{aligned} \frac{3\bar{n}}{2}\left(\frac{\Delta T_\alpha}{\Delta t} + \frac{1}{2}\mathbf{v}_\alpha^{j+1}\cdot\nabla\Delta T_\alpha\right) + \frac{1}{2}\bar{n}\Delta T_\alpha\nabla\cdot\mathbf{v}_\alpha^{j+1} + \frac{1}{2}\nabla\cdot[\mathbf{q}_\alpha(\Delta T_\alpha)] = \\ -\frac{3\bar{n}}{2}\mathbf{v}_\alpha^{j+1}\cdot\nabla\Delta T_\alpha^{j+1/2} - \bar{n}T_\alpha^{j+1/2}\nabla\cdot\mathbf{v}_\alpha^{j+1} - \nabla\cdot[\mathbf{q}_\alpha(T_\alpha^{j+1/2})] + Q_\alpha^{j+1/2}, \end{aligned} \tag{3.11}$$

$$\begin{aligned} \frac{\Delta\mathbf{B}}{\Delta t} + \nabla\times\left(\frac{m_e}{\mu_0\bar{n}e^2}\nabla\times\frac{\Delta\mathbf{B}}{\Delta t}\right) - \frac{1}{2}\nabla\times(\mathbf{v}^{j+1}\times\Delta\mathbf{B}) \\ + \frac{1}{2}\nabla\times\frac{1}{\bar{n}e}\left(\mathbf{J}^{j+1/2}\times\Delta\mathbf{B} + \Delta\mathbf{J}\times\mathbf{B}^{j+1/2} + \frac{1}{2}\Delta\mathbf{J}\times\Delta\mathbf{B}\right) + \frac{1}{2}\nabla\times\eta\Delta\mathbf{J} = \\ -\nabla\times\left[\frac{1}{\bar{n}e}(\mathbf{J}^{j+1/2}\times\mathbf{B}^{j+1/2} - \bar{T}_e\nabla\bar{n}) - \mathbf{v}^{j+1}\times\mathbf{B}^{j+1/2} + \eta\mathbf{J}^{j+1/2}\right], \end{aligned} \tag{3.12}$$

where superscripts indicate time-level indices, Δ indicates the change over a step, and overbars indicate the average of the beginning and end of a step.

The inclusion of atomic interactions breaks the functional structure of the MHD equations that lead to this discretization. However, we can still use this algorithm as the underlying base to advance fluid equations for each species. Similar to the plasma advance, the leapfrog algorithm staggers the neutral velocity field with respect to the other fields. Analogously, a semi-implicit operator is required to stabilize the sound-wave propagation. Following the discretization steps taken for plasma equations, the semi-discrete form of the neutral equations without atomic interactions can be written as

$$\frac{\Delta n_n}{\Delta t} + \frac{1}{2}\nabla\cdot(\mathbf{v}_n^{j+1}\Delta n_n) - \frac{1}{2}D_n\nabla^2\Delta n_n = -\nabla\cdot(\mathbf{v}_n^{j+1}n_n^{j+1/2}) + D_n\nabla^2 n_n^{j+1/2}, \tag{3.13}$$

$$\begin{aligned} m_i n_n^{j+1/2}\left(\frac{\Delta\mathbf{v}_n}{\Delta t} + \frac{1}{2}\mathbf{v}_n^j\cdot\nabla\Delta\mathbf{v}_n + \frac{1}{2}\Delta\mathbf{v}_n\cdot\nabla\mathbf{v}_n^j + \frac{1}{4}\Delta\mathbf{v}_n\cdot\nabla\Delta\mathbf{v}_n\right) = \\ - m_i n_n^{j+1/2}\mathbf{v}_n^j\cdot\nabla\mathbf{v}_n^j - \nabla p_n^{j+1/2} - \nabla\cdot\mathbf{\Pi}_n^{j+1/2}(\mathbf{v}_n^j), \end{aligned} \tag{3.14}$$

$$\begin{aligned} \frac{3\bar{n}_n}{2}\left(\frac{\Delta T_n}{\Delta t} + \frac{1}{2}\mathbf{v}_n^{j+1}\cdot\nabla\Delta T_n\right) + \frac{1}{2}\bar{n}_n\Delta T_n\nabla\cdot\mathbf{v}_n^{j+1} + \frac{1}{2}\nabla\cdot[\mathbf{q}_n(\Delta T_n)] = \\ - \frac{3\bar{n}_n}{2}\mathbf{v}_n^{j+1}\cdot\nabla\Delta T_n^{j+1/2} - \bar{n}_n T_n^{j+1/2}\nabla\cdot\mathbf{v}_n^{j+1} - \nabla\cdot[\mathbf{q}_n(T_n^{j+1/2})] + Q_n^{j+1/2}, \end{aligned} \tag{3.15}$$

There are different ways that we can incorporate the atomic physics between plasma and neutral species in the same framework of semi-implicit leapfrog algorithm. Here we consider two competing approaches:

1. coupling the neutral species to the plasma through a time-centered Crank-Nicolson approach

2. introducing additional operator-splitting for the atomic physics interactions.

Section 3.3.1 details an algorithm with Crank-Nicolson time centering of the linear contributions to the atomic physics terms. In Sec. 3.3.2, we describe Newton iteration that adds nonlinear contributions to the Crank-Nicolson time centering as required for an accurate and stable algorithm. Alternatively, as a different approach Sec. 3.3.3 gives details of an operator-splitting algorithm. Next, we will introduce a Douglas-Rachford inspired splitting in the Strang-split method to mitigate operator splitting error. Finally, we discuss different sources of error in both methods and possible cause for them.

3.3.1 Crank-Nicolson time-centering within semi-implicit leapfrog algorithm

Following Refs. [33] and [34], the discrete form of an implicit/semi-implicit numerical time-advance for the number density equation of the plasma-neutral model is

$$\begin{aligned}\frac{\Delta n}{\Delta t} + \theta\nabla\cdot[\mathbf{V}^{j+1}\Delta n] - \theta\Gamma_1^{ion}(\Delta n, \Delta n_n, n^{j+\frac{1}{2}}, n_n^{j+\frac{1}{2}}, T^{j+\frac{1}{2}}) + \theta\Gamma_1^{rec}(\Delta n, n^{j+\frac{1}{2}}, T^{j+\frac{1}{2}}) \\ = -\nabla\cdot[\mathbf{V}^{j+1}n^{j+\frac{1}{2}}] + \Gamma_0^{ion}(n^{j+\frac{1}{2}}, n_n^{j+\frac{1}{2}}, T^{j+\frac{1}{2}}) - \Gamma_0^{rec}(n^{j+\frac{1}{2}}, T^{j+\frac{1}{2}})\end{aligned} \tag{3.16}$$

$$\begin{aligned}\frac{\Delta n_n}{\Delta t} + \theta\nabla\cdot[\mathbf{V}_n^{j+1}\Delta n_n] + \theta\Gamma_1^{ion}(\Delta n, \Delta n_n, n^{j+\frac{1}{2}}, n_n^{j+\frac{1}{2}}, T^{j+\frac{1}{2}}) - \theta\Gamma_1^{rec}(\Delta n, n^{j+\frac{1}{2}}, T^{j+\frac{1}{2}}) \\ = -\nabla\cdot[\mathbf{V}_n^{j+1}n_n^{j+\frac{1}{2}}] - \Gamma_0^{ion}(n^{j+\frac{1}{2}}, n_n^{j+\frac{1}{2}}, T^{j+\frac{1}{2}}) + \Gamma_0^{rec}(n^{j+\frac{1}{2}}, T^{j+\frac{1}{2}})\end{aligned} \tag{3.17}$$

where the superscript shows the discrete step label, Δn is the change in number density, $n^{j+3/2} - n^{j+1/2}$, and θ is the centering parameter. $\mathbf{V}$ is centered in the density advance through the leapfrog algorithm. In this work Crank-Nicolson centering of $\theta = 1/2$ is used for the hyperbolic and atomic reaction terms. Reference [34] shows that time centering of $\theta = 1/2$ for advection terms is required to maintain numerical stability for the MHD advance.

Equations (3.16) and (3.17) are coupled through atomic reactions between plasma and neutrals. To clearly present the discrete form of atomic physics we expand the ionization and recombination source terms around a time-step as $\Gamma^*(n + \theta\Delta n) = \Gamma_0^*(n) + \theta\Gamma_1^*(n, \Delta n, \theta) + \Gamma_{nl}^*(n, \Delta n, \theta)$ where Γ_0^* is the full source term at the beginning of time-step, Γ_1^* is the linear contribution of atomic physics due to change in the field, and Γ_{nl}^* represents the nonlinear contribution of the field change in atomic physics source terms. For example, the expansion of the ionization source term in plasma number density equation can be presented as

$$\Gamma^{ion}(n + \theta\Delta n, n_n + \theta\Delta n_n) = \langle\sigma_{ion}v\rangle n n_n + \theta\langle\sigma_{ion}v\rangle\Delta n\ n_n + \theta\langle\sigma_{ion}v\rangle n\ \Delta n_n + \Gamma_{nl}^{ion} \tag{3.18}$$

where $\Gamma_0^{ion} = \langle\sigma_{ion}v\rangle n n_n$, $\Gamma_1^{ion} = \langle\sigma_{ion}v\rangle\Delta n\ n_n + \langle\sigma_{ion}v\rangle n\ \Delta n_n$, and $\Gamma_{nl}^{ion} = \Gamma^{ion} - \Gamma_0^{ion} - \theta\Gamma_1^{ion}$. The Γ_1^* term does not include a linear contribution from the cross-section, $\langle\sigma v\rangle$, which may be density dependent. This choice is made as the functional form of the cross-section is not known a priori. These contributions are included in Γ_{nl}^* which will be addressed in Sec. 3.3.2.

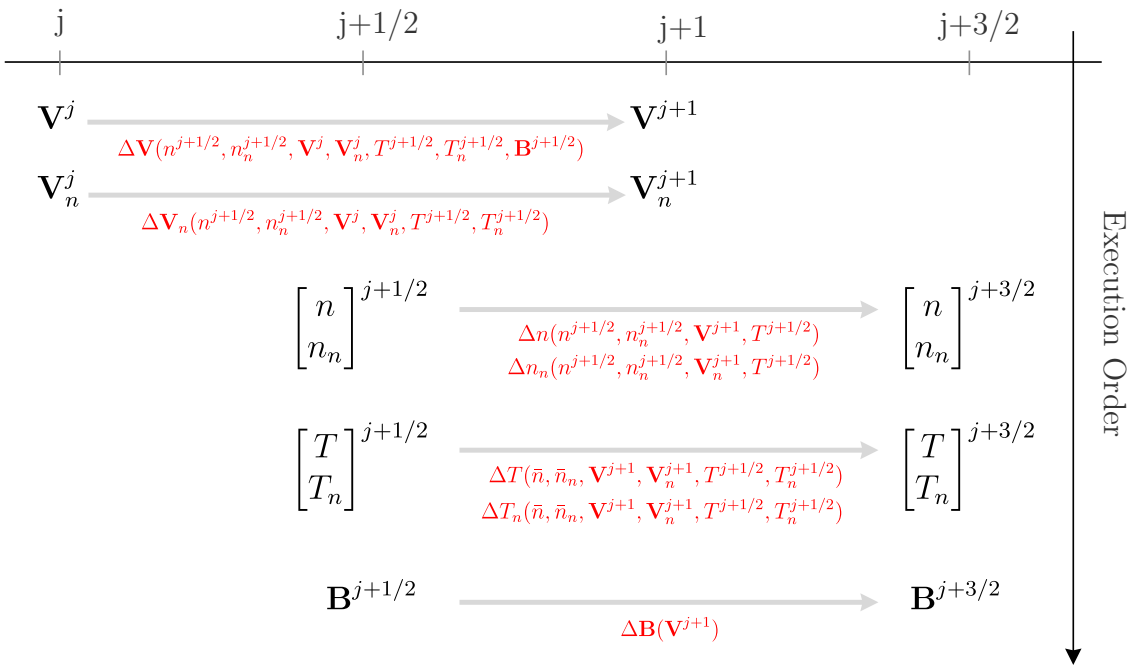

Figure 3.2: Schematic of Crank-Nicolson time advance. By exploiting the functional structure of MHD equations, velocity, number density, temperature, and magnetic field advances can be staggered and solved sequentially using the semi-implicit leapfrog algorithm. Plasma and neutral velocities are solved separately where number densities and temperatures for both species are solved simultaneously.

Turning to the full system of equations, Fig. 3.2 shows the time staggering and data dependency schematically. Velocity is staggered in time with respect to number density, temperature, and magnetic field which are solved sequentially. The ordering of the sequential solves is based on the MHD data dependencies. However, including neutral-plasma atomic interaction breaks this data dependency between number density and temperature equations when the cross-section depends on temperature as is common. Explicit centering of temperature in the number density equation amplifies the time-discretization error associated with temperature-dependent cross-sections. We refer to this error as *T-in-n* error.

While the linearized velocity fields for plasma and neutral species are solved independently here, we add full CN time-centering to them through nonlinear terms in Newton iteration as detailed in Sec. 3.3.2. Square bracket notation in Fig. 3.2 implies that the species are dependent on each other for the specified field and are solved simultaneously. Although we could solve the number density and temperature equations simultaneously to eliminate the *T-in-n* error, we choose not to due to implementation complexity, computational cost and potential issues with system-size scaling with the number of atomic species.

3.3.2 Newton iteration for nonlinear terms in Crank-Nicolson method

We now turn to how a Newton method is applied for the nonlinear terms (and a small subset of linear terms as mentioned in Sec. 3.3.1). The nonlinear dynamics of plasma-neutral interactions at low temperature plasmas ($\sim 1-5$ [eV]) mostly depend on the atomic reaction cross-section rates which are calculated by DEGAS2 code and computed via bi-cubic spline interpolation from a table. The Newton method is a straight forward algorithm to include nonlinear terms in the time advance.

For completeness, we briefly summarize Newton's method presented in Ref. [15], while also highlighting specific implementation details. Consider a nonlinear system of equations given as $dx/dt = g(x)$, where $g(x)$ is a general nonlinear function of x. We discretize the equation using the Crank-Nicolson time-centering scheme. Expanding the nonlinear function

with Taylor series, we get

$$\Delta x - \Delta t \left[g(x^n) + \frac{1}{2}\Delta \mathbf{u}\ g'(x^n) + g_{nl}(x^n, \Delta x) \right] = 0, \tag{3.19}$$

where prime notation presents the derivative with respect to variable x. g_{nl} incorporates all the high order terms in the Taylor expansion and can be simply calculated using the Taylor expansion definition,

$$g_{nl}(x^n, \Delta x) = g(x^n + \frac{1}{2}\Delta x) - g(x^n) - \frac{1}{2}\Delta x\ g'(x^n). \tag{3.20}$$

Considering that $g(x)$ can be a system of equations, we expand the definition of g_{nl} to include the inter-species interaction terms from $g'(x^n)$, cross-section derivatives, and the nonlinear part of the Taylor expansion. The inter-species velocity advance equations are CN-time-centered through nonlinear Newton iteration eliminating the limitation discussed in linear Crank-Nicolson algorithm in Sec. 3.3.1. An independent linear solve of the velocity fields avoids the need for a 6-component vector solve which reduces the complexity and cost of the numerical solver.

A Newton-Krylov method is used to solve the linear part of the system of equations. After simplifying and rearranging Eq. (3.19), the Newton sequence to find the root is given as

$$\left[1 - \frac{1}{2}\Delta t\ g'(x^n) - \Delta t\ \frac{\partial g_{nl}(x^n, \Delta x_k)}{\partial \Delta x_k} \right] \Delta x_{k+1} = \Delta t \left[g(x^n) + g_{nl}(x^n, \Delta x_k) - \Delta x_k \frac{\partial g_{nl}(x^n, \Delta x_k)}{\partial \Delta x_k} \right] \tag{3.21}$$

where dot notation shows the derivative with respect to Δx, x^n represents the variables at time step n, and Δx_k is the change in the variables at iteration k. Since $g_{nl}(x^n, \Delta x_k)$ has no analytic form with tabular atomic physics cross-sections, a simple finite difference approximation is used to find its Jacobian as

$$\frac{\partial g_{nl}(x, \Delta x)}{\partial \Delta x} = \frac{g_{nl}(x, \Delta x) - g_{nl}(x, (1-\epsilon)\Delta x)}{\epsilon \Delta x}. \tag{3.22}$$

An error estimate is required to test convergence, and in most cases the norm of Eq. (3.19) can be used to show the decay rate in error [15]. Accordingly, the convergence criterion

considered for the nonlinear Newton iteration is

$$\frac{\|[1-\frac{1}{2}\Delta t\ g'(x^n)]\Delta x^k - \Delta t\ g(x^n) - \Delta t\ g_{nl}(x^n,\Delta x^k)\|}{\|\Delta t\ g(x^n)\|} < tol_{nl} \tag{3.23}$$

where tol_{nl} is the nonlinear solver tolerance.

At large time-step size, linearized operators can cause large overshoots relative to the solution during nonlinear iteration. Although the numerical schemes can recover the overshoot and find the correct steady-state solution, in fluid dynamics simulations these overshoots can cause physically impossible solutions such as negative pressure which often terminates the simulation. A "dynamic" floor is implemented to keep number density and temperature positive during iteration. Another knob used to control the Newton nonlinear iterations is relaxing the solution, in which a relaxation factor limits how far the new guess for Δx can be from the previous solution.

3.3.3 Strang-split time advance within the semi-implicit leapfrog algorithm

The semi-implicit leapfrog with Crank-Nicolson centering handles the MHD-fluid dynamics and atomic reactions simultaneously. An alternative approach is operator splitting the atomic physics from fluid dynamics. Additional operator splitting is in the spirit of leapfrog algorithm. In this method the spatially local atomic reactions (ODE system) is advanced half time-step. Then the MHD-fluid equations (PDE system) evolves a full time-step using the semi-implicit leapfrog algorithm. Finally, the ODE system is advanced for another half time-step to complete the Strang-split algorithm. General form of the iteration for this method is given by

$$\begin{aligned} x^{(j+1,j+1/2)} &= \mathcal{S}_{\text{ode}}\left(\frac{\Delta t}{2}, x^{(j+1/2,j+1/2)}\right), \\ x^{(j+1,j+3/2)} &= \mathcal{S}_{\text{pde}}\left(\Delta t, x^{(j+1,j+1/2)}\right), \\ x^{(j+3/2,j+3/2)} &= \mathcal{S}_{\text{ode}}\left(\frac{\Delta t}{2}, x^{(j+1,j+3/2)}\right), \end{aligned} \tag{3.24}$$

where x is one of fields n, $\mathbf{V}$, or T. $\mathcal{S}_{\text{pde}}$ represents the solution to PDE system with Crank-Nicolson time-centering similar to the solution presented in Sec. 3.3.1, but the atomic

interactions are neglected. $\mathcal{S}_{\text{ode}}$ is the numerical solution for the ODE system representing the atomic reactions between species using a time-adaptive Adam-Bashforth method. The first superscript represents the ODE time index, where the second one denotes the time indexing for the PDE contribution.

Consider the plasma density equation, Eq. (2.48), as an example. Operator splitting divides the solution into two parts: one part is the solution to the ODE system given by

$$\frac{\partial n}{\partial t} = \Gamma^{ion} - \Gamma^{rec}, \tag{3.25}$$

and the other part is the solution to the PDE system given by the nonlinear equation

$$\frac{\partial n}{\partial t} + \nabla \cdot (n\mathbf{V}) = 0. \tag{3.26}$$

In this algorithm the coupling between species is captured in the ODE system of equations. Within the scope of the semi-implicit leapfrog algorithm, the Strang operator splitting is applied to n, $\mathbf{V}$ and T separately.

Figure 3.3 shows a schematic view of the SS-field time advance for plasma and neutral number density equations. Away from the equilibrium point the atomic reactions are local processes that happen on much faster time-scales compared to typical MHD-fluid waves which makes the ODE problem stiff. There are plenty of high quality methods developed for this type of problems. Here we use a stiff/non-stiff ODE solver, `lsode`, with Adams methods [23]. Since plasma and neutral species are only coupled through atomic reactions, operator splitting makes the fields in the MHD-fluid dynamics independent. As a result, the global sparse matrices for the implicit solve become smaller, reducing the numerical cost for the PDE part of the problem.

Field separation and sequential solve is still in the SS-field method, thus it does not resolve the *T-in-n* error. All the nonlinearities in the atomic physics are captured in the ODE solver, thus SS-field method eliminates any error related to nonlinear dynamics in the source terms.

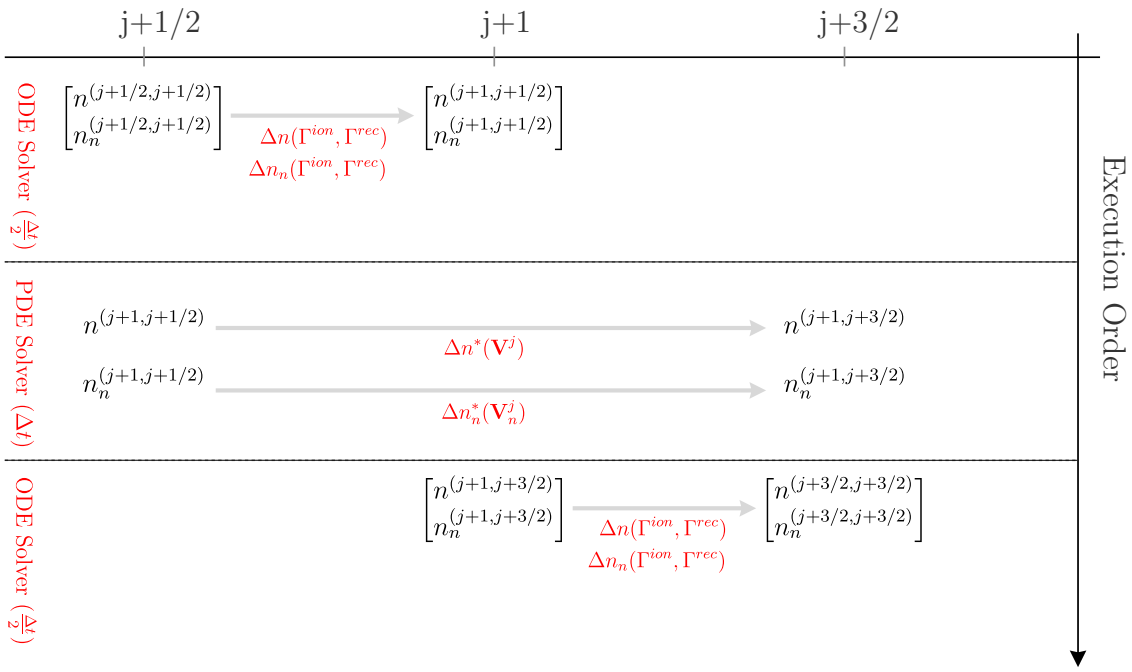

Figure 3.3: Schematic of SS-field time advance for number density equation. Local atomic physics are captured by the ODE system of equations where the PDE system represents the MHD-fluid equations for plasma and neutral species. Since plasma-neutral interactions are captured in local ODEs, the PDE equations can be solved independently.

3.3.4 Strang-split time advance within the leapfrog with Douglas-Rachford inspired coupling

Now we focus on an alternative splitting method which improves the SS-field method in two aspects. First, the Strang-split is interleaved into the leapfrog where all fields are integrated simultaneously by the ODE solver which eliminates the *T-in-n* error. Second, incorporation of a correction source term inspired by Douglas-Rachford coupling [5] that reduces the error associated with ODE/PDE splitting. We will discuss more details about different errors in Sec. 3.3.5.

Before discussing the details of the implementation, let us explain the Douglas-Rachford splitting. In their paper [5], Douglas and Rachford focus on solving dynamic heat equation given by

$$\frac{\partial u}{\partial t} = \frac{\partial^2 u}{\partial x^2} + \frac{\partial^2 u}{\partial y^2}, \tag{3.27}$$

with Dirichlet boundary condition (we ignore the boundary condition for simplicity). Considering a rectangular grid, they approximate the second derivatives by a simple finite difference scheme as

$$Au = \frac{\partial^2 u}{\partial x^2} \approx \frac{u^n_{i+1,j} - 2u^n_{i,j} + u^n_{i-1,j}}{h^2}, \tag{3.28}$$

$$Bu = \frac{\partial^2 u}{\partial y^2} \approx \frac{u^n_{i,j+1} - 2u^n_{i,j} + u^n_{i,j-1}}{h^2}, \tag{3.29}$$

and finally, they represent the problem as

$$\frac{\partial u}{\partial t} = (A + B)u. \tag{3.30}$$

To solve this equation in time, Douglas and Rachford propose the following iteration:

$$\begin{aligned} Av^{n+1} + Bu^n &= \frac{v^{n+1} - u^n}{\tau}, \\ Bu^{n+1} &= Bu^n + \frac{u^{n+1} - v^{n+1}}{\tau}, \end{aligned} \tag{3.31}$$

where we can eliminate v^{n+1} by substituting the first equation into the second one and we get

$$(A + B)u^{n+1} = \frac{u^{n+1} - u^n}{\tau} + \tau AB(u^{n+1} - u^n). \tag{3.32}$$

Equation 3.32 is an implicit Euler method with a correction term, $\tau AB(u^{n+1} - u^n)$. This method was actually proposed to reduce the computational cost of inverting a matrix for linear solve by reducing the bandwidth of the matrix.

Inspired by the correction term in Douglas-Rachford iteration, we add a correction source term to each operator in Strang-split method to control the growth of variables in each separate advance. Consider the full system of plasma-neutral equations as

$$\frac{d\mathbf{u}}{dt} = \mathcal{A}_1(\mathbf{u}) + \mathcal{A}_2(\mathbf{u}), \tag{3.33}$$

where $\mathcal{A}_1$ is the generalized form of Eq. (3.25) for all the fields in which the ODE equations describe the nonlinear local atomic physics and $\mathcal{A}_2$ is the generalized form of Eq. (3.26) representing the linearized MHD-fluid system of equations. Adding Douglas-Rachford inspired coupling with a Strang-splitting interleaved into the leapfrog algorithm gives the following iteration

$$\begin{aligned}
\mathbf{u}^{(j+1/2,j)} &= \mathcal{S}_{\text{ode}}\left(\frac{\Delta t}{2}, \mathbf{u}_0', \mathbf{u}^{(j,j)}\right) \\
\mathbf{u}^{(j+1/2,j+1)} &= \mathcal{S}_{\text{pde}}\left(\Delta t, \mathbf{u}_0', \mathbf{u}^{(j+1/2,j)}\right) \\
\mathbf{u}^{(j+1,j+1)} &= \mathcal{S}_{\text{ode}}\left(\frac{\Delta t}{2}, \mathbf{u}_0', \mathbf{u}^{(j+1/2,j+1)}\right),
\end{aligned} \tag{3.34}$$

where $\mathcal{S}_{\text{ode}}$ is the solution to

$$\frac{d\mathbf{u}}{dt} = \mathcal{A}_1(\mathbf{u}) + \mathbf{u}_0', \tag{3.35}$$

using a time adaptive Adam-Bashforth method and $\mathcal{S}_{\text{pde}}$ represents the solution to

$$\frac{d\mathbf{u}}{dt} = \mathcal{A}_2(\mathbf{u}) - \mathbf{u}_0', \tag{3.36}$$

using a leapfrog staggered Crank-Nicolson time-centering algorithm. Analysis shows that SS-leapfrog+DR method is second-order accurate in time regardless of the choice of $\mathbf{u}_0'$. This allows for $\mathbf{u}_0'$ to be constructed to reduce the ODE/PDE splitting error. Our construction of $\mathbf{u}_0'$ satisfies the following conditions:

- $\mathbf{u}_0'$ should vanish when $d\mathbf{u}_{\rm pde}/dt$ and $d\mathbf{u}_{\rm ode}/dt$ are additive, i.e., have same sign (this condition is expected to be rare and likely to only apply for fast dynamics where the operators are dominantly linear),

- $\mathbf{u}_0'$ should be limited to the lesser of $d\mathbf{u}_{\rm pde}/dt$ and $-d\mathbf{u}_{\rm ode}/dt$ (when one operator dominates, the implicit fluid solves or multistep ODE method associated with the dominant operator should determine the bulk of the change in $\mathbf{u}$).

To satisfy these constraints we construct $\mathbf{u}_0'$ with a `minmax` function defined as

$$\mathbf{u}_0' = -\min\left(\max\left(-\frac{|\mathcal{A}_2\mathbf{u}^{(j+1/2,j)}|}{|\mathcal{A}_1\mathbf{u}^{(j+1/2,j)}|},0\right),1\right)\mathcal{A}_1\mathbf{u}^n. \tag{3.37}$$

The implementation of this form is approximate and is used for computational efficiency. With a C_0 finite-element discretization, calculation of the second-order derivatives associated with the PDE equations, $\mathcal{A}_2\mathbf{u}$, requires integration by parts and an additional mass-matrix solve. In order to avoid the cost associated with this solve, we use an approximation from the prior time-step solve

$$\mathcal{A}_2\mathbf{u}^{(j+1/2,j)} \simeq \frac{\mathbf{u}^{(j,j)}-\mathbf{u}^{(j,j-1)}}{\Delta t}+\mathbf{u}_0'. \tag{3.38}$$

Figure 3.4 shows a schematic of the Strang-split time advance within the leapfrog with Douglas-Rachford inspired coupling. All the fields are solved simultaneously in the ODE steps while we still have the field staggering for the PDE solver. It is important to note that we update $\mathbf{u}_0'$ for different fields at different spots in the iteration scheme to properly center the operator splitting with respect to the different fields in the leapfrog. The leapfrog advance for fields is staggered limiting the second superscript in Eq. (3.34) to velocity advance only. For full description of the superscripts for fields consult Fig. 3.4.

3.3.5 Discussion of the sources of the error

The prior discussion identifies multiple sources of error for the different time-discretization algorithms. These are summarized as

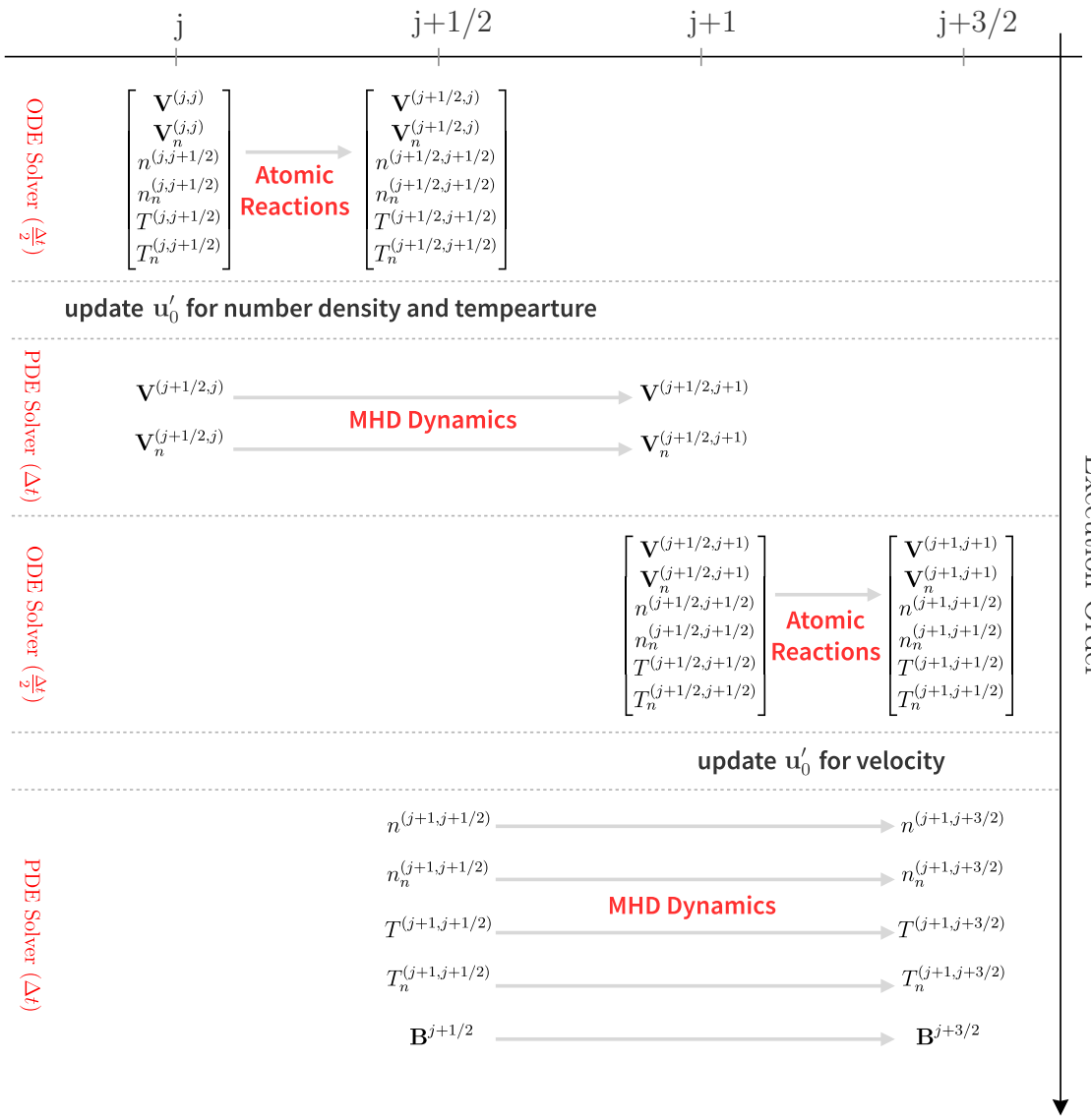

Figure 3.4: Schematic of SS-leapfrog+DR time advance. Strang-split is interleaved into the leapfrog integrating all the fields simultaneously, while the fields are staggered in the leapfrog algorithm and are solved independently.

- **Nonlinear error**

  Neglecting nonlinear terms in plasma-neutral interactions introduces a source of error that is substantial in specific parameter regimes. We eliminate this error by adding a Jacobian-free Newton-Krylov iteration to the Crank-Nicolson method or alternatively using an adaptive time-step size ODE solver in the Strang-split method.

- **Crank-Nicolson time-centering error**

  Time centering the atomic physics in the Crank-Nicolson method results in a second order in time-step size error. Using an adaptive Adam-Bashforth ODE solver in the Strang-split method eliminates this error.

- ***T-in-n* error**

  As discussed in Sec. 3.3.1 including the atomic interactions between plasma and neutrals breaks the data dependency of the MHD equations that is exploited by the leapfrog algorithm. Solving number density and temperature equations independently leads to an error from temperature-dependent cross-section terms in the density equation. This error is eliminated by interleaving a Strang-split solve for the full system of equations into the leapfrog algorithm as described in Sec. 3.3.4.

- **Field staggering error**

  Atomic reaction terms in center of mass velocity and temperature equations, Eqs. (2.50) – (2.53), depend on relative velocity between the species and staggering the velocity in the leapfrog algorithm introduces a source of error in plasma and neutral temperature solutions. Similar to *T-in-n* error, solving the full system of equations in the Strang-split algorithm as discussed in Sec. 3.3.4 eliminates this error.

- **ODE/PDE splitting error**

  As discussed in Sec. 3.3.3 the Strang-split method divides the equations into constituent ODE and PDE parts. When there are large cancellations between the ODE

and PDE terms the Strang-split method is prone to significant error with oscillation in the solution between the different steps of each solve. These oscillations can lead to incorrect steady states. Douglas-Rachford inspired Strang-split with proper choice of $\mathbf{u}_0'$ is designed to reduce this oscillations by limiting the changes during the ODE or PDE advance.

3.4 Boundary conditions

Implementing boundary conditions is a vital step in numerical solutions where we constrain the governing equations in time and space. For instance, we consider a linear differential equation in a domain Ω given by

$$\mathcal{L}(u) = 0, \tag{3.39}$$

subject to a particular initial and boundary conditions. As stated in this chapter, we approximate the exact solution $u(x,t)$ with a truncated series of the form

$$u^{\delta}(x,t) = u_0(x,t) + \sum_{i=1}^{N_{dof}} \hat{u}_i(t)\varphi_i(x), \tag{3.40}$$

where u^{δ} is the approximate solution, $\varphi_i(x)$ are trial functions, $\hat{u}_i(t)$ are the N_{dof} unknown coefficients, and $u_0(x,t)$ is selected in such a way to satisfy the initial and boundary conditions [13]. There are two types of boundary conditions acting on governing equations; *Dirichlet* or *essential* boundary condition which specifies a condition on the solution at a specific point, and *Neumann* or *natural* boundary condition which states a condition on the derivative of the solution. We should note that since the known function $u_0(x,t)$ satisfies the boundary conditions of the problem, $\varphi_i(x)$ by definition satisfies homogeneous boundary conditions.

3.4.1 Neumann boundary condition

Let us start with Neumann boundary condition which appears *naturally* in finite element weak formulation. The key components causing Neumann boundary condition to be a natural

part of finite element are second order derivatives and weak formulation. As an example, consider the Laplace equation

$$\mathcal{L}(u) \equiv \nabla^2 u = 0, \tag{3.41}$$

subject to the following boundary conditions:

$$u(0) = g_{\mathcal{D}}, \qquad \frac{\partial u}{\partial x}(1) = g_{\mathcal{N}},$$

with $g_{\mathcal{D}}$ and $g_{\mathcal{N}}$ being constants. Multiplying the Laplace equation by test function $\varphi(x)$ and integrating over the domain Ω, we can write the weak formulation as

$$\langle \varphi, \mathcal{L}(u) \rangle = \int_0^1 \varphi \frac{\partial^2 u}{\partial x^2} dx = 0. \tag{3.42}$$

Next step is integrating by part and applying the Gauss' divergence theorem. By definition, test function $\varphi(x)$ is zero on Dirichlet boundaries ($\varphi(0) = 0$) and weak formulation is simplified to

$$\int_0^1 \frac{\partial \varphi}{\partial x} \frac{\partial u}{\partial x} dx = \left[\varphi \frac{\partial u}{\partial t} \right]_0^1 = \varphi(1) g_{\mathcal{N}}. \tag{3.43}$$

We can see how the Neumann boundary condition appears naturally in finite element representation and for special case of zero slope, the last term simply vanishes. A consequence of integration by parts in weak form is the surface integral term which appears when we have a first order spatial derivative. These terms are usually zero, unless we have special cases like surface electric fields or outside pressure in open boundaries. In these situations we use predefiened or known values from previous time-step to calculate the surface integral. We will discuss this further later in this chapter.

3.4.2 Dirichlet boundary condition

There are two different ways of implementing a Dirichlet boundary condition. The most general way of enforcing Dirichlet boundary conditions is *lifting* a known solution which is equivalent to decomposing the approximate solution u^{δ} into a known lifted part $u^{\mathcal{D}}$, which satisfies the Dirichlet boundary conditions, and an unknown homogeneous part $u^{\mathcal{H}}$, which is zero on the Dirichlet boundaries [13].

Since the method of *lifting* is unnecessarily complicated, there is an alternative approach to impose Dirichlet boundary conditions. In this approach which is used in here as well, a matrix system including all degrees of freedom for both the test and trial functions is assembled. Then, the rows corresponding to the known degrees of freedom are set to zero except for the diagonal element, and the known Dirichlet boundary value is set to the right-hand side. This approach results in an asymmetric matrix which is harder to solve, however, is less complicated than the lifting method.

3.4.3 Magnetic flux injection

Injecting magnetic flux from a boundary into the simulation domain is a required boundary condition for plasma acceleration test case. A Dirichlet boundary condition and a thin diffusive layer are used to maintain the inflow of magnetic flux from the boundary. Here, we apply the nonzero Dirichlet condition on toroidal component of the magnetic field, while restricting the other two components to zero.

3.4.4 Particle flux

Similar to magnetic flux injection, we can maintain a source of particles at the boundary using a thin diffusive layer and a Dirichlet boundary condition on number density. Diffusivity makes sure that we have particle flow while the Dirichlet boundary condition maintains the value at the boundary.

3.4.5 Open boundary

Imposing inflow or outflow boundaries requires Neumann boundary condition on velocity equation. As explained before, we get natural boundary conditions in finite element weak formulation if we have a second order derivative in the equation. Viscous diffusion can enforce the Neumann boundary condition in the velocity equation if it is the dominant term at the boundaries. We will ensure of this dominance by using a modified diffusivity shape function

to enhance the diffusion effects close to the boundary.

Chapter 4

VALIDATION CASES

Now that the interactive plasma-neutral model is described and the numerical framework has been introduced, we are ready to study wave motions in partially ionized plasmas and validating the numerical tool. It is convenient to study systems of linear differential equations using Fourier analysis [7]. In these systems, oscillation in one quantity transfers to other quantities matching the same frequency with different amplitudes and phases. The MHD plasma equations are not a set of linear differential equations, however, we assume small perturbations and correspondingly linearize the nonlinear system.

The linearization and Fourier analysis of nonlinear two-component model for partially ionized plasmas is used to validate the numerical implementation of the model.

4.1 Ionization equilibrium

Charged particles in a plasma can have two type of collisions: collisions with other charged particles and collisions with neutral atoms and molecules [7]. Whether collisions with charged particles are dominant or collisions with neutral particles, depends on the degree of ionization which consequently depends on the atomic processes between particles. 'Partially ionized plasma' or 'weakly ionized gas' is a state where the degree of ionization is so low that collisions with neutrals are dominant.

In order to determine the relative importance of collisions of charged particles with other charged or neutral particles, we need to estimate the degree of ionization. There are two types of ionization processes (see Figure 4.1), namely electron impact ionization where an electron collides with a neutral atom and rips out the bound electron, leaving an ion and two electrons, and photo ionization where a photon is absorbed by a neutral atom, dissociating

(a) Electron Impact Ionization

(b) Photo Ionization

Figure 4.1: Ionization processes. In highly collisional plasmas where electron mean-free-path is short the main cause of ionization is electron impact ionization shown in (a), where a high energy electron hits a neutral atom and kicks the last electron out of its orbit. On the other hand, if plasma is opaque and radiation is well trapped a neutral atom absorbs a photon and the excited electron leaves its orbit leaving a positively charged ion (b).

it into an ion and an electron. These processes can happen in the reverse direction making recombination processes (Figure 4.2). In three-body recombination, two electrons and an ion recombine to make a neutral atom and a free electron, where in radiative recombination, an electron binds to an ion, releasing energy in the form of a photon [7].

Ionization and recombination processes compete with each other to create a steady state with a certain degree of ionization which can be calculated using statistical mechanics. Whether a type of process in both ionization and recombination is dominant or not depends on the plasma density. For the case of dense plasmas, one can have 'local thermodynamic equilibrium' or LTE, where electron impact ionization and three body recombination are the dominant atomic processes between plasma and neutrals. On the other hand, at lower densities a different steady-state arises called 'coronal equilibrium' where electron impact ionization balances the radiative recombination like the solar corona.

The Saha equation obtained from a statistical description of plasma gives the degree of ionization as a function of electron number density and temperature for a weakly ionized gas in thermal equilibrium (at least locally). As mentioned before, in local thermodynamic equilibrium case, collisional ionization competes with three body recombination to set the steady state and degree of ionization can be written as

(a) Three Body Recombination

(b) Radiative Recombination

Figure 4.2: Recombination processes. Three body recombination (a) is the reverse process for electron impact ionization where two electrons hit a positively charged ion. One of the electrons gets bound and the other electron absorbs the extra energy. On the other side, an electron gets absorbed by a positively charged ion and the excess energy is released as a photon (b).

$$\frac{n_i}{n_n} = \frac{1}{n_e}\left(\frac{2\pi m_e k T_e}{h^2}\right)^{3/2} e^{-U_i/kT_e}, \tag{4.1}$$

where U_i is the ionization energy of the gas, k is the Boltzmann constant, and h is the Planck constant. Figure 4.3 shows the degree of ionization against electron temperature for different electron number densities.

In coronal equilibrium, the source of electrons by collisional ionization is balanced against the sink of electrons by radiative recombination [7]. As described in number density equation, the electron source rate is given by:

$$S_e = \langle \sigma_{ion} v_e \rangle n_e n_n, \tag{4.2}$$

and the electron sink rate is written as:

$$S_n = \langle \sigma_{rec} v_e \rangle n_e n_i. \tag{4.3}$$

As presented in previous chapters, there are different formulations for average ionization and recombination rates. Figure 4.4a shows that the degree of ionization changes very slightly for different models. Proposed formulations for ionization and recombination rates in coronal equilibrium does not include any density dependence. On the other hand, tables

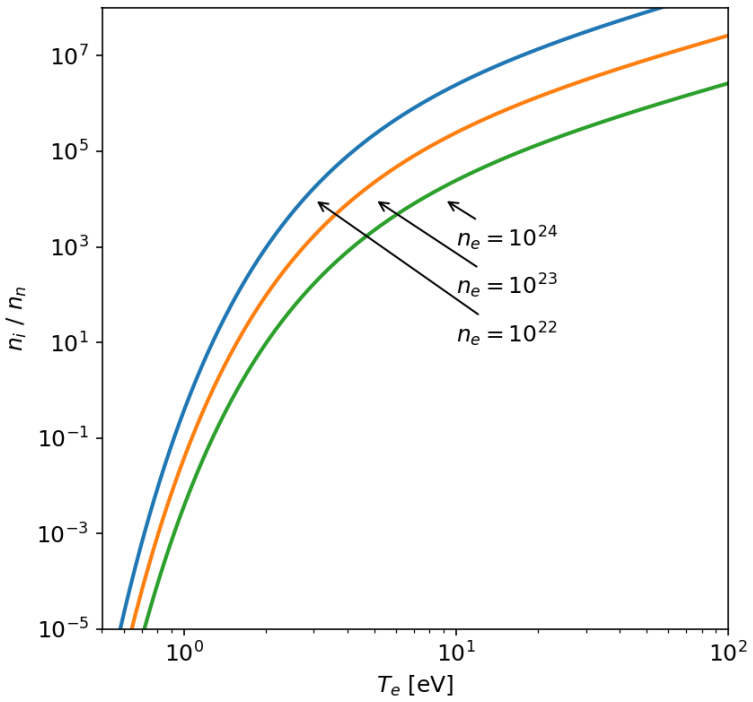

Figure 4.3: Degree of ionization for hydrogen plasma in local thermal equilibrium calculated by the Saha equation. The accuracy of the Saha equation decreases at low densities where three body recombination is no longer dominant.

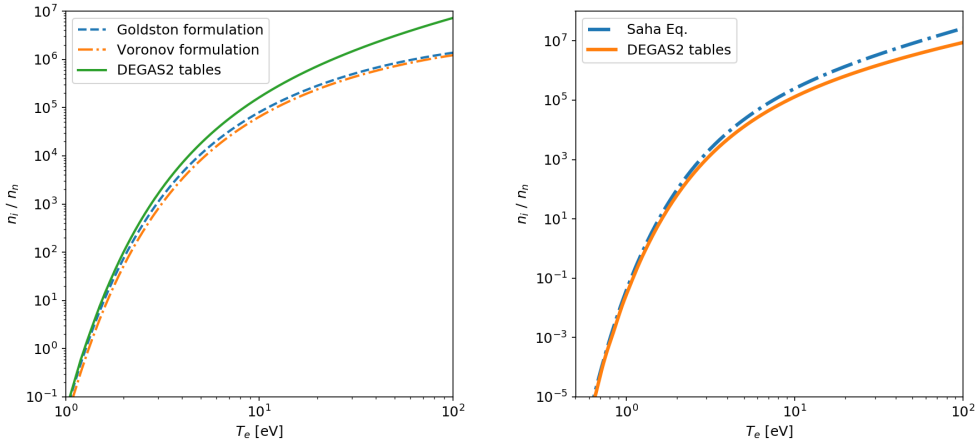

(a) Coronal Equilibrium (b) Local Thermal Equilibrium

Figure 4.4: Degree of ionization for hydrogen plasma at different regimes is compared for different models. DEGAS2 data match the analytic formulae given by Goldston [7] and Voronov [41] at low density, $n = 10^{20}$ $[m^{-3}]$, shown in (a) and Saha equation at high density, $n = 10^{23}$ $[m^{-3}]$, shown in (b).

such as DEGAS2 [37] provide more detailed rates as a function of electron temperature and density. Therefore, they can cover both coronal and LTE regimes with good accuracy. Figure 4.4 compares ionization equilibrium given by formulas with tabulated data (DEGAS2) in different regimes. Although they are not exactly matched, they show a good consistency.

4.2 Steady state number density

As described in Chapter 2, the atomic reactions considered in the plasma-neutral model are electron impact ionization and radiative recombination and as we discussed previously, balance between these two processes results in coronal equilibrium state. Steady state coronal equilibrium is studied to validate the time evolution of plasma and neutral densities in the implementation. Spatially uniform plasma and neutral gas interact in a doubly periodic do-

main to reach the steady state. Both plasma and neutral gas are stationary and temperatures are kept constant in the simulation. In the following the analytic solution and simulation results are presented.

4.2.1 Analytic solution

Evolution of number densities for plasma and neutral species is given as

$$\begin{aligned} \frac{\partial n}{\partial t} + \nabla \cdot (n\mathbf{v}) &= \langle \sigma_{ion} v_e \rangle n n_n - \langle \sigma_{rec} v_e \rangle n^2, \\ \frac{\partial n_n}{\partial t} + \nabla \cdot (n_n \mathbf{v}_n) &= \langle \sigma_{rec} v_e \rangle n^2 - \langle \sigma_{ion} v_e \rangle n n_n. \end{aligned} \tag{4.4}$$

We examine a homogeneous stationary ideal plasma-neutral system with no magnetic field and constant temperature. If the perturbations are sufficiently small, their dynamics can be described by linearized equations given as

$$\begin{aligned} \frac{\partial n'}{\partial t} &= \langle \sigma_{ion} v_e \rangle (n' n_n + n n_n') - \langle \sigma_{rec} v_e \rangle (2 n n'), \\ \frac{\partial n_n'}{\partial t} &= \langle \sigma_{rec} v_e \rangle (2 n n') - \langle \sigma_{ion} v_e \rangle (n' n_n + n n_n'). \end{aligned} \tag{4.5}$$

We can treat the perturbations as waves and represent the number densities as follows

$$\mathbf{q}'(\mathbf{r}, t) = q' \exp{(i\mathbf{k} \cdot \mathbf{r} - i\omega t)}, \tag{4.6}$$

where q' is the complex amplitude, $\mathbf{k}$ is the wave number, and ω is the wave frequency. Since the waves are independent of the spatial coordinates, $\mathbf{k}$ is equal to 0. Substituting perturbations with Fourier representation and solving for ω gives us

$$-\omega^2 + i\omega[\langle \sigma_{ion} v_e \rangle (n_n - n) - 2\langle \sigma_{rec} v_e \rangle n] = 0, \tag{4.7}$$

$$\omega = i[\langle \sigma_{ion} v_e \rangle (n_n - n) - 2\langle \sigma_{rec} v_e \rangle n]. \tag{4.8}$$

This ω is the characteristic decay time of plasma-neutral system where number densities are not in equilibrium.

	$n\ [m^{-3}]$	$T\ [eV]$	$V\ [m/s]$
plasma	1.0×10^{20}	1.3162	0.0
neutral	1.0166×10^{20}	1.3162	0.0

Table 4.1: Equilibrium state for coronal equilibrium test case.

4.2.2 Numerical results

Table 4.1 shows the initial equilibrium state for both plasma and neutral species. Perturbing the system slightly ($\sim 1\%$) out of equilibrium results in an exponential decay of perturbation and the plasma-neutral system recovers its equilibrium state.

At this temperature, average ionization and recombination cross sections can be calculated using formulations given in Chapter 2 as

$$\langle \sigma_{ion} v_e \rangle = 2.2292 \times 10^{-19}\ [m^3/s]$$
$$\langle \sigma_{rec} v_e \rangle = 2.2662 \times 10^{-19}\ [m^3/s].$$

Based on the analytic solution in the previous section, the decay rate is:

$$\omega = -44.95i\ [sec^{-1}],$$

which means it takes ~ 0.089 seconds to decay 98% of the perturbation. Figure 4.5 shows the analytic and numerical results for number density evolution of both plasma and neutral species. Since the number density equation is nonlinear in terms of ionization and recombination, the number densities relaxation is different from perturbation analysis when the perturbation amplitude is large.

4.3 Waves in the two-component model

The governing equations for the nonlinear two-component model is given in Chapter 2. The Fourier analysis of the system starts with linearizing these equations around an equilibrium

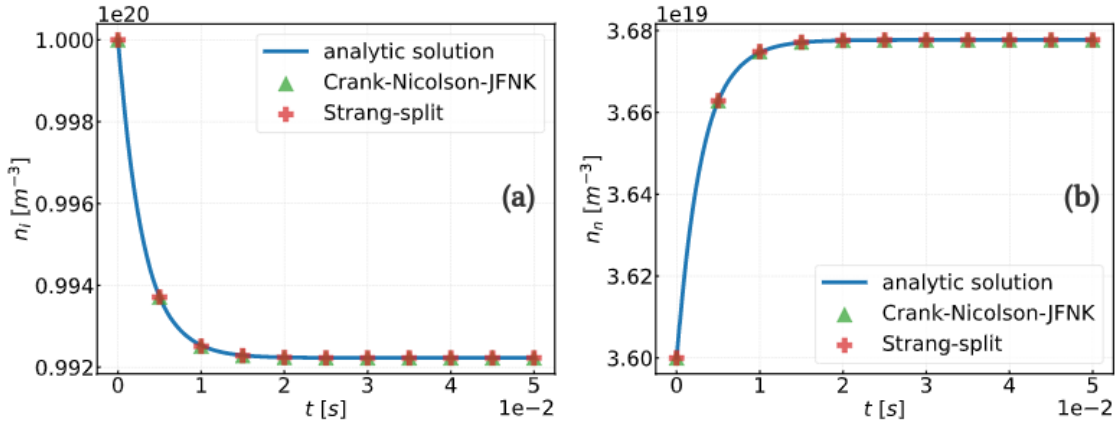

Figure 4.5: A mixture of stationary plasma and neutral hydrogen at a specific temperature evolves toward the coronal equilibrium exponentially. Figure (a) and (b) show the analytic solution (solid lines) and the numerical simulation in NIMROD (asterisks) for plasma and neutral species respectively.

state. The steady state is a spatially uniform, isentropic, magnetized plasma at rest, and linearizing the system of equations gives

$$
\begin{aligned}
\frac{\partial n'}{\partial t} + n\nabla\cdot\mathbf{v}' - S^{ion}(n'n_n + nn'_n) + S^{rec}(2nn') &= 0,\\
\frac{\partial n'_n}{\partial t} + n_n\nabla\cdot\mathbf{v}'_n + S^{ion}(n'n_n + nn'_n) - S^{rec}(2nn') &= 0,\\
mn\frac{\partial \mathbf{v}'}{\partial t} + \nabla p' - \frac{(\nabla\times\mathbf{B}')\times\mathbf{B}}{\mu_0} + S^{ion}mnn_n(\mathbf{v}' - \mathbf{v}'_n) + S^{cx}mnn_n(\mathbf{v}' - \mathbf{v}'_n) &= 0,\\
mn_n\frac{\partial \mathbf{v}'_n}{\partial t} + \nabla p'_n + S^{rec}mn^2(\mathbf{v}'_n - \mathbf{v}') + S^{cx}mnn_n(\mathbf{v}'_n - \mathbf{v}') &= 0,\\
n\frac{\partial p'}{\partial t} - \gamma p\frac{\partial n'}{\partial t} &= 0,\\
n_n\frac{\partial p'_n}{\partial t} - \gamma p_n\frac{\partial n'_n}{\partial t} &= 0,\\
\frac{\partial \mathbf{B}'}{\partial t} - \nabla\times(\mathbf{v}'\times\mathbf{B}) &= 0.
\end{aligned}
\tag{4.9}
$$

where

$$S^{ion} = \langle \sigma_{ion} v_e \rangle,$$
$$S^{rec} = \langle \sigma_{rec} v_e \rangle,$$

$$\begin{aligned} S^{cx} = \sigma_{cx} & \sqrt{\frac{4}{\pi} v_{Ti}^2 + \frac{4}{\pi} v_{Tn}^2 + v_{in}^2} \\ & + \sigma_{cx} v_{Tn}^2 \left[4 \left(\frac{4}{\pi} v_{Ti}^2 + v_{in}^2 \right) + \frac{9\pi}{4} v_{Tn}^2 \right]^{-1/2} \\ & + \sigma_{cx} v_{Ti}^2 \left[4 \left(\frac{4}{\pi} v_{Tn}^2 + v_{in}^2 \right) + \frac{9\pi}{4} v_{Ti}^2 \right]^{-1/2}. \end{aligned}$$

For simplicity, we have neglected viscosity, magnetic diffusion, and Hall term. Also, we assume the adiabatic equation of state is independent of density changes due to ionization and recombination. Now, let the perturbed variables have a linearized form as

$$\mathbf{q}'(\mathbf{r}, t) = q' \exp\left(i\mathbf{k} \cdot \mathbf{r} - i\omega t\right). \tag{4.10}$$

Using this form in the linearized equations gives

$$\begin{aligned} -i\omega n' + in\mathbf{k} \cdot \mathbf{v}' - S^{ion}(n' n_n + n n_n') + S^{rec}(2nn') &= 0, \\ -i\omega n_n' + in_n \mathbf{k} \cdot \mathbf{v}_n' + S^{ion}(n' n_n + n n_n') - S^{rec}(2nn') &= 0, \\ -i\omega mn\mathbf{v}' + i\mathbf{k}p' - \frac{(i\mathbf{k} \times \mathbf{B}') \times \mathbf{B}}{\mu_0} + S^{ion} mnn_n(\mathbf{v}' - \mathbf{v}_n') + S^{cx} mnn_n(\mathbf{v}' - \mathbf{v}_n') &= 0, \\ -i\omega mn_n \mathbf{v}_n' + i\mathbf{k}p_n' + S^{rec} mn^2(\mathbf{v}_n' - \mathbf{v}') + S^{cx} mnn_n(\mathbf{v}_n' - \mathbf{v}') &= 0, \\ -i\omega p' + i\gamma p \mathbf{k} \cdot \mathbf{v}' &= 0, \\ -i\omega p_n' + i\gamma p_n \mathbf{k} \cdot \mathbf{v}_n' &= 0, \\ -i\omega \mathbf{B}' - i\mathbf{k} \times (\mathbf{v}' \times \mathbf{B}) &= 0. \end{aligned} \tag{4.11}$$

These equations describe MHD waves in a homogeneous partially ionized plasma under influence of plasma-neutral interactions. Assuming that $\omega \neq 0$, the number density, pressure,

and magnetic induction equations can be written as

$$\begin{aligned}
n' &= n\frac{\mathbf{k}\cdot\mathbf{v}'}{\omega} - \frac{i}{\omega}S^{ion}(n'n_n + nn'_n) + \frac{i}{\omega}S^{rec}(2nn'),\\
n'_n &= n_n\frac{\mathbf{k}\cdot\mathbf{v}'_n}{\omega} + \frac{i}{\omega}S^{ion}(n'n_n + nn'_n) - \frac{i}{\omega}S^{rec}(2nn'),\\
p' &= \gamma p\frac{\mathbf{k}\cdot\mathbf{v}'}{\omega},\\
p'_n &= \gamma p_n\frac{\mathbf{k}\cdot\mathbf{v}'_n}{\omega},\\
\mathbf{B}' &= \frac{(\mathbf{k}\cdot\mathbf{v}')\mathbf{B} - (\mathbf{k}\cdot\mathbf{B})\mathbf{v}'}{\omega}.
\end{aligned} \tag{4.12}$$

Substituting these expressions into equations of motion for plasma and neutral species gives

$$\begin{aligned}
\left[\omega^2 - \frac{(\mathbf{k}\cdot\mathbf{B})^2}{\mu_0 mn}\right]\mathbf{v}' - \left[\frac{\gamma p}{mn}\mathbf{k} + \frac{B^2}{\mu_0 mn}\mathbf{k} - \frac{\mathbf{B}}{\mu_0 mn}(\mathbf{k}\cdot\mathbf{B})\right](\mathbf{k}\cdot\mathbf{v}') + \frac{\mathbf{k}}{\mu_0 mn}(\mathbf{k}\cdot\mathbf{B})(\mathbf{v}'\cdot\mathbf{B})\\
+ i\omega S^{ion}n_n(\mathbf{v}' - \mathbf{v}'_n) + i\omega S^{cx}n_n(\mathbf{v}' - \mathbf{v}'_n) = 0,\\
\omega^2\mathbf{v}'_n - \frac{\gamma p_n}{mn_n}\mathbf{k}(\mathbf{k}\cdot\mathbf{v}'_n) + i\omega S^{rec}\frac{n^2}{n_n}(\mathbf{v}'_n - \mathbf{v}') + i\omega S^{cx}n(\mathbf{v}'_n - \mathbf{v}') = 0.
\end{aligned}$$

We study both Alfvén and magneto-acoustic waves, where Alfvén waves are incompressible transverse waves propagating parallel to background magnetic field and magneto-acoustic waves are compressible longitudinal waves traveling perpendicular to magnetic field lines.

4.3.1 Incompressible waves

The first class of low-frequency waves is the incompressible transverse waves ($\mathbf{v}' \perp \mathbf{B}$) propagating purely parallel to background magnetic field ($\mathbf{k} \parallel \mathbf{B}$) as shown in Figure 4.6.

If we assume that number density is independent of ionization and recombination, incompressible flow gives $\mathbf{k}\cdot\mathbf{v}' = 0$, Therefore, the equations of motion simplify to give

$$\begin{aligned}
\omega^2\mathbf{v}' + \frac{k^2B^2}{\mu_0 mn}\mathbf{v}' + i\omega S^{ion}n_n(\mathbf{v}' - \mathbf{v}'_n) + i\omega S^{cx}n_n(\mathbf{v}' - \mathbf{v}'_n) = 0,\\
\omega^2\mathbf{v}'_n + i\omega S^{rec}\frac{n^2}{n_n}(\mathbf{v}'_n - \mathbf{v}') + i\omega S^{cx}n(\mathbf{v}'_n - \mathbf{v}') = 0.
\end{aligned} \tag{4.13}$$

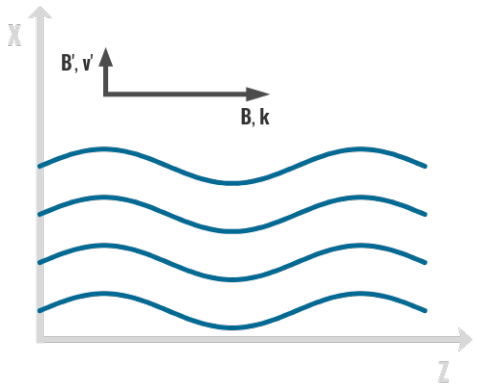

Figure 4.6: The shear Alfvén wave is a low-frequency incompressible transverse wave propagating along the external magnetic field. Both magnetic field and velocity perturbations are perpendicular to wave vector **k** as shown.

Solving this system of equations for $\mathbf{v}'$ and $\mathbf{v}'_n$, we can find the dispersion relation for shear Alfvén wave in a partially ionized plasma considering the ionization, recombination, and resonant charge exchange as

$$\omega^3 + i\omega^2 \left(S^{ion} n_n + S^{rec} \frac{n^2}{n_n} + S^{cx} n + S^{cx} n_n \right) - \omega k^2 v_A^2 - i \left(S^{rec} \frac{n^2}{n_n} + S^{cx} n \right) k^2 v_A^2 = 0, \quad (4.14)$$

where v_A is the propagation velocity called the Alfvén velocity defined as

$$v_A = \frac{B}{\sqrt{\mu_0 m n}}. \quad (4.15)$$

The shear Alfvén wave is analogous to a wave in a plucked string with tension B^2/μ_0 and density of mn. Where plasma flow across the magnetic field can increase the bending of the field; the shear wave acts to reduce the additional curvature of the field line and reduce the tension. We expect that atomic reactions between plasma and neutral species act as a drag force causing the damping of the wave mode and also decreasing the frequency of the wave.

	$n\ [m^{-3}]$	$T\ [eV]$	$V\ [m/s]$	$B\ [T]$
plasma	1.0×10^{20}	12.417	0.0	1.0
neutral	1.0×10^{20}	12.417	0.0	

Table 4.2: Equilibrium state for shear Alfvén wave test case.

Numerical results

Table 4.2 shows the equilibrium state used for numerical simulation of a shear Alfvén wave. The Alfvén velocity is

$$v_A = \frac{B}{\sqrt{\mu_0 m n}} = 1542.7\ [km/s].$$

Figure 4.7a shows the analytic solution and the numerical results for 2 oscillation periods where interaction with neutrals are excluded.

Adding atomic reactions to the system, reduces the frequency and damps the wave mode as expected. Here, we use DEGAS2 tables for ionization and recombination cross-sections. The wave frequency is reduced by 6.64% compared to plasma-only case. Figure 4.7b shows a good match between the analytic solution and numerical results.

4.3.2 Compressible waves

The second class of low-frequency waves in the compressible longitudinal waves ($\mathbf{B}' \parallel \mathbf{B}$) propagating across the magnetic field direction ($\mathbf{k} \perp \mathbf{B}$) and involves compression of the magnetic field [25] as shown in Figure 4.8.

Since we assumed the fluid is compressible, there are density perturbations in the wave and magnetic field perturbations are parallel to the background field [4]. Magneto-acoustic waves act to reduce thermal or magnetic pressure gradients and they are present even in cold plasmas where the sound speed is zero. Revisiting the equations of motion and considering

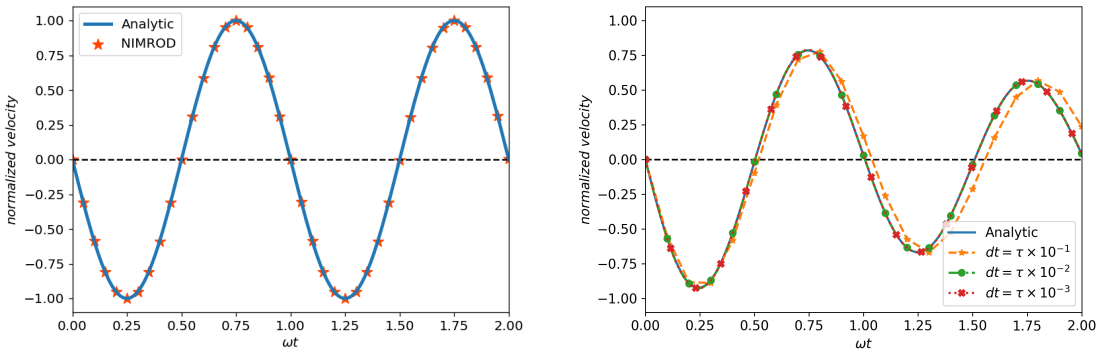

(a) plasma-only (b) plasma-neutral

Figure 4.7: Shear Alfvén wave is a wave with frequency of kv_A in plasma (a). Plasma-neutral interactions act as a diffusion process, lowering the frequency and damping the wave amplitude (b). Solid lines show the analytic solution for shear Alfvén wave with and without neutral species involved where the markers show numerical simulation results in NIMROD. Figure (b) shows the numerical results for different time-steps where large time-step results in a higher damping effect which is not physical.

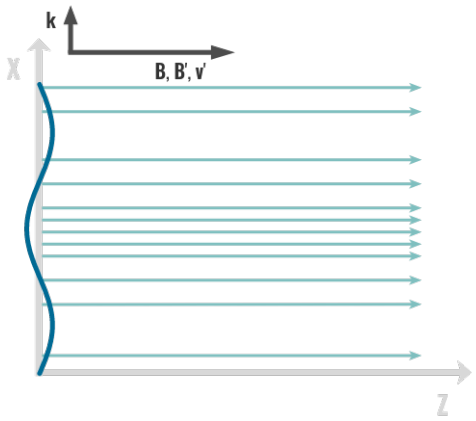

Figure 4.8: Magneto-acoustic wave is a low-frequency compressible longitudinal wave propagating across the external magnetic field. Both magnetic field and velocity perturbations are perpendicular to wave vector **k** and along the external magnetic field **B** as shown.

perturbations parallel to background magnetic field, we get

$$\begin{aligned}\omega^2\mathbf{v}' + (k^2c_s^2 + k^2v_A^2)\mathbf{v}' + i\omega S^{ion}n_n(\mathbf{v}' - \mathbf{v}'_n) + i\omega S^{cx}n_n(\mathbf{v}' - \mathbf{v}'_n) = 0,\\ \omega^2\mathbf{v}'_n + k^2c_{s,n}^2 + i\omega S^{rec}\frac{n^2}{n_n}(\mathbf{v}'_n - \mathbf{v}') + i\omega S^{cx}n(\mathbf{v}'_n - \mathbf{v}') = 0,\end{aligned} \tag{4.16}$$

where plasma and neutral sound speeds are defined as

$$\begin{aligned}c_s &= \sqrt{\frac{\gamma p}{mn}},\\ c_{s,n} &= \sqrt{\frac{\gamma p_n}{mn_n}}.\end{aligned} \tag{4.17}$$

Solving the above system of equations for $\mathbf{v}$ and $\mathbf{v}'$ yields the dispersion relation for magneto-acoustic waves in a plasma-neutral system as

$$\begin{aligned}&\omega^4 + i\omega^3\left(S^{ion}n_n + S^{rec}\frac{n^2}{n_n} + S^{cx}n + S^{cx}n_n\right) - \omega^2k^2(v_A^2 + c_s^2 + c_{s,n}^2)\\ &\quad - i\omega k^2\left[(v_A^2 + c_s^2)\left(S^{rec}\frac{n^2}{n_n} + S^{cx}n\right) + c_{s,n}^2(S^{ion}n_n + S^{cx}n_n)\right] + k^4(v_A^2 + c_s^2)c_{s,n}^2 = 0.\end{aligned}$$

The magneto-acoustic wave is simply a longitudinal sound wave where the pressure is augmented by the magnetic pressure [39]. Similar to shear Alfvén waves, plasma-neutral interactions act as a drag force on magneto-acoustic waves causing them to slow down and also decay with time. In the remaining of this section, we compare analytic solution and numerical results for our implementation.

Numerical results

Table 4.3 shows the equilibrium state for numerical simulation. We assume small thermal pressure compared to magnetic pressure ($\sim 2\%$) for plasma and set the neutral thermal pressure equal to plasma thermal pressure in this simulation.

Accordingly, the Alfvén velocity can be calculated as

$$v_A = \frac{B}{\sqrt{\mu_0 mn}} = 1542.7\ [km/s],$$

	$n\ [m^{-3}]$	$T\ [eV]$	$V\ [m/s]$	$B\ [T]$	β
plasma	1.0×10^{20}	12.417	0.0	1.0	1.0×10^{-3}
neutral	1.0×10^{20}	12.417	0.0		

Table 4.3: Equilibrium state for magneto-acoustic wave test case.

and the sound speeds are

$$c_s = c_{s,n} = \sqrt{\frac{\gamma kT}{m}} = 31.5\ [km/s]. \tag{4.18}$$

Figure 4.9a shows the analytic and numerical solutions for magneto-acoustic wave in plasma-only case through 2 oscillation periods. On the other hand, Figure 4.9b shows the results for the case including plasma-neutral interactions. As it was expected, the oscillation frequency reduces ($\sim 3.3\%$ for this case) and the drag force due to atomic processes damps the wave. Simulation results show a good match with analytic solution confirming the numerical implementation.

4.4 Spatially Uniform Benchmarks

Having described several potential time-advance algorithms, we now compare their accuracy and efficiency by running a series of spatially uniform tests of the plasma-neutral interactions in regimes representing typical fusion devices. Not having any spatial gradients reduces the SS-leapfrog+DR method to an adaptive time-step size ODE integrator for all equations in 0-D and the error is simply set by the tolerance to the solver. Thus, we ignore this method in 0-D cases. Spatially nonuniform cases will be considered in Sec. 4.5. In the battery of 0-D tests we have conditions that mimics the tokamak core, tokamak edge, nonlinear ionization and flow relaxation. Here we are purely testing the atomic physics and all spatial dependent terms are zero.

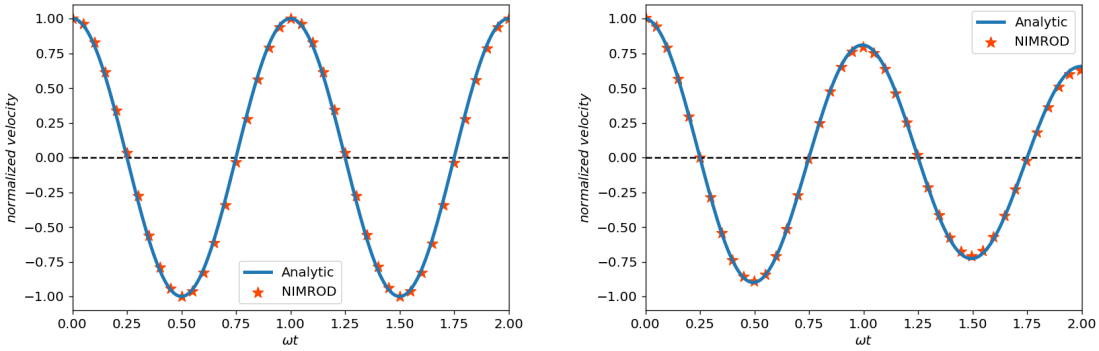

(a) plasma-only

(b) plasma-neutral

Figure 4.9: Magneto-acoustic wave has a frequency of $k(va + cs)$ in plasma (a), while the atomic reactions and collisions with neutrals decreases the frequency and damps the wave amplitude as shown in (b). Solid lines show the analytic solution and asterisks are the numerical simulation results in NIMROD.

Plasma and neutral species interact with each other through three main processes: ionization, recombination, and charge exchange. For a spatially uniform system, number densities depend only on ionization and recombination processes and the equilibrium point is when ionization balances recombination. This equilibration point depends on electron temperature which depends on total energy of the system. We ignore the effective ionization energy, i.e., plasma is optically thick and radiation energy is trapped to keep the total energy conserved. Including the energy loss will cool down the system continuously until it reaches the temperature of zero. In this section, we look at the accuracy and efficiency of the two algorithms in finding the equilibrium point for a plasma-neutral system.

4.4.1 Tokamak Core

Consider a typical tokamak core condition with cold neutral fueling. At very high electron temperatures, the ionization rate is almost constant and recombination rarely happens.

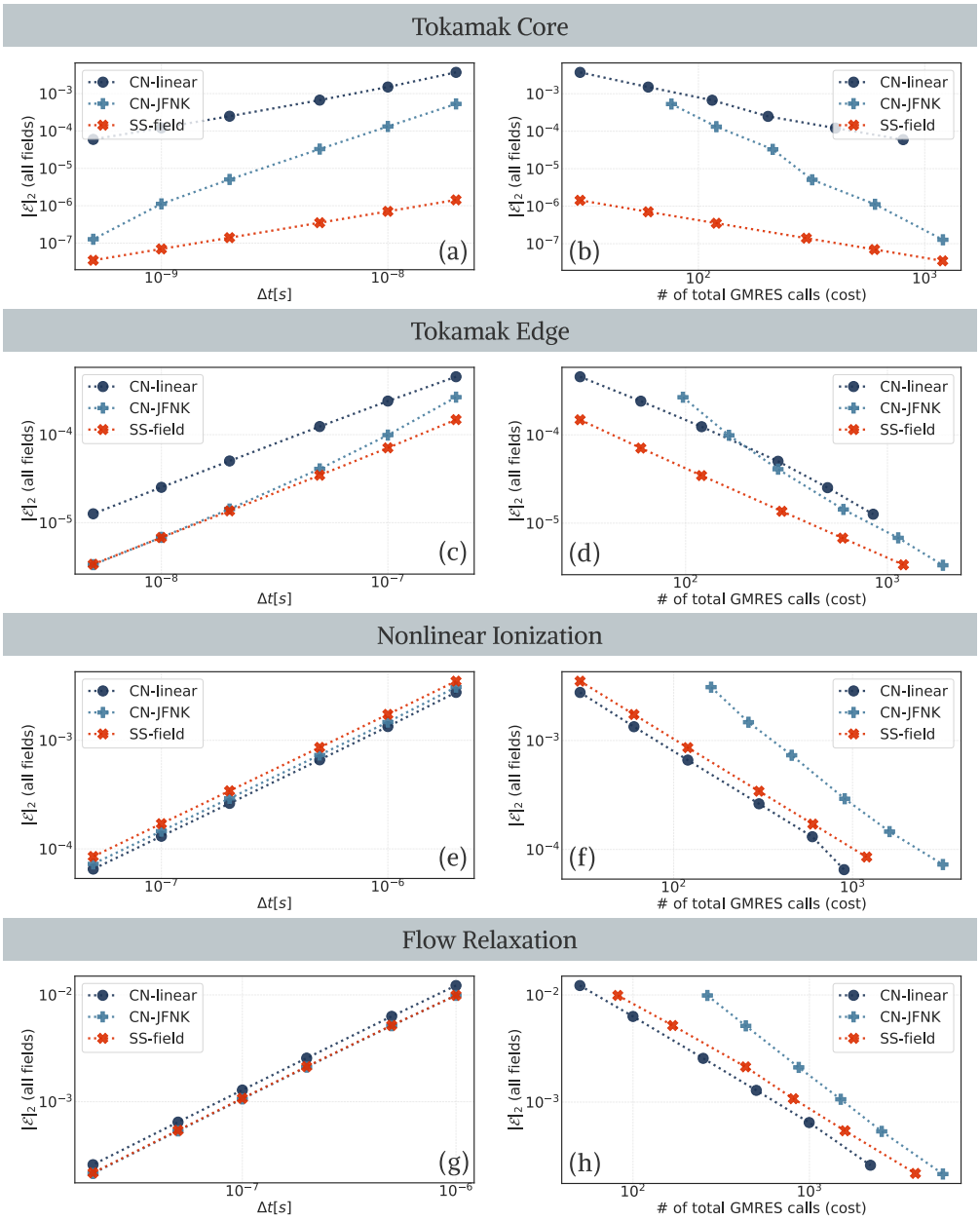

Figure 4.10: Accuracy and computational cost of methods for 0-dimensional test cases. Total l_2 error is summation of l_2 errors for all changing fields and number of GMRES iterations for linear solver is considered a proxy for computational cost. The difference between methods in convergence plots shows the different sources of error.

Thus, nonlinear terms in the number density equations are negligible compared to their linear counterparts in the source terms. High temperature plasma ionizes the neutral atoms and thus the plasma undergoes dilution cooling while the neutrals heat up. Large changes in neutral temperature makes the nonlinear source terms in the temperature equations dominant, and thus requires the full nonlinear solve. The initial state and the change in the plasma and neutral fields are given in Table 4.4. Clear distinction between errors for different algorithms makes this case a good starting point to explain the sources of the errors and how each method handles them.

	Initial		Change (Δ)	
	Number Density $[\mathrm{m}^{-3}]$	Temperature [eV]	Number Density $[\mathrm{m}^{-3}]$	Temperature [eV]
Plasma	10^{20}	1241.7	4.15×10^{15}	0.1
Neutral	10^{16}	1.2417	-4.15×10^{15}	1072.3

Table 4.4: Initial state and change of plasma and neutral species in a typical tokamak core regime. Hot plasma in the core ionizes the neutral atoms while they are heating up to reach thermal equilibrium with the plasma. The final states do not represent the equilibrium point but rather the state at $t = 2 \times 10^{-7}$ [s].

Figure 4.10(a) shows the normalized error with respect to chosen time-step for the CN-linear (blue circle), the CN-JFNK (orange plus), and the SS-field method (green cross). Errors are calculated compared to results for a fine-temporal-resolution computation with $\Delta t = 2 \times 10^{12}$ [s]. The overall normalized error is defined as

$$\|\mathcal{E}\|_2 = \frac{1}{N} \sum_j \sum_i \sqrt{\left(\frac{u_i^j - u_{i,ref}^j}{u_{i,ref}^j} \right)^2}, \tag{4.19}$$

where subscript i represents the components of vector $\mathbf{u}$, composed of evolving fields n, $\mathbf{V}$, and T for both species plus $\mathbf{B}$, superscript j indicates the time slice, and N is the total number of time slices. The entire duration of each run is divided into 10 uniformly spaced time slices.

Comparing errors for different discretization schemes disentangles three different sources of error as identified in Sec. 3.3.5. For instance different errors in Fig. 4.10(a) are indicated as:

- Nonlinear error represented by the difference between CN-linear and CN-JFNK,
- Crank-Nicolson time centering error shown as the difference between CN-JFNK and SS-field,
- *T-in-n* error demonstrated by the difference between SS-field and the tolerance to the solver.

It is important to note that the different errors are not strictly additive and there are cases with fortuitous cancellations.

Solving the linear system using generalized minimal residual method (GMRES) in the semi-implicit leapfrog method is a time-consuming section, and we use the total number of GMRES iterations as a proxy to measure the cost for each method. Figure 4.10(b) shows the normalized error versus total number of linear solve iterations for different time-steps for the CN-linear (blue circle), the CN-JFNK (orange plus), and the SS-field method (green cross). Solving the PDE equations independently in SS-field method reduces the computational cost while removing the *nonlinear* and *Crank-Nicolson time-centering* errors. CN-JFNK method converges faster by reducing the time-step size, but it comes at the cost of more linear matrix solves which increase the run-time.

4.4.2 Tokamak Edge

In the edge region of tokamaks, low plasma temperature in combination with high neutral number density enhances the atomic interactions, thus the numerical algorithm gets more challenged. Ionization rate changes drastically at electron temperatures of around $1 - 5$ [eV] and recombination has a comparable contribution in atomic processes. Heat exchange with cold neutrals cools down the plasma which causes the recombination rate to become more dependent on plasma number density. Since the change in number densities are tiny, nonlinear source terms have a negligible effect in the number-density advance. However, nonlinear source terms in the temperature equations have tangible contribution to error because of the large changes in the plasma temperature. The initial state and changes in different fields for both species are given in Table 4.5. Here, the final state of computation is not exactly the steady state because we want to focus on a dynamic part of the solution.

	Initial		Change (Δ)	
	Number Density $[\mathrm{m}^{-3}]$	Temperature [eV]	Number Density $[\mathrm{m}^{-3}]$	Temperature [eV]
Plasma	10^{17}	2.4834	1.64×10^{14}	-1.331
Neutral	10^{20}	0.025	-1.64×10^{14}	0.0027

Table 4.5: Initial state and change for plasma and neutral species in a typical tokamak edge regime. The plasma loses energy by ionizing the cold neutrals in the process. The final states do not represent the equilibrium point but rather are the state at $t = 2 \times 10^{-6}$ [s].

Figure 4.10(c) presents the summation of a normalized error for all changing fields versus time-step for different algorithms. The time-step size for reference computation for error calculation is $\Delta t = 2 \times 10^{-11}$ [s]. Since atomic cross-sections are highly nonlinear dropping

the nonlinear terms introduces error regardless of the size of the time-step. At large time-steps *Crank-Nicolson time-centering* error explains the difference between CN-JFNK and SS-field method, however, at smaller time-steps this error becomes negligible. Similar to tokamak core case *T-in-n* error is presented by the difference between SS-field and solver error. Figure 4.10(d) shows the tipping point between CN-linear and CN-JFNK after which we get better accuracy relative to the computational cost by including the nonlinear terms in the solver.

4.4.3 Nonlinear Ionization

The initial state of the tokamak edge test case is close to equilibrium and number-density changes are small, thus the nonlinear source terms in the density equation are negligible despite the fact that the cross-section terms are highly nonlinear at low electron temperatures. In order to stress the algorithms further, a hypothetical regime is considered: nonlinear ionization where the initial state given in Table 4.6 is far from equilibrium and the change during the computations is considerable. The higher ionization rate results in increasing plasma number density and dilution cooling. Heat exchange between the species cools down the neutrals and keeps the total energy of the system constant (the ionization energy loss is ignored here). The final state is not the asymptotic steady state but temperatures are largely equilibrated between species.

Similar to the tokamak core and tokamak edge cases, Fig.4.10(e) shows the normalized error versus time-step for different algorithms. Time-step size for the reference computation is $\Delta t = 2 \times 10^{-10}$ [s]. Interestingly, the CN-linear method performs better than both the CN-JFNK and SS-field solvers. The different sources of error are not additive in this instance and there is partial cancellation of the errors. Diving more into the computation details, the high ionization rate results in large source terms in the density equations. Without nonlinear terms, the plasma number density solution overshoots, the higher plasma density enhances dilution cooling which in turn drops the ionization rate. Finally, the reduced ionization rate limits the source term and the overshoot in subsequent steps which partially cancels the

	Initial		Change (Δ)	
	Number Density [m^{-3}]	Temperature [eV]	Number Density [m^{-3}]	Temperature [eV]
Plasma	10^{20}	2.4834	2.77×10^{19}	-0.2112
Neutral	10^{20}	2.4834	-2.77×10^{19}	-0.2111

Table 4.6: Initial state and change for plasma and neutral species in a highly nonlinear regime. Ionization and recombination cross-sections change significantly with temperature, stressing *T-in-n* error. Final states do not represent the equilibrium point.

initial error. The nonlinear algorithms eliminate the overshoot by including the nonlinear contributions to the source terms. However, the overall error is increased without partial cancellation of the *T-in-n* error. The error cancellation in CN-linear is fortuitous for this specific case.

Figure 4.10(f) shows the total number of GMRES iterations for each algorithm as a measure of computational cost. Error cancellation in the CN-linear method suggests that it is more efficient to ignore nonlinear terms in CN algorithms, however, this is an accidental coincidence. Although the SS-field method is the best of three, leapfrog staggering results in a considerable *T-in-n* error which is eliminated by the Strang-split within the leapfrog.

4.4.4 Flow Relaxation

Up until now all the test cases are focused on number density and temperature equations. The flow relaxation test case examines the atomic reactions within the center-of-mass-velocity equation in conjunction with the atomic processes in the density and temperature. To focus on the velocity equation, plasma and neutral species start from a density equilibrium point where ionization and recombination rates balance and temperatures equilibrated. The

plasma has a uniform velocity and neutrals are stationary.

The high-velocity plasma exchanges momentum and energy with neutral particles through atomic reactions. In the process, the neutrals are ionized, heated, and dragged along with plasma. The plasma and neutral thermal energies increase from frictional heating while plasma undergoes dilution cooling. The charge exchange time scales are much shorter than the ionization and recombination time scales and the number-density change for the species is negligible. Thus, the momentum and thermal equilibration dominates the dynamics reducing the dilution cooling. Table 4.7 presents the initial state and changes in the fields for both species. The normalized error is calculated compared to a reference computation with $\Delta t = 1 \times 10^{-10}$ [s].

	Initial			Change (Δ)		
	Number Density [m^{-3}]	Temperature [eV]	Velocity [m/s]	Number Density [m^{-3}]	Temperature [eV]	Velocity [m/s]
Plasma	10^{19}	1.2417	10^4	1×10^{15}	0.1141	-5447
Neutral	1.492×10^{19}	1.2417	0	-1×10^{15}	0.1239	3651

Table 4.7: Initial state and change for plasma and neutral species in a flow relaxation test case. Plasma flow transfers momentum to neutral species through charge-exchange collisions as well as ionization until equilibrium is reached. The final states do not represent the equilibrium point but rather are the state at $t = 1 \times 10^{-5}$ [s].

Figure 4.10(g) presents the error versus time-step size for all three methods. Among all the error sources, nonlinear contributions have a slight contribution to the total error and the field staggering is the dominant source of error. Since the number density and temperature fields are close to equilibrium through all the run time, *T-in-n* error is negligible. Crank-Nicolson time-centering has no tangible effect in the total error. Similar to previous cases,

Fig. 4.10(h) shows the total error as a function of computational cost.

4.5 Spatially Non-uniform Benchmarks

In this section, we move beyond 0-D cases and analyze the effects of spatially dependent MHD and fluid dynamics in conjunction with atomic reactions.

4.5.1 Ballistic Expansion into Tokamak Pedestal

Fusion-plasma edge fueling is one of the main applications of plasma-neutral MHD models. We investigate the spatially dependent neutral profiles in 1-D with a generic tokamak pedestal test. Plasma profiles are kept stationary throughout the simulation and neutral initial state is set by a local equilibration of ionization and recombination as shown by red lines in Fig. 4.11. To maintain a source of neutral particles during the steady state a thin diffusive layer and Dirichlet boundary conditions are applied to the number-density equation at the wall. The neutral pressure gradient causes ballistic expansion of particles into the core that is balanced by ionization. At the time-asymptotic steady state, shown with blue lines in Fig. 4.11, the plasma is ionized in the edge pedestal before reaching the core. We analyze both the steady-state and dynamic solutions with the different time-advance algorithms.

Steady State Solution

Figures 4.12(a-c) show the steady state profiles for three time-advance algorithms using different time-step sizes. Time-centering the atomic processes with Crank-Nicolson algorithm converges rapidly as seen in Fig. 4.12(a). However, the ODE/PDE splitting error has a significant role in the SS-field solution and the numerical steady state will be dependent on the time step [18]. SS-leapfrog+DR removes the ODE/PDE splitting error through the coupling parameter $\mathbf{u}_0'$. For SS-leapfrog+DR, simultaneously solving the fields in the ODE system removes the *T-in-n* error, however, with fixed plasma profiles the *T-in-n* error has no effect.

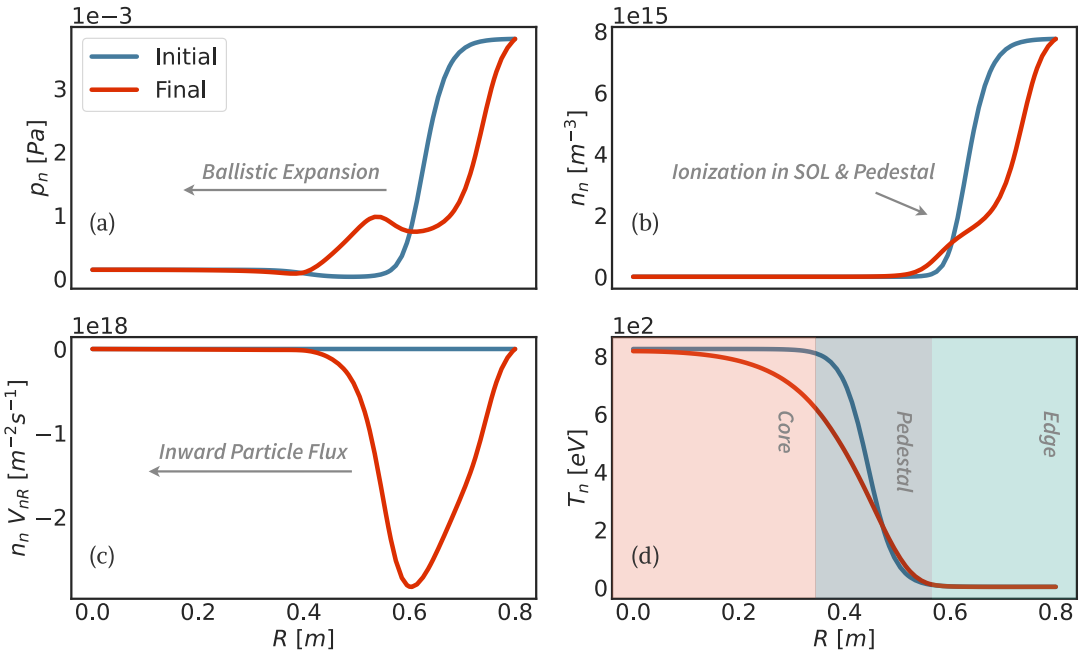

Figure 4.11: Initial and final ($t = 0.5$ [ms]) profiles for (a) pressure, (b) number density, (c) number density flux, and (d) temperature of the neutral species in 1-D tokamak pedestal case.

As discussed in Sec. 3.3.3 splitting the operators in the SS methods separates the PDE equations for the plasma and neutral species. This independent solution of fields makes the underlying linear system smaller and the associated GMRES solves computationally cheaper compared to the CN-JFNK method which couples the species within the linear solves. Unlike the 0-D cases, 1-D cases require periodic matrix refactorizations which makes using only the GMRES iteration count a poor proxy for cost. Relative to SS-field, SS-leapfrog+DR has slightly faster ODE solves. Comparing the wall clock time, the CN-JFNK method takes approximately three times more than the SS-field method with the same time step size, while SS-field takes about 10 percent longer relative to SS-leapfrog+DR. These simulations are relatively low resolution (they use a finite-element grid with 40×4 bi-quintic elements), and we expect that the SS methods will better outperform the CN on larger system sizes.

Figure 4.13 shows the convergence rate for all three methods at steady state. l_2-norm on the y-axis is the summation of errors for neutral fields ($n_n, \mathbf{V}_n$, and T_n) over the entire physical domain. SS-field method underestimates the neutral flux due to ODE/PDE splitting error, while the CN-JFNK and SS-leapfrog+DR have comparable accuracy.

Dynamic Solution

The dynamic solution often involves slow evolution resulting from the balance of large competing terms. These terms can be split between the ODE and PDE systems such as a balance between advection and ionization in the density equation and charge-exchange and the pressure gradient force. This case starts from a local atomic equilibrium and thus spans from a PDE dominated system initially to a balanced final state. There are more details in King et al. [17].

Figures 4.12(d-f) show the velocity profile of the tokamak pedestal test case for 10 intermediate states (starting with red) until we reach the asymptotic steady state (blue line) for all three methods. At the beginning the neutral flux to the core is very large which slows down as it reaches the high-temperature, dense plasma in the core. High charge exchange rate as well as ionization acts as a balancing force to pressure gradient which drives the flux.

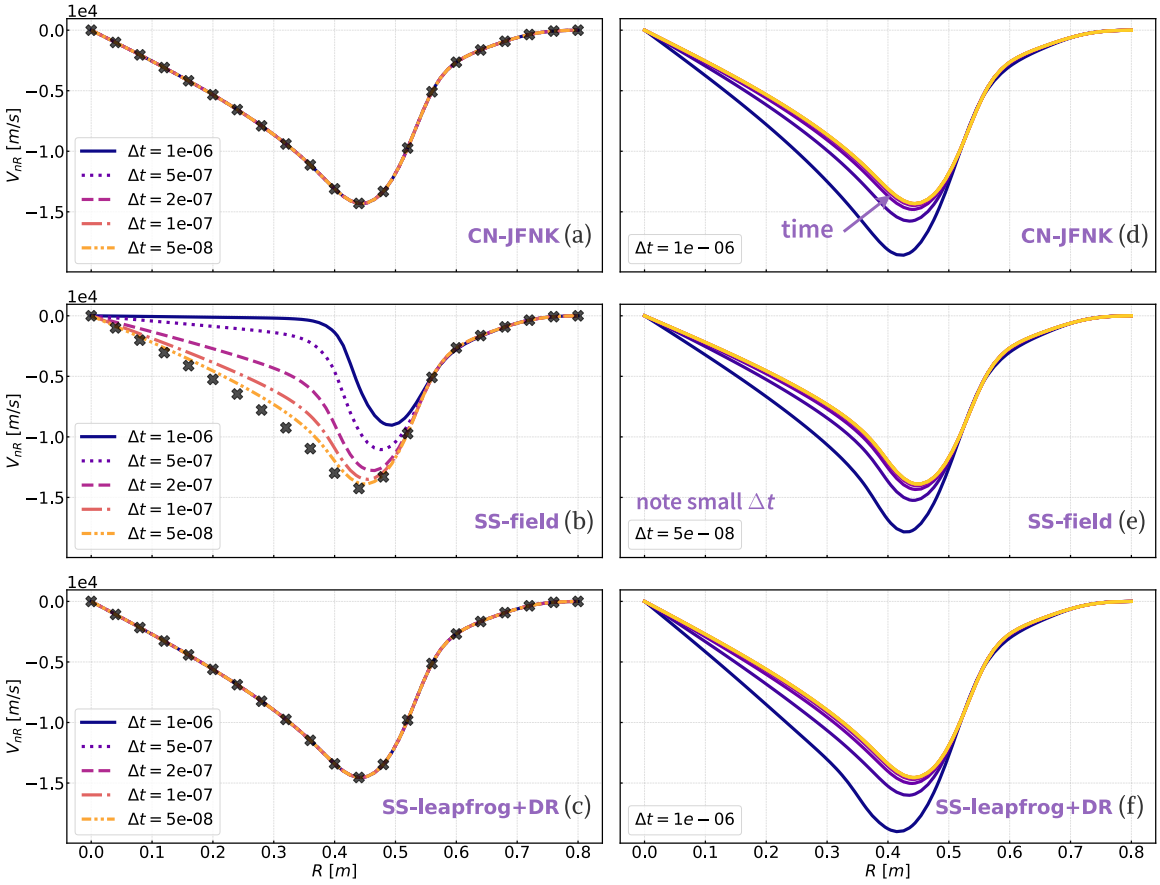

Figure 4.12: Steady state (a-c) and time dynamic (d-f) velocity profiles for neutral atoms in the tokamak pedestal case. Black **x** marks shows the steady state profile for fine-temporal-resolution computation with $\Delta t = 2 \times 10^{12}$ [s]. ODE/PDE splitting error is significantly affecting the SS-field profiles (b), where using SS-leapfrog+DR (c) reduces the error to levels comparable to CN-JFNK (a). Similarly, SS-leapfrog+DR (f) follows CN-JFNK (d) in capturing the dynamic evolution of neutral velocity profile.

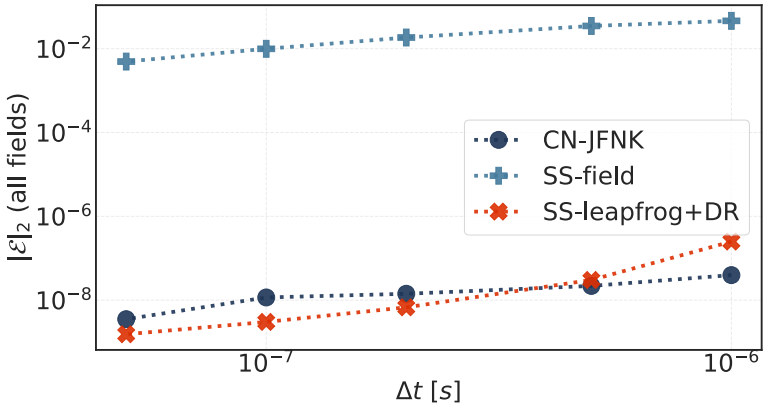

Figure 4.13: Accuracy and convergence of the different time-discretization methods for tokamak pedestal case. The y-axis represents the summation of l_2 errors for all neutral fields. The errors are calculated compared to a base solution with $\Delta t = 5 \times 10^{-9}$ [s].

As it reaches steady state, a flux of neutral particles move from wall to the core as is shown in Fig. 4.11(c). The time-dynamic evolution of all three algorithms, Figs. 4.12(d-f), is qualitatively similar (but not exactly and note the small time-step size for Fig. 4.12(e)). Both the SS algorithms under-predict the core penetration velocity, but this is particularly prevalent for the SS-field algorithm. As shown in Fig. 4.13, the SS-leapfrog+DR is of comparable accuracy to the CN-JFNK while the SS-field maintains substantial error.

4.5.2 Planar Electromagnetic Plasma Accelerator

Next, we present a time dynamic test case where full interaction between plasma and neutral species is studied. A generic 1-D snowplow includes dominantly hyperbolic and atomic reactions when a slug of cold neutrals is hit by an accelerating plasma. A linearly rising magnetic flux is injected from the left side into an infinitely long domain with uniform background plasma as shown in Fig. 4.14. This setup is a simplified representation of the acceleration region in a sheared-flow-stabilized Z pinch. Calculations are done using a finite-

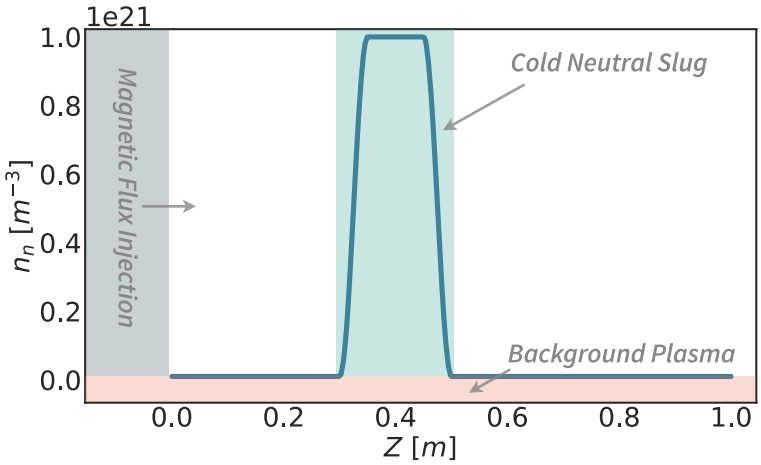

Figure 4.14: Initial neutral number density profile for snowplow case sitting in a uniform background plasma. A linearly rising magnetic flux is injected from left boundary pushing plasma towards the cold neutral slug.

element grid with 64×4 bi-quintic elements on a 2D domain. Considering a periodic boundary condition in one of the directions reduces the case to a 1-D plasma acceleration.

Rising magnetic flux accumulates magnetic pressure until it surpasses the thermal pressure of the plasma and creates a magnetic piston pushing the plasma to the right. According to snowplow theory, the magnetic piston is led by a shock wave where heated plasma starts to ionize the neutral slug upon reaching it which increases the plasma number density. In the process, plasma loses momentum due to ionization and charge exchange collisions which drags the neutrals along with plasma. Magnetic flux at the left boundary is implemented as a time-dynamic Dirichlet condition on the perpendicular component of the magnetic field. A zero Neumann boundary condition is used for number-density and velocity equations, where it acts as an open flow boundary on velocity equation.

Figure 4.15 shows the dynamic evolution of the plasma number density flux (starting with red line) up to 20 μs with $\Delta t = 10^{-8}$ [s]. All three methods deliver comparable accuracy

in solving dynamic problems as can be seen in Fig. 4.16. Unlike the tokamak pedestal test case, SS-field method gives fairly accurate results here which indicates that the ODE/PDE splitting error is not dominant.

Figure 4.16 presents the time-averaged l_2 error of all fields over the entire physical domain. The error is calculated compared to a base solution with $\Delta t = 10^{-10}$ [s]. CN-JFNK and SS-leapfrog+DR methods deliver comparable accuracy and convergence while the SS-field method converges more slowly and is less accurate at small time-step sizes. We conclude that for this case there is a common source of error for all three methods at large time-steps, likely from the PDE Crank-Nicolson and leapfrog discretization itself. At small time-step size, the PDE/ODE splitting error becomes dominant in SS-field method and adversely affects convergence.

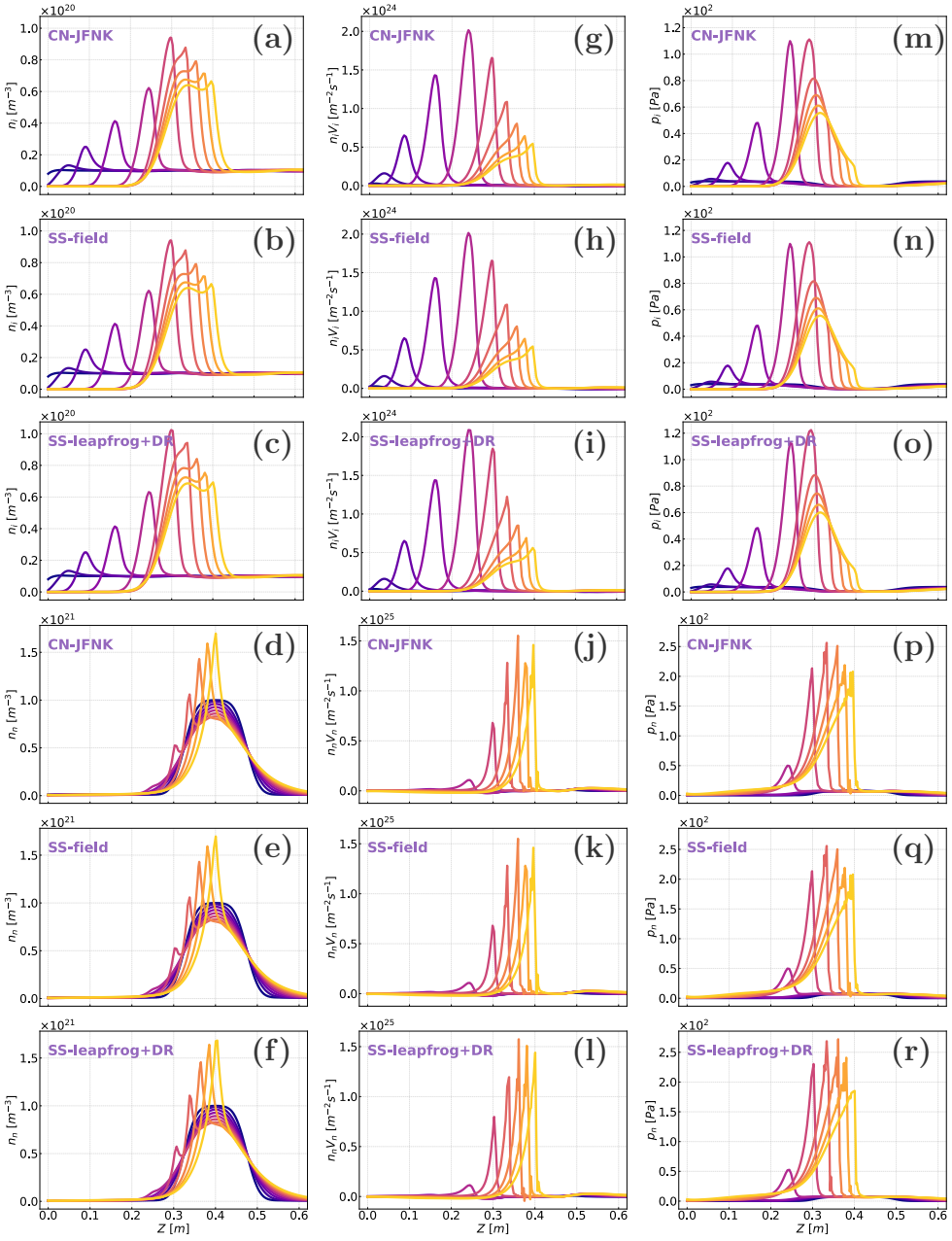

Figure 4.15: Dynamic evolution of the plasma and neutral species in a planar electromagnetic plasma accelerator. Top three rows show the plasma number density, plasma momentum, and plasma pressure. Bottom three rows show the same variables for neutral species. SS-field delivers comparable accuracy when ODE and PDE operators have the same sign.

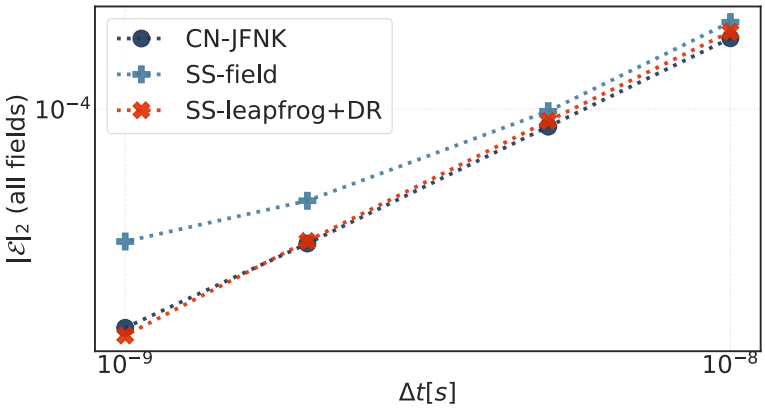

Figure 4.16: Accuracy and convergence of the different time-discretization methods for generic snowplow case. l_2-error on the y-axis is the summation of errors for all fields compared to a base solution with $\Delta t = 10^{-10}$ [s].

Chapter 5

PLASMA-NEUTRAL SIMULATION OF SHEARED FLOW Z-PINCH EXPERIMENT

The Z-pinch is a column of plasma in which a current passes through parallel to the axial direction (z-direction). The self-generated azimuthal magnetic field interacts with the axial current to give a radially inward Lorentz force, $\mathbf{j} \times \mathbf{B}$, which can be used to compress the plasma column or confine it through the pinch effect [8]. Z-pinches are attractive plasma confinement devices since the average β (ratio of kinetic pressure to magnetic pressure) reaches unity. Average β is an indication for how efficient magnetic field is used to confine the plasma. The nonlinear behavior of the Z-pinch gives it a complex nature, where adding atomic, ionization, and radiative physics elevated the complexity to a newer level [19]. Although theoretical discussions in this chapter cover the simplest Z-pinch, the main focus of this research is to look at plasma-neutral evolution in FuZE (Fusion Z-pinch Experiment) at University of Washington. Figure 5.1 shows a schematic of the device.

The device is composed of a 100 cm coaxial acceleration region followed by a 50 cm pinch assembly region. A shaped nose cone is attached at the exit of the acceleration region. The inner electrode has a 10 cm diameter, where the diameter of the outer electrode is 20 cm. The neutral gas is injected half-way in the acceleration region and ionized by breakdown. The plasma accelerates along the inner electrode into the assembly region where it pinches on the axis. Flowing current compresses the pinch and keeps feeding the neutral gas at the back end of the device to maintain the confinement. Velocity profile in the acceleration region and the feeding mechanism are of great interest in this research and we try to study the effects of plasma-neutral interactions on these phenomena.

The objective of this chapter is to give a brief overview of Z-pinch physics in both the-

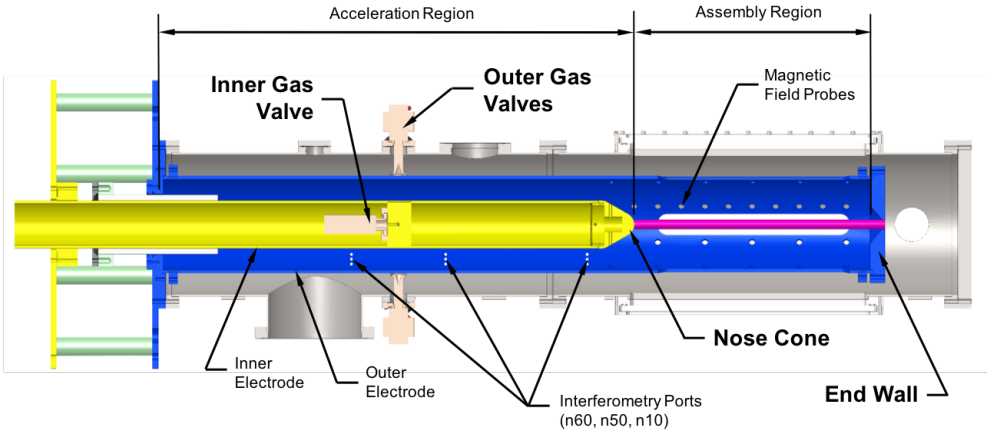

Figure 5.1: Schematic side-view of FuZE. Azimuthal magnetic field and mode amplitude is measured using a multiple axial arrays of surface-mounted magnetic probes. Plasma density is measured by a digital holographic interferometer and the plasma temperature is measured by Doppler broadening via impurity ion emission spectroscopy [44].

oretical and numerical manner. Equilibrium configuration in the pinch is given based on ideal-MHD model and the dynamic evolution of current sheet in the acceleration region as well as the pinch itself is studied analytically and numerically. Also, a quick overview of the applications is given at the end of the chapter.

5.1 Z-pinch Equilibrium

Equilibrium is the state where all the forces acting on a system reach a balance. According to second law of Newton, the system does not have any acceleration and keeps its state. In this section, we look at plasma equilibrium in assembly using ideal-MHD to describe the equilibrium states. The acceleration region is inherently dynamic and has no equilibrium state even if the current is constant.

5.1.1 Assembly region

In a Z-pinch, magnetic field is induced due to axial current in z-direction only, hence the only non-zero component is the poloidal component in θ-direction. $\nabla \cdot \mathbf{B} = 0$ is trivially satisfied since the poloidal magnetic field is only a function of radius. Starting with ideal-MHD and setting the time derivative and velocity equal to zero in momentum equation we get

$$\nabla p - \mathbf{j} \times \mathbf{B} = 0. \tag{5.1}$$

Ampere's law shows the current density as a function of magnetic field in steady state

$$\mathbf{j} = \frac{1}{\mu_0} \nabla \times \mathbf{B}. \tag{5.2}$$

Substituting this current density in momentum equation gives the radial component of pressure balance as

$$\frac{d}{dr}\left(p + \frac{B_\theta^2}{2\mu_0}\right) + \frac{B_\theta^2}{\mu_0 r} = 0, \tag{5.3}$$

where the two terms inside the derivative show the kinetic pressure and magnetic pressure and the last term represents the tension in the field lines due to their curvature. It is the tension force that provides the radial balance against pressure. We have only one equation for pressure and magnetic field; therefore, one of them is a free function. This creates a great variety of profiles in an equilibrium state. If we assume that the current density profile is known, then we can find the pressure and magnetic field profiles in the pinch. For example, assuming a uniform current density j_z, we find [19]

$$B_\theta(r) = \frac{\mu_0 I_p}{2\pi a^2} r, \qquad \text{for } r < a. \tag{5.4}$$

Integrating the pressure balance equation along radial direction gives pressure as

$$p(r) = \frac{\mu_0 I_p^2}{4\pi^2 a^2}\left(1 - \frac{r^2}{a^2}\right), \tag{5.5}$$

where I_p is the total axial current in the pinch and a is the plasma column radius. Plasma number density and temperature do not show separately in equation which adds another

level of freedom for equilibrium profiles. Assuming that the heat conductivity is sufficiently high, the temperature profile is uniform and number density follows the parabolic profile, same as pressure

$$n(r) = \frac{\mu_0}{4k_B T}\frac{I_p^2}{\pi^2 a^2}\left(1 - \frac{r^2}{a^2}\right), \tag{5.6}$$

where $T = T_i + ZT_e$ is the weighted plasma temperature and Z is the average ion charge. Integrating this equation in radial direction for a simple Z-pinch, we find the Bennett equation describing line number density in terms of current as [19]

$$NT = \frac{\mu_0}{8\pi k_B} I_p^2, \tag{5.7}$$

where N is the ion linear number density given by

$$N = 2\pi \int_0^a n(r) r dr. \tag{5.8}$$

According to Bennett's relation, for a constant current the lower line density is, the higher plasma temperature will be. However, there is a minimum on ion linear number density, stating that the electron drift velocity, $v_{De} = |j_z|/en_e$, should not exceed the ion thermal velocity, $v_{Ti} = (T_i/m_i)^{1/2}$; otherwise, current-driven micro-instabilities will develop [19].

It is convenient to express plasma confinement efficiency in terms of dimensionless pressure. β is defined as the ratio of average plasma kinetic pressure to average magnetic pressure

$$\beta_\theta = \frac{2\mu_0 \langle p \rangle}{B_\theta^2}. \tag{5.9}$$

Although high β_θ means better confinement efficiency, some classes of MHD instabilities arise in this regime which potentially can be avoided by lowering β_θ [6]. Another figure of merit in confinement schemes is the kink safety factor, q^*. This factor quantifies the stability against long-wavelength modes driven by the axial current known as kink modes [6]. The kink safety factor for a Z-pinch can be written as

$$q^* = \frac{aB_z}{LB_\theta}, \tag{5.10}$$

where B_z and B_θ are the axial and azimuthal magnetic field components, and a and L are pinch radius and pinch length, respectively. For a Z-pinch with no external axial magnetic field $q^* = 0$, which indicates why Z-pinch devices are unstable against current-driven kinks.

5.2 Dynamics of Z-pinch

Next we are going to look into dynamic behavior of plasma in a Z-pinch, since dynamics certainly affects the Z-pinch parameters. The FuZE experiment starts with neutral gas-puff in the middle of acceleration region and ionized by the capacitor bank. The break-down process complicates the dynamics further and is beyond the scope of this research. The Lorentz force accelerates plasma in the coaxial acceleration region and the pinch forms later in the assembly region. Here we assume the average electron drift velocity $\bar{v}_{De}$ is smaller than the ion thermal velocity v_{Ti}, hence current-driven kinetic instabilities do not appear. Although we consider a plasma seed in the acceleration region, the pre-filled neutral gas is not fully ionized and plasma-neutral interaction play an important role in dynamics study. In this chapter we are trying to use suitable theoretical models to describe the Z-pinch dynamics and compare them to numerical simulations of the system. In the remaining of this section, simple theoretical models are described for both acceleration and assembly region. However, our focus is on the acceleration region and numerical studies only consider this part of the device.

5.2.1 Acceleration region

Most of the analytic models proposed for Z-pinches in literature focus on the pinch in the assembly region. Here, we take similar approach to describe the plasma dynamics in the acceleration region where plasma moves in axial direction, although the coaxial geometry induces 2-dimensional profiles for the flow. For simplicity, we first look at planar plasma accelerators and then expand the model to cylindrical geometries.

Rail-gun model

The simplest model for plasma acceleration is zero dimensional rail gun theory. It is assumed that all plasma mass is concentrated at the current sheet and being accelerated by the Lorentz force due to induced magnetic field. For a planar rail gun, the out-of-plane magnetic field

generated by current $I(t)$ can be written as

$$B(t) = \frac{\mu_0 I(t)}{2\pi}, \tag{5.11}$$

with an unusual assumption of *unit depth* $= 2\pi$. Axial position of the current sheet is described by momentum equation as

$$\rho_l \frac{d^2 z}{dt^2} = \frac{\mu_0 I^2(t)}{4\pi}, \tag{5.12}$$

where ρ_l is the plasma density per unit depth and $I(t)$ is time dependent current. For a case of linearly rising current $I(t) = \dot{I}t$ the dimensionless momentum equation for $\xi = z/L_0$ and $\tau = t/t_0$ is

$$\frac{d^2 \xi}{d\tau^2} = \tau^2, \tag{5.13}$$

with $t_0 = (4\pi\rho_l L_0/\mu_0 \dot{I}^2)^{1/4}$. The assumption of lumped mass is not very realistic and results in smaller acceleration for the plasma.

Snowplow model

To make the model more realistic, the snowplow model assumes that the current sheet is infinitely thin and not permeable; hence, it sweeps the plasma in front of it as in the snowplow. Similar to rail-gun model, current induces an out-of-plane magnetic field creating a magnetic pressure behind the current sheet which accelerates it according to Newton's second law as

$$\frac{d}{dt}\left(M(t)\frac{dz}{dt}\right) = \frac{\mu_0 I^2(t)}{4\pi}, \tag{5.14}$$

where $I(t)$ is total current flowing in the current sheet and $M(t)$ is total mass of plasma per unit width in front of the current sheet given by

$$M(t) = \int_0^t 2\pi\rho_0 \frac{dz}{dt} dt, \tag{5.15}$$

in which ρ_0 is plasma density at rest. Assuming a linearly rising current $I(t) = \dot{I}t$ and defining nondimensional variables $\xi = z/L_0$ and $\tau = t/t_0$, the dimensionless Newton's law

can be written as

$$\frac{d}{d\tau}\left(\xi\frac{d\xi}{d\tau}\right) = \tau^2, \tag{5.16}$$

with $t_0 = (8\pi\rho_0 L_0^2/\mu_o \dot{I}^2)^{1/4}$. Accumulation of plasma in front of the current sheet changes the accelerating mass at each time resulting in faster acceleration compared to rail-gun model.

Slug model

Piriz et al. [26] present a model for hydrodynamic growth and decay of planar shock waves driven by a pressure piston. The model is based on approximate integration of the fluid conservation equations and describes dynamics of the shock and the piston by a coupled system of ODEs. We take the same approach to present a one dimensional model for current sheet propagation in planar plasma accelerator where we can assume the magnetic pressure behind current sheet is driving the magnetic piston following a shock wave. Consider a planar shock launched into a slab of plasma of density ρ_0 by magnetic pressure due to the current sheet with time dependent current $I(t)$. Assuming isentropic flow between the shock and the current sheet, the conservation equations can be written as

$$\begin{aligned} \frac{d\rho}{dt} &= -\rho\frac{\partial v}{\partial z}, \\ \frac{dv}{dt} &= -\frac{1}{\rho}\frac{\partial p}{\partial z}, \\ \frac{dp}{dt} &= \frac{\gamma p}{\rho}\frac{d\rho}{dt}. \end{aligned} \tag{5.17}$$

In addition, we assume the shock wave is always strong and Rankine-Hugoniot equations describe the jump at shock wave given by

$$\begin{aligned} u_s &= \frac{2}{\gamma-1}, \\ \rho_s &= \frac{\gamma+1}{\gamma-1}\rho_0, \\ p_s &= \frac{2}{\gamma-1}\rho_0 v_s^2, \end{aligned} \tag{5.18}$$

where u_s, ρ_s, and p_s are respectively plasma velocity, density, and pressure immediately after the shock and v_s is the shock velocity. Following Piriz et al. [26] we can describe the current

sheet and the shock dynamics as

$$\ddot{z}_p \approx \frac{B^2}{2\mu_0\rho_0 z_s} - \frac{2\dot{z}_s^2}{(\gamma+1)z_s}, \tag{5.19}$$

$$\ddot{z}_s \approx \frac{\gamma\dot{z}_s}{2(z_s - z_p)}\left(\dot{z}_p - \frac{2}{\gamma+1}\dot{z}_s\right). \tag{5.20}$$

Integrating the energy equation at a specific time, we can get an approximation for plasma pressure and density profiles between the current sheet and the shock given by

$$\begin{aligned} p(z,t) &\approx p_s\left[1 - \frac{(\gamma+1)^2}{2\gamma}\frac{\ddot{z}_p}{\dot{z}_s^2}(z - z_s)\right]^{\frac{\gamma}{\gamma-1}}, \\ \rho(z,t) &\approx \rho_s\left[1 - \frac{(\gamma+1)^2}{2\gamma}\frac{\ddot{z}_p}{\dot{z}_s^2}(z - z_s)\right]^{\frac{1}{\gamma-1}}. \end{aligned} \tag{5.21}$$

In order to compare with other models, we introduce non-dimensional variables $\xi_p = z_p/L_0$, $\xi_s = z_s/L_0$, and $\tau = t/t_0$, as before. Then, the governing equations for a case of linearly rising current can be written in dimensionless form

$$\begin{aligned} \ddot{\xi}_p &= \frac{\tau^2}{\xi_s} - \frac{2\dot{\xi}_s^2}{(\gamma+1)\xi_s}, \\ \ddot{\xi}_s &= \frac{\gamma\dot{\xi}_s}{2(\xi_s - \xi_p)}\left(\dot{\xi}_p - \frac{2}{\gamma+1}\dot{\xi}_s\right), \end{aligned} \tag{5.22}$$

with $t_0 = (8\pi^2\rho_0 L_0^2/\mu_0\dot{I}^2)^{1/4}$.

Self-similar solution

The similarity method is a standard method to obtain exact solutions of PDEs. In this method, solutions to PDE equations depend on certain groupings of the independent variables, called "similarity variables", rather than on each variable separately. These similarity variables are identified by using the invariance properties of PDEs subjected to finite or infinitesimal transformations [28]. Transforming PDEs using the similarity variables reduces the number of independent variables by one and allows to write the system as an ODE

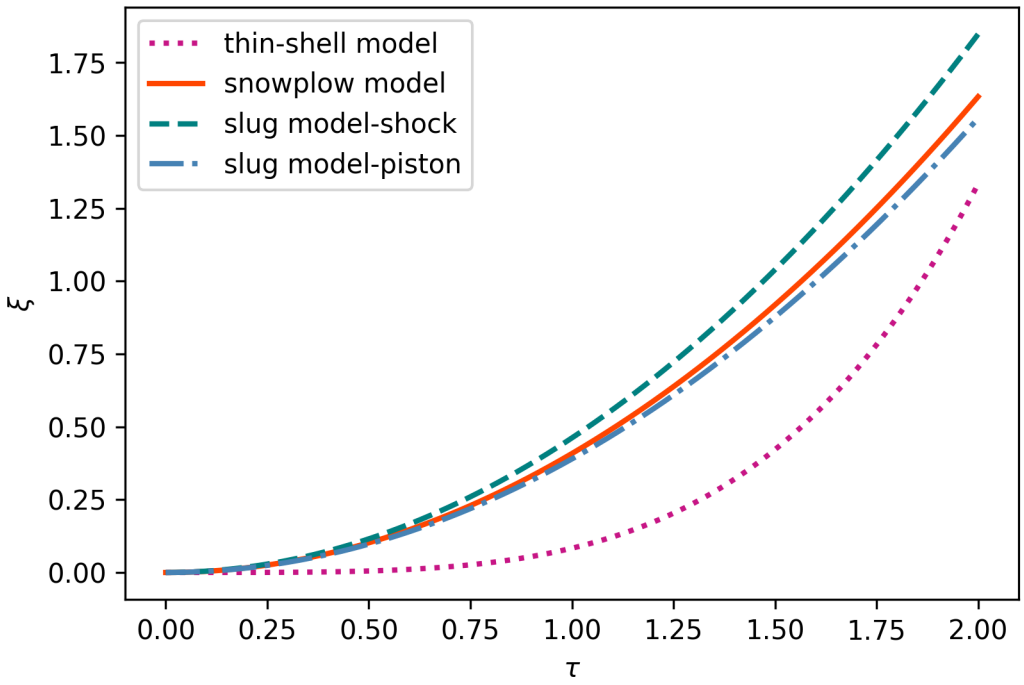

Figure 5.2: Analytic models are developed to predict the evolution of a current sheet in parallel-plate plasma acceleration test. Thin-shell model (dotted line) assumes all the plasma mass is at the current sheet and accelerates with it. The snowplow model (solid line) is one of the most used models and assumes that the current sheet is infinitely thin and sweeps all the plasma in front of it. The most realistic model is the slug model (dashed and dash-dot line) where a shock wave leads the current sheet and the plasma parameters are calculated by Rankine-Hugoniot equations.

problem. Consider the one-dimensional equations of gas dynamics given by

$$\begin{aligned}
&\frac{\partial \rho}{\partial t} + u\frac{\partial \rho}{\partial z} + \rho\frac{\partial u}{\partial z} = 0,\\
&\frac{\partial u}{\partial t} + u\frac{\partial u}{\partial z} + \frac{1}{\rho}\frac{\partial p}{\partial z} = 0,\\
&\frac{\partial p}{\partial t} + u\frac{\partial p}{\partial z} + \gamma p\frac{\partial u}{\partial z} = 0.
\end{aligned} \tag{5.23}$$

For the problem of gas acceleration by a piston with a time-varying pressure, if pressure is a polynomial function of time, $p(t) = p_0 t^n$, similarity variable can be written as

$$\xi(z,t) = \frac{z}{b_0 t^{1+n/2}}, \tag{5.24}$$

where $b_0 = (p_0/\rho_0)^{1/2}$ is a constant obtained from initial conditions with dimensions $[LT^{-1-n/2}]$ to make ξ a non-dimensional parameter. Introducing a single independent variable $\xi(z,t)$, density, pressure, and velocity can be written as functions of the new variable

$$\begin{aligned}
&\rho = \rho_0 R(\xi,)\\
&u = \frac{z}{t}U(\xi),\\
&p = \rho_0\frac{z^2}{t^2}\Pi(\xi).
\end{aligned} \tag{5.25}$$

Substituting these expressions in the governing equations, we obtain the reduced system of ODEs as follows

$$\begin{aligned}
\frac{dR}{d\xi} &= \frac{n/2R}{\xi(U-n/2-1)}\left[\frac{U^2-(n/2+1)U-2\Pi/R}{(U-n/2-1)^2-\gamma\Pi/R}\right]\\
\frac{dU}{d\xi} &= \frac{RU(U-1)(U-n/2-1)-\Pi(n+\gamma U)}{\xi[\gamma\Pi - R(U-n/2-1)^2]}\\
\frac{d\Pi}{d\xi} &= \frac{2\Pi}{\xi}\left[\frac{U^2-U(n/2+2+\gamma n/4)+(n/2+1)-\gamma\Pi/R}{\gamma\Pi/R-(U-n/2-1)^2}\right]
\end{aligned} \tag{5.26}$$

subject to Rankine-Hugoniot jump conditions at the shock position. Similarity variable holds a constant value at the position of piston and shock front, given by ξ_p and ξ_s, respectively. At the end, the axial position of piston and shock can be written as

$$\begin{aligned}
z_p(t) &= b_0\xi_p t^{1+n/2},\\
z_s(t) &= b_0\xi_s t^{1+n/2},
\end{aligned} \tag{5.27}$$

where we assume $\xi_s = 1$ and use conservation of mass to find the corresponding value for ξ_p. Stepanov showed that for $n = 2$ and $\gamma = 5/3$, the similarity variable at the position of piston is $\xi_p \approx 0.864$. Figure 5.4 shows the axial position of piston (current sheet) and shock front for a parabolic pressure (linearly rising current) profile using the similarity solution method.

Fluid model

Transport processes such as particle diffusion, heat conduction, electric resistivity, viscosity, and energy transfer can have important effects in Z-pinch dynamics. These plasma interactions are caused either by collisions or collective effects, and can be studied by evolution of the velocity distribution function in kinetic theory [19]. Most of the time, this kinetic description of the plasma is too detailed and whenever the species are close to equilibrium, fluid descriptions are sufficient to describe the plasma behavior. The one-fluid MHD model is the most commonly used one for Z-pinch simulations. The governing equations for this model is presented in section 2.2. Including the neutral interactions with plasma as it is done in section 2.3 expands the adequacy of the one-fluid MHD model in describing Z-pinch dynamics.

Rectangular geometry

A parallel plate accelerator as shown in Figure 5.3 is simulated using the plasma-neutral model. A current source is modeled as magnetic field boundary condition injecting linearly increasing magnetic flux at the left boundary. The top and bottom boundaries are periodic, therefore the magnetic field is uniform in the y-direction. The simulation results are compared with slug model and self-similar solution for 1D plasma acceleration. Figure 5.4 shows the evolution of the current sheet and the shock front for MHD simulation and analytic models.

Increasing current at left boundary increases the magnetic pressure until it overcomes the thermal pressure and the current sheet detaches from the boundary moving into the plasma. The current sheet is led by a shock front moving faster than the current sheet which establishes a profile between the current sheet and the shock front shown in Figure 5.5. As

Figure 5.3: Parallel-plate-electrode plasma acceleration test for current-sheet evolution. A current-sheet starts at the left boundary and accelerates the plasma in-front of it. The current-sheet is led by a shock-wave which increases the plasma density and temperature. The shock-wave travels faster than the current sheet resulting in a widening slug of plasma moving to the right.

it was described, the slug model assumes a uniform profile for this region, hence estimated position for the current sheet and the shock wave diverges from the MHD simulations. This is where similarity solution predicts the current sheet evolution with significant accuracy.

Cylindrical geometry

Similar to parallel plate electrodes, plasma acceleration in a coaxial-electrode configuration is modeled as shown in Figure 5.6. Here, the current source is modeled as magnetic field boundary condition at bottom. Radial current generates azimuthal magnetic field which depends inversely on radius accelerating the plasma with different rates. Figures 5.7 and 5.8 show the simulation results for a linearly increasing current.

Since the azimuthal magnetic field profile changes as $1/r$, the magnetic pressure behind the current sheet has $1/r^2$ dependency which results in a parabolic current sheet which can be seen in early time snaps of Figure 5.7. Canted current sheet results in radially outward Lorentz force which pushes plasma away from the inner electrode towards the outer electrode decreasing the plasma density and pressure at the inner electrode. Simultaneously, the magnetic pressure at the inner electrode increases, making this condition more severe which can result in a blow-by instability. Figure 5.8 shows that accumulating plasma at the outer electrode slows down the current sheet advection and instead current diffuses into the plasma. As plasma moves more towards the outer electrode, thermal pressure increases and plasma expands due to high pressure resulting in a flat density front.

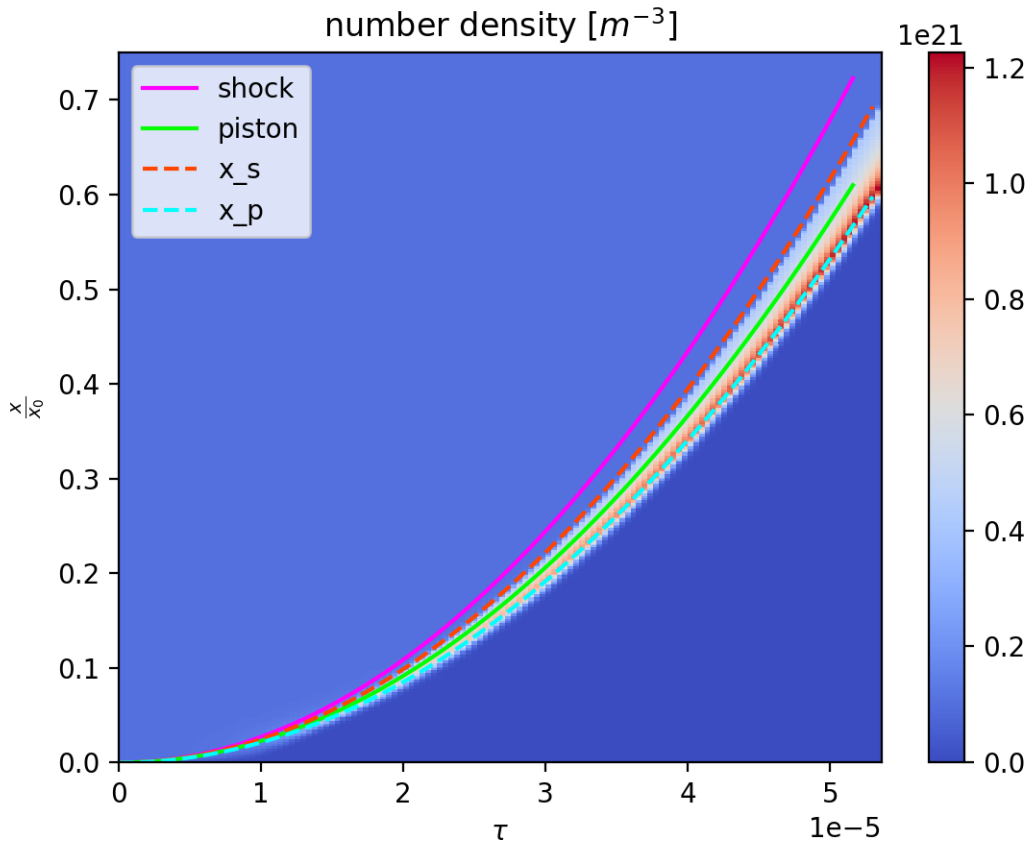

Figure 5.4: Space-time evolution of the plasma number density from MHD simulation of a parallel-plate-electrode configuration. The current rises linearly in time and the current sheet sweeps all the plasma in front of it seen as high density concentration close to the magnetic piston. As explained the current sheet is led by a shock-wave which increases the plasma density and temperature before it is swept by the current sheet. Solid lines show the predictions from a slug model and dashed lines are predictions from a self-similar solution.

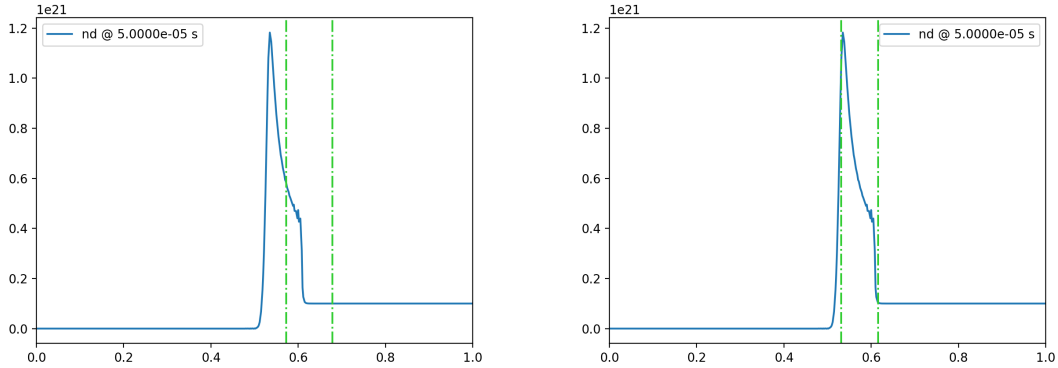

(a) MHD vs. slug model

(b) MHD vs. self-similarity solution

Figure 5.5: Plasma number density profile at the middle of acceleration shows the shock wave (jump at the right end of the slug) and the current sheet (jump at the left end of the slug) from MHD simulations in NIMROD. Plasma density ratio before and after the shock wave is approximately equal to 4, a value predicted by Rankine-Hugoniot jump conditions. Figure (a) shows that the slug model over-predicts the position of the shock wave and the current sheet since this model assumes linear profile for plasma density and pressure inside the slug. Figure (b) shows the good match between MHD simulation results and the self-similar model predictions.

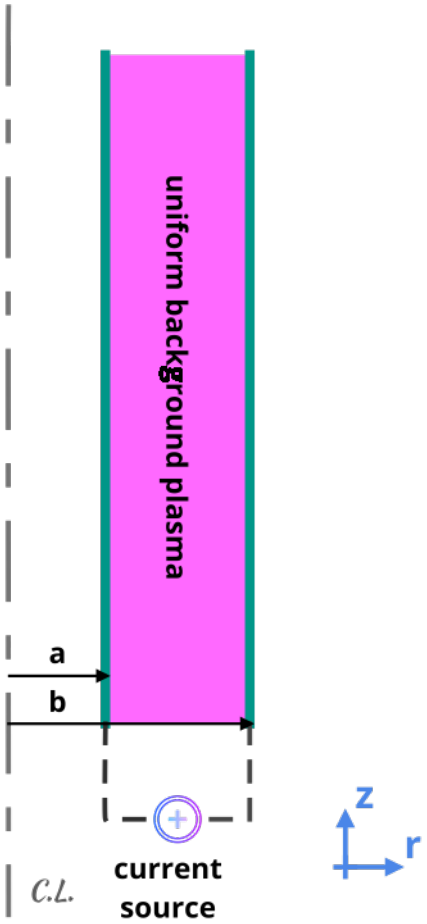

Figure 5.6: Coaxial-electrode plasma acceleration test for studying the geometry effects on current sheet evolution. In this configuration, the current sheet starts at the bottom boundary and propagates upward into the plasma. Radially uniform current generates an azimuthal magnetic field inversely proportional to radius. Higher magnetic pressure close to the inner electrode moves the plasma faster which results in a canted current sheet.

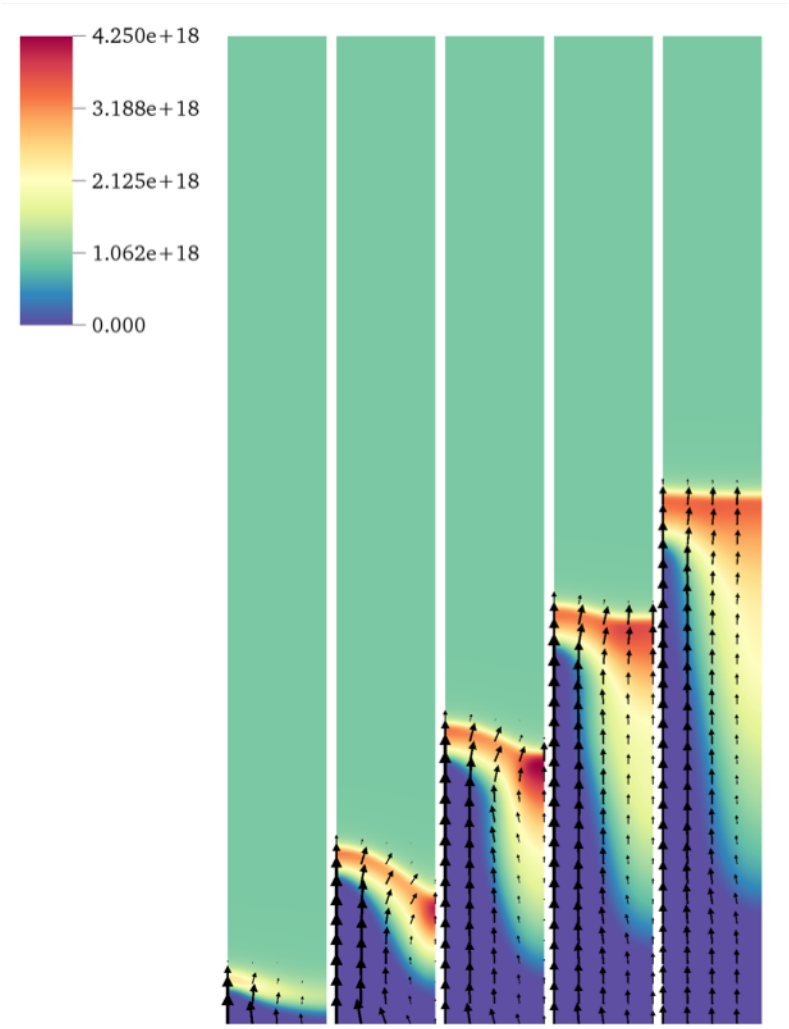

Figure 5.7: Time evolution of plasma density profile in a coaxial-electrode plasma acceleration test shows the formation of a shock-wave followed by a parabolic current sheet. The radial component of the current generates a radially outward Lorentz force which pushes the plasma against the outer electrode as shown by velocity quiver plots. This radial movement increases the plasma density at the outer electrode until the plasma pressure flattens the shock front.

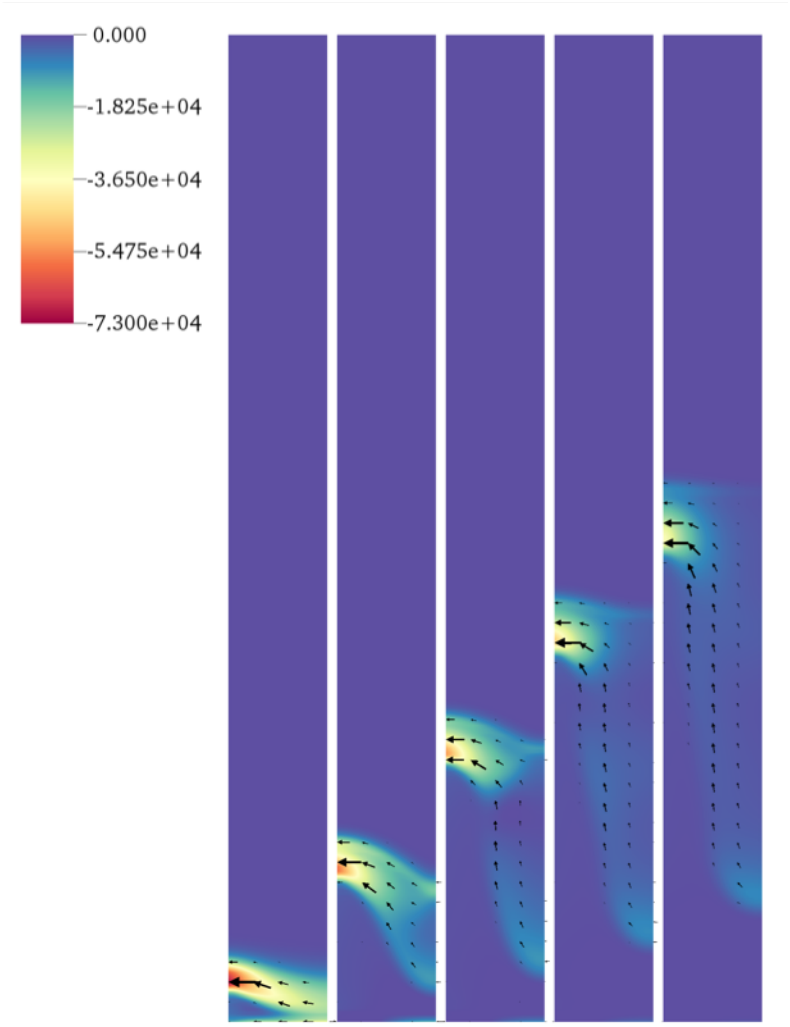

Figure 5.8: Time evolution of current density in a coaxial-electrode plasma acceleration test shows an almost radial current sheet close to the inner electrode. Since the radial plasma movement is negligible, the current sheet and the shock wave are similar to parallel-plate-electrode test case. Moving away from the inner electrode, the radial plasma movement increases the plasma density which in turn reduces the magnetic field advection. Close to the outer electrode, magnetic field penetrates the plasma diffusively which cannot accelerate the plasma as efficiently as before.

Chapter 6

CONCLUSION AND FUTURE WORK

6.1 Conclusion

The goal of this work is to evaluate the best time-discretization algorithm compatible with a semi-implicit leapfrog for inclusion of atomic interaction in a plasma-neutral MHD model. Two competing approaches are considered: Crank-Nicolson with JFNK (CN-JFNK) and Strang-split which is further subdivided into split-by-field (SS-field) and leapfrog-interleaved with Douglas-Rachford-inspired coupling (SS-leapfrog+DR). The Strang-split algorithms have many advantages. Testing on 0-D cases, Sec. 4.4, shows the ODE solver accurately eliminates both the need for nonlinear iteration when solving the highly nonlinear atomic-interaction equations and the CN time-centering error associated with the atomic terms (the fluid CN centering error is still present in the SS algorithm, but this error is not present in 0-D). Furthermore, the SS-leapfrog+DR method eliminates errors associated with the combination of the leapfrog and atomic interaction, identified as *T-in-n* and field-staggering error is Sec. 3.3.5. In fact, this algorithm reduces the error to that of the multi-step ODE solver tolerance for 0-D cases and thus it is not considered in our 0-D tests.

Consideration of tests with spatially dependent fields in Sec. 4.5 introduces ODE/PDE splitting error when using the Strang-split methods. We consider two examples: fusion-plasma edge fueling and a co-axial plasma-injector snowplow which are representative of slow and fast applications, respectively. Through the use of a Douglas-Rachford-inspired coupling, the ODE/PDE splitting error is minimized in SS-leapfrog+DR to be comparable to CN-JFNK. In fact, analysis of the accuracy shows that the error associated with SS-leapfrog+DR can be lower than CN-JFNK at the same time-step size as interleaving the ODE solves with the leapfrog eliminates the *T-in-n*, field-staggering and CN error associated

with the atomic interaction terms.

Finally, the Strang-split methods have a computational performance advantage relative to CN. Each species is considered independently during global-matrix solves. This significantly reduces the algebraic system size and fill-in and permits exploitation of parallelization over species (which is not presently explored). The test cases presented are relatively small but the performance advantage is evident. Given the scaling of global-matrix solves, we expect the performance advantage of the Strang-split methods to become larger with high-resolution cases. The advantages only grow when considering multiple species, such as tritium, carbon, and tungsten, where parallelization over species would lead to a huge performance gain. Future work will involve application of the SS-leapfrog+DR to this system of equations.

6.2 Future Work

Having a robust implementation of a plasma-neutral model in hand, we can expand our studies to various branches and directions in fusion-plasma devices. These possibilities can be divided into three groups: 1) improving the numerical implementation and efficiency, 2) improving the plasma-neutral model to include more physics, and 3) exploring other questions in the field of plasma-neutral interactions.

6.2.1 Improvements in numerical implementation

A major advantage of the numerical simulations compared to experimental studies is that setup time for numerical studies are extremely shorter that experimental setup times. Designing and building and experiment is a costly time-consuming process while changing and setting up a new numerical simulation is relatively cheap and fast. On the other hand, numerical runs are considerably longer than experimental shots and this is a big area to improve the numerical tools that we have in hand. Code optimization can help reduce the run time for numerical studies and make it a more reliable tool to help with design and understanding fusion-plasma devices. None of the codes in this research is optimized, thus finding the bottle-necks in numerical implementations can be the first step in improvements.

Another major advance in computational field is the rise of the parallel computation on graphics processing unit (GPU). Using thousands of nodes on GPU clusters helps to reduce the run time by orders of magnitude. Adapting scientific codes to run on GPUs relies on the code structure and how well the computations can be scaled for GPUs. One of the advantages we discussed for Strang-split method is that the ODE contributions are local calculations that are well suited for parallelism on GPUs. There is an initial effort in the NIMROD team to adapt the code for GPU calculations and incorporating the plasma-neutral model in this research can be an essential part of this move.

6.2.2 Improvements in plasma-neutral modeling

A huge improvement in the field of fusion-plasma simulation is the incorporation of other species such as carbon or even including diatomic molecules coming back from the walls. There are already some models such as KPRAD [11] that includes impurities in the extended MHD model used in NIMROD. A desirable extension to the plasma-neutral model here would be inclusion of impurities and other neutral species. Strang-splitting the ODE/PDE contributions again can be advantageous here. Since the PDE equations are independent for each species, adding more neutral species does not increase the linear matrix size and keeps the matrix solves tractable. Adding more and more components to the ODE section can be efficiently addressed by utilizing GPUs or even parallelization on CPU clusters. We can show that including impurities is properly scalable.

Another aspect that is extremely important in plasma-neutral modeling is the effects of boundary conditions on final simulation results. We have seen that changing the boundary conditions in the tokamak pedestal case changes the time asymptotic solutions considerably. It is preferable to impose physically motivated boundary conditions using available experimental data and theoretical models. Exploring the effects of different boundary conditions and how to best model physical boundary conditions in numerical methods is suggested as an important continuation for this research.

As discussed in Chap. 2, the plasma-neutral system is considered as optically thin where

the radiation energy is lost. There are applications that absorbing the radiation energy and following the status of photons in the system can be considerable. There are different models to track photons and radiation energy in fluid plasma formulation. Pursuing this aspect of modeling for interactive plasma-neutral models can be a possible research topic for future.

6.2.3 Exploring applications

All the studied test cases in this research whether 0-D, 1-D, or even 2-D cases are simplified problems to verify and study different aspects on the numerical implementation of the plasma-neutral model. Now that model implementation and its validation is done, we are encouraged to explore real-world applications of this tool in fusion-plasma field. King et al. [17] used this implementation to study neutral effects in ion orbit loss in tokamak-edge regimes for a two-dimensional domain using data reconstructions for DIII-D tokamak. Expanding further, these effects can be studied in 3-D considering the toroidally non-symmetric effects.

Another area that we have targeted in this work is the plasma acceleration region in sheared-flow-stabilized Z pinches. Here we inject magnetic flux from one end of the domain while in practice the breakdown happens in the middle of the domain and the magnetic flux advects in both directions. Stepanov et al. [36] discuss the physics of detonation and deflagration shack waves in such geometry. Implementing volumetric source terms can inject energy into the system representing the gas breakdown process. 2-D and 3-D simulation of plasma acceleration in coaxial electrodes of a sheared-flow-stabilized Z pinch can be considered as an interesting research topic for future. These studies will bring more insight into wave propagation physics in these devices.

BIBLIOGRAPHY

[1] C. F. Barnett, J. A. Ray, and J. C. Thompson. Atomic and Molecular Collision Cross Sections of Interest in Controlled Thermonuclear Research. Technical report, Oak Ridge National Laboratory (ORNL), Oak Ridge, TN (United States), aug 1964.

[2] G.T. Birk and A. Otto. A Three-Dimensional Plasma–Neutral Gas–Fluid Code. *Journal of Computational Physics*, 125(2):513–525, may 1996.

[3] Peter J. Catto. A short mean-free path, coupled neutral-ion transport description of a tokamak edge plasma. *Physics of Plasmas*, 1(6):1936–1943, jun 1994.

[4] Neil F Cramer. *The Physics of Alfvén Waves*. Wiley, sep 2001.

[5] J. Douglas and H. H. Rachford. On the numerical solution of heat conduction problems in two and three space variables. *Transactions of the American Mathematical Society*, 82:421–439, 1956.

[6] Jeffrey P. Freidberg. *Ideal MHD*. Cambridge University Press, Cambridge, 2014.

[7] Robert Goldston and Paul Rutherford. *Introduction to Plasma Physics*. Taylor & Francis, nov 1995.

[8] M. G. Haines. A review of the dense Z -pinch. *Plasma Physics and Controlled Fusion*, 53(9):093001, sep 2011.

[9] R. D. Hazeltine, M. D. Calvin, P. M. Valanju, and E. R. Solano. Analytical calculation of neutral transport and its effect on ions. *Nuclear Fusion*, 32(1):3–14, 1992.

[10] P. Helander, S. I. Krasheninnikov, and P. J. Catto. Fluid equations for a partially ionized plasma. *Physics of Plasmas*, 1(10):3174–3180, oct 1994.

[11] V. A. Izzo. A numerical investigation of the effects of impurity penetration depth on disruption mitigation by massive high-pressure gas jet. *Nuclear Fusion*, 46(5):541–547, 2006.

[12] Stephen C Jardin, J Breslau, and N Ferraro. A high-order implicit finite element method for integrating the two-fluid magnetohydrodynamic equations in two dimensions. *Journal of Computational Physics*, 226(2):2146–2174, 2007.

[13] George. Karniadakis and Spencer Sherwin. *Spectral/hp Element Methods for Computational Fluid Dynamics*. Oxford University Press, Oxford, 2nd ed. edition, 2007.

[14] S. Katsuki, K. Murayama, T. Nishi, I.V. Lisitsyn, and H. Akiyama. Influence of gas density distribution on the pinch process in gas-puff Z-pinch scheme. In *Digest of Technical Papers. 12th IEEE International Pulsed Power Conference. (Cat. No.99CH36358)*, volume 2, pages 1067–1070. IEEE, 1999.

[15] C. T. Kelley. *Solving Nonlinear Equations with Newton's Method*. Society for Industrial and Applied Mathematics, jan 2003.

[16] E. Khomenko, M. Collados, A. Díaz, and N. Vitas. Fluid description of multi-component solar partially ionized plasma. *Physics of Plasmas*, 21(9), 2014.

[17] J. King, S. Taheri, J. Callen, R. Groebner, B. Grierson, S. Haskey, and E. Howell. Integrating tokamak-edge mhd-fluctuation modeling with transport. Unpublished Manuscript, 2021.

[18] Randall J. LeVeque. *Finite Volume Methods for Hyperbolic Problems*. Cambridge University Press, aug 2002.

[19] Michael A. Liberman, John S. De Groot, Arthur Toor, and Rick B. Spielman. *Physics of High-Density Z-Pinch Plasmas*. Springer New York, New York, NY, 1999.

[20] H. Lütjens and J.F. Luciani. A class of basis functions for non-ideal magnetohydrodynamic computations. *Computer Physics Communications*, 95(1):47–57, may 1996.

[21] E. T. Meier and U. Shumlak. A general nonlinear fluid model for reacting plasma-neutral mixtures. *Physics of Plasmas*, 19(7):072508, jul 2012.

[22] Eric Todd Meier. *Modeling Plasmas with Strong Anisotropy, Neutral Fluid Effects, and Open Boundaries*. PhD thesis, Unveristy of Washington, 2011.

[23] Livermore Nationai. Description and use of lsode, the livermore solver for ordinary differential equations. 1993.

[24] Numerical Methods for Engineers, https://folk.ntnu.no/leifh/teaching/tkt4140/.

[25] Alexander Piel. *Plasma Physics*. Springer Berlin Heidelberg, Berlin, Heidelberg, 2010.

[26] A. R. Piriz, Y. B. Sun, and N. A. Tahir. Hydrodynamic growth and decay of planar shock waves. *Physics of Plasmas*, 23(3):032704, mar 2016.

[27] J. N. Reddy and D. K. Gartling. *The finite element method in heat transfer and fluid dynamics third edition*. CRC Press, jan 2010.

[28] PL Sachdev. *Self-similarity and beyond: exact solutions of nonlinear problems*. Chapman and Hall/CRC, 2019.

[29] D. D. Schnack, D. C. Baxter, and E. J. Caramana. A pseudospectral algorithm for three-dimensional magnetohydrodynamic simulation. *Journal of Computational Physics*, 55(3):485–514, 1984.

[30] D.D Schnack, D.C Barnes, Z. Mikic, Douglas S. Harned, and E.J Caramana. Semi-implicit magnetohydrodynamic calculations. *Journal of Computational Physics*, 70(2):330–354, jun 1987.

[31] Andrei N. Simakov. A drift-ordered short mean-free path description of a partially ionized magnetized plasma. *Plasma Physics and Controlled Fusion*, 51(5):055006, may 2009.

[32] C. R. Sovinec. A Tutorial on NIMROD Physics Kernel Code Development, 2001.

[33] C.R. Sovinec, A.H. Glasser, T.A. Gianakon, D.C. Barnes, R.A. Nebel, S.E. Kruger, D.D. Schnack, S.J. Plimpton, A. Tarditi, and M.S. Chu. Nonlinear magnetohydrodynamics simulation using high-order finite elements. *Journal of Computational Physics*, 195(1):355–386, mar 2004.

[34] C.R. Sovinec and J.R. King. Analysis of a mixed semi-implicit/implicit algorithm for low-frequency two-fluid plasma modeling. *Journal of Computational Physics*, 229(16):5803–5819, aug 2010.

[35] Weston M. Stacey. *Fusion Plasma Physics*. Wiley, Weinheim, Germany, aug 2005.

[36] AD Stepanov, U Shumlak, HS McLean, BA Nelson, EL Claveau, EG Forbes, TR Weber, and Y Zhang. Flow z-pinch plasma production on the fuze experiment. *Physics of Plasmas*, 27(11):112503, 2020.

[37] Daren (Princeton Plasma Physics Lab) Stotler, Charles (Princeton Plasma Physics Lab) Karney, Randall (Rensselaer Polytechnic Institute) Kanzleiter, and India) Jaishankar, S. (Institute for Plasma Research. User's Guide for DEGAS 2, 2019.

[38] B.R. Suydam. Effect of the gas blanket on the stability of the dense z-pinch. Technical report, University of California, 1979.

[39] Kips Thorne and Blandford Roger. *Modern Classical Physics: Optics, Fluids, Plasmas, Elasticity, Relativity, and Statistical Physics*. PRINCETON UNIVERSITY PRESS, 2017.

[40] E. L. Vold, F. Najmabadi, and R. W. Conn. Computational implementation of a coupled plasma-neutral fluid model. *Journal of Computational Physics*, 103(2):300–319, 1992.

[41] G.S. Voronov. A practical fit formula for ionization rate coefficients of atoms and ions by electron impact: Z=1–28. *Atomic Data and Nuclear Data Tables*, 65(1):1–35, jan 1997.

[42] Flow Z-Pinch Experiments, https://www.aa.washington.edu/research/ZaP.

[43] T. V. Zaqarashvili, M. L. Khodachenko, and H. O. Rucker. Magnetohydrodynamic waves in solar partially ionized plasmas: two-fluid approach. *Astronomy & Astrophysics*, 529:A82, may 2011.

[44] Y. Zhang, U. Shumlak, B. A. Nelson, R. P. Golingo, T. R. Weber, A. D. Stepanov, E. L. Claveau, E. G. Forbes, Z. T. Draper, J. M. Mitrani, H. S. McLean, K. K. Tummel, D. P. Higginson, and C. M. Cooper. Sustained Neutron Production from a Sheared-Flow Stabilized Z Pinch. *Physical Review Letters*, 122(13):135001, 2019.